THE UNIVERSITY OF MANITOBA

THE EFFECTS OF SMALL STRAINS & HEAT TREATMENT PROCESSING SEQUENCE ON THE FORMATION OF SPECIAL GRAIN BOUNDARIES IN COMMERCIALLY PURE NICKEL

By

SIU-LUN LEE

A Thesis
Submitted to the Faculty of Graduate Studies
In Partial Fulfillment of the Requirements for the Degree of

MASTER OF SCIENCE

METALLURGICAL SCIENCE LABORATORY

DEPARTMENT OF MECHANICAL AND INDUSTRIAL ENGINEERING

WINNIPEG, MANITOBA

November 2003

THE UNIVERSITY OF MANITOBA

FACULTY OF GRADUATE STUDIES

*****

COPYRIGHT PERMISSION

THE EFFECTS OF SMALL STRAINS & HEAT TREATMENT PROCESSING SEQUENCE ON THE FORMATION OF SPECIAL GRAIN BOUNDARIES IN COMMERCIALLY PURE NICKEL

BY

SIU-LUN LEE

A Thesis/Practicum submitted to the Faculty of Graduate Studies of The University of Manitoba in partial fulfillment of the requirement of the degree

Of

MASTER OF SCIENCE

ACKNOWLEDGMENTS

I acknowledge Dr. M.C. Chaturvedi and Dr. N.L. Richards who gave me an opportunity to work on this project and to use the equipment in the metallurgical science laboratory. I am extremely grateful to Dr. N.L. Richards for not only his sincere guidance throughout the course of this work, but also for his patient and encouragement throughout my master's degree. I am thankful to Don Mardis, John Van Dorp and Mike Boskwick for their technical assistance. Many useful discussions with Brendan Guyot are also gratefully acknowledged.

ABSTRACT

This thesis reports an investigation involving a thorough examination of the effects of thermomechanical processing commercially pure nickel on the grain boundary character distribution. Successive cold working of low strain levels and annealing steps were used to increase the fraction of special coincident site lattice (CSL) grain boundaries, $3 \leq \Sigma \leq 29$. Low CSL boundaries were found consist of mostly twin ($\Sigma 3$) and twin related ($\Sigma 3^n$) grain boundaries. Samples strained at less than or equal to 12% strain, one step or sequential steps, annealed between 500°C and 800°C for 10 minutes did not show improvement in special boundaries fraction compared to the as-received material with Σ_{sp} = 36.5%. Following the same sequence of strains, samples annealed at 1000 °C for 10 minutes showed increases of special boundaries up to an average of $\Sigma_{sp} \sim 55\%$, but an excessive grain growth was seen for all the samples annealed at 1000 °C.

A dramatic enhancement in special grain boundaries occurred when samples were sequentially strained and annealed at 900 °C for 10 minutes with over 70% of special boundaries recorded. Recovery mechanisms and moderate grain growth were energy minimization processes to the formation of special boundaries. Longer time annealing treatments up to 168 hours showed increased special boundary fraction at temperatures of 700°C and 800°C. Annealing at 700°C for 168 hours, after a 3% strain increased the special boundary fraction to 70.8%; with 6% strain annealed for 48 hours, a special boundary fraction of 76% was developed, where the grain size was measured as 46μm and all the other samples annealed for this period of time or longer had an average grain

size between 60-80μm. A higher annealing temperature of 800 °C were also processed, and the results showed the special boundaries only increased up to ~60% for both 3% and 6% strained samples.

Samples sequentially deformed with 3% strain annealed at 900 °C (4 steps) for 10minutes and 6% strain and annealed at 700 °C for 48 hours showed the highest percentage of special boundaries at 76%, and lowest degree of random boundaries connectivity observed out of all samples processed.

TABLE OF CONTENT

ACKNOWLEDGEMENTS i

ABSTRACT ii

TABLE OF CONTENTS iv

LIST OF TABLES

LIST OF FIGURES

Chapter 1: INTRODUCTION 1

Chapter 2: LITERATURE REVIEW 3

2.1 GRAIN BOUNDARY ENGINEERING 3

2.2 GRAIN BOUNDARY TYPES 4

2.2.1 Low Angle Grain Boundaries 5

2.2.1.1 Methodology to obtain Low Angle Boundaries 6

2.2.2 Coincident-Site Lattice (CSL) 6

2.2.3 High Angle Boundaries 9

2.2.3.1 LAB vs. HAB 10

2.3 TWIN BOUNDARIES 11

2.3.1 Mechanical and Annealing Twins 12

2.3.2 Twins Formation 13

2.3.2.1 Coherent Twins 13

2.3.2.2 Incoherent Twins 14

2.3.3 Factors Affecting Twin Formation 16

2.3.4 Multiple Twinning 17

2.4 EFFECTS OF COLD WORKING AND HEAT-TREATMENTS 18

2.5 THERMOMECHANICAL PROCESSING 21

2.6 GRAIN BOUNDARY POPULATION VARIATION 22

2.6.1 Multiple Step Recrystallization 23

2.6.2 One Step Recrystallization 25

2.6.3 Multiple Step Strain Annealing 27

2.6.4 One Step Strain Annealing 31

2.7 EFFECTS OF GRAIN SIZE 35

2.8 EXTENDED TIME OF ANNEAL PROCESSING 37

2.9 MATERIAL 38

2.10 GRAIN BOUNDARY NETWORK 39

2.11 ELECTRON BACK-SCATTERED DIFFRACTION (EBSD) 42

2.12 SCOPE OF PRESENT INVESTIGATION 43

Chapter 3: EXPERIMENTAL PROCEDURE 45

3.1 CHEMICAL COMPOSITION OF Ni-200 45

3.2 SAMPLE PREPARATION 45

3.3 STRESS AND STRAIN UNDER AXIAL LOADING 47

3.3.1 Engineering Stress-Strain Curve 47

3.4 TENSILE TEST 49

3.5 HARDNESS MEASUREMENTS 50

3.6 THERMOMECHANICAL PROCESSING 50

3.6.1 Short Annealing Time Experiments 50

3.6.2 Time Extended Experiments 52

3.7 SCANNING ELECTRON MICROSCOPY 53

3.8 ANALYSES TECHNIQUES 54

3.9 ORIENTATION IMAGING MICROSCOPY (OIM) 56

3.9.1 Orientation and Misorientation 59

3.9.2 EBSP Image Processing 59

3.9.3 Automated Indexing 61

3.9.4 Confidence Index (C.I.) 61

3.9.5 Image Quality (I.Q.) 62

3.9.6 Fit Parameter 62

3.10 OIM DATA COLLECTION 62

3.10.1 OIM Data Clean-Up 64

Capter 4: RESULTS AND DISCUSSION 66

4.1 MECHANICAL PROPOERTIES OF Ni-200 66

4.1.1 Stress-Strain Curve 67

4.2 MICROSTRUCTURE OF AS-RECEIVED MATERIAL 67

4.3 EFFECTS OF DEFORMATION ON GBCD 71

4.3.1 OIM Observations of Low Strained Samples 72

4.3.2 OIM analyses of low strained samples 73

4.4 HARDNESS RESULTS 74

4.4.1 Strain – annealed Processed Hardness Results 76

4.5 THERMOMECHANICAL PROCESSING 78

4.5.1 One Step Strain Anneal Processing Results 78

4.5.2 Multiple Steps Strain Anneal Treatments 83

4.5.2.1 Annealed at 500°C and 700°C for 10 min. 83

4.5.2.2 Annealed at 800°C for 10 min. 87

4.5.2.3 Annealed at 900°C for 10 min. 90

4.5.2.3.1 CSL Distribution 100

4.5.2.4 One Step Strain Anneal at 900°C 104

4.5.2.5 Annealed at 1000°C for 10 min. 110

4.5.3 Strain Anneal Long Time Anneal Experiments 116

4.5.3.1 One-Step of 3% Strain at 700°C 116

4.5.3.2 One-Step of 6% Strain at 700°C 122

4.5.3.3 One Step Anneal at 800°C 126

4.5.3.4 Fine Tuning at $\sum 3^n$ Boundary 130

4.5.4 Statistical Analysis of Selected Experiments 133

4.5.5 Summary of Thermomechanical Treatment Results 136

4.5.5.1 Single Step Strain-Anneal Treatments 136

4.5.5.2 Multiple Step Strain-Anneal Treatments 137

4.5.4.3 Long Period of Anneal Treatments 137

Chapter 5: CONCLUSION 139

Chapter 6: RECOMMANDATIONS 142

REFERENCES 144

APPENDIX A 151

LIST OF TABLES

1. Distribution of special boundaries for the three alloys 23

2. Strain – anneal treatments for Oxygen-free electronic copper 24

3. Fraction special boundaries of OFE 1-4 24

4. Results of the occurrence of CSLs in grade 270 pure nickel 26

5. Nominal Composition of Ni-16Cr-9Fe Alloys 28

6. GBCD of the SA and CSLE Tensile samples 29

7. Thermo-mechanical Processing steps of Alloy 600 30

8. Strain annealing processing details of commercially pure nickel 32

9. Results of twinning frequency and LAB 32

10. Table of Heat-treatments for 99.999% pure nickel 38

11. Limiting Chemical Composition of Ni-200 45

12. Example of 2^3 factorial matrixes 51

13. Time extended experimentations 52

14. Mechanical Properties of Ni-200 66

15. List of tolerance values and fractions of Sigma boundaries of as-received sample with $3 \leq \sum \leq 29$ 70

16. Fraction of $\sum_{sp}$ for Samples Deformed at Room Temperature 73

17. Strain – annealed hardness results in Vickers Hardness 76

18. Single step special boundaries percentage obtained by 3% and 12% strains and annealed at 500°C and 800°C 79

19. Grain size measurements of one-step strain anneal treatments 82

20. Values for 2^3 Factorial Multiple Steps Strain – Anneal Treatment 83

21. Result Values of Multiple Steps Processing Annealed at 500°C and 800°C 85

22. Grain size measurements of multiple steps processing at 800°C 88

23. Special boundary values due to single-step strain-anneal processing 136

24. Special boundaries values due to multiple steps strain-anneal processing 137

25. Special boundaries values due to extended time of anneal processing at 700°C 137

26. Special boundaries values due to extended time of anneal processing at 800°C 137

A1 (a)-(d). CSL distribution of samples processed at 900°C 151

A3 (a)-(d). CSL distribution of samples processed at 1000°C 157

LIST OF FIGURES

1. CSL model showing the number of coincidence sites 7

2. Random High-angle grain boundary transition zone 9

3. Energy Comparison of Low-angle and High-angle Grain Boundaries 10

4. Schematic of simple twinning with black circles represents the atoms with changed positions 11

5. Schematic representation of Coherent Twin Boundary 14

6. Schematic representation of Incoherent Twin boundary 15

7. Energy (γ) of a function of misorientation (φ) for Coherent and Incoherent Twins 15

8. Microstructure of a cold rolled alloy showing elongated grains 19

9. Microstructure of a strain – anneal alloy 20

10. Picture of an fcc structure with {1 1 1 } plane indicated 39

11. Schematic representation of grain boundary structure fracture 40

12. Misorientation map of break-up of random boundary network for the case of sequentially processed Inconel 600 41

13. Schematic representation of machined standard tensile sample 46

14. Engineering stress-strain curves 48

15. Schematic representation of the Scanning Electron Microscope 53

16. Inelastic Scattered electrons from specimen generating Kikuchi-lines on fluorescent screen 55

17. Schematic of the EBSD geometry including calibration parameters 57

18. Coordinate systems of specimen and cubic symmetric crystal 59

19. Schematic of Hough transform parameters in x-y space 60

20. Picture inside of SEM chamber 63

21. Engineering stress-strain curve 67

22. As – received Ni-200 observed in
(a) Optical microscope magnified at 200X 68
(b) Grey scale shaded OIM image with colour coded CSL boundaries 68
(c) Non-grey scale shaded OIM maps with colour coded CSL boundaries 69

23. Processed OIM maps of samples strained at room temperature without Heat-treatment: a) 3% strain and b) 12% strain 72

24. Cold Worked Hardness Curves 75

25. Vickers Hardness verses Percentage strain curves at various temperatures 76

26. Non – grey scale shaded processed OIM maps of
(a) 3% strain annealed at 500°C 79
(b) 12% strain annealed at 500°C, (c) 3% strain annealed at 700°C 80
(d) 12% strain annealed at 700°C, (e) 3% strain annealed at 800°C,
(f) 12% strain annealed at 800°C 81

27. Graphical Representation of Multiple steps processing results annealed at 500°C and 800°C 84

28. OIM maps of (a) grain boundary network, (b) random boundary network of 2 steps – 3% strain for a total of 6% strain annealed at 800°C 86

29. Three-center point samples processed at 2 steps – 4.5% strain for 650°C 87

30. Multiple steps special boundaries percentage annealed at 500°C, 700°C and 800°C 89

31. OIM maps of processed samples (a) 1 step – 6% strain, (b) 2 steps – 3% strain annealed at 700°C 91

32. Microstructures of nickel annealed at
(a) 500°C 92
(b) 800°C, (c) 900°C 93

33. Grain size distribution of as-received and processed samples annealed at 900°C 94

34. OIM maps of sample processed at 1 step – 6% strain at 900°C 95

35. OIM maps of sample processed at 2 steps – 3% strain at 900°C 96

36. OIM maps of sample processed at 2 steps – 6% strain at 900°C 97

37. OIM maps of sample processed at 4 steps – 3% strain at 900°C 98

38. CSL distributions of multiple steps processing samples annealed at 900°C 101

39. Contribution of annealing twins ($\sum 3$) to GBCD 102

40. The effects of grain size on the distribution of $\sum 3$ boundaries at annealing temperatures 500°C, 700°C, 800°C and 900°C 103

41. One Step Strain - Anneal Processed Samples, annealed at 900°C 105

42. OIM maps of sample processed at 1 step – 3% strain at 900°C 106

43. OIM maps of sample processed at 1 step – 6% strain at 900°C 107

44. OIM maps of sample processed at 1 step – 9% strain at 900°C 108

45. OIM maps of sample processed at 1 step – 12% strain at 900°C 109

46. Multiple Steps Processing Results of Special Boundaries Percentage Annealed at 500°C, 700°C, 800°C, 900°C and 1000°C 111

47. Grain size distributions of the as-received sample, and samples strained and annealed at 900°C and 1000°C 112

48. CSL distributions of multiple steps processing samples annealed at 1000°C 113

49. Effects of grain size on the distribution of $\sum 3$ boundaries at annealing temperatures 500°C, 700°C, 800°C, 900°C and 1000°C 115

50. Graph of samples processed at 1 step 3% strain annealed at 700°C for 168 hours 117

51. The network of random boundaries in the microstructure of 1 step – 3% strain annealed at 700°C for (a) 0.167hr, (b) 48hr, (c)72hr, (d) 96hr, (e) 168hr 120

52. Distribution of CSL, $3 \leq \sum \leq 29$ boundaries for 1 step – 3% strain annealed at 700°C 121

53. Graphical representation of special boundaries processed with 1 step 6% strain annealed at 700°C for 168 hours 122

54. Grain size measurements of 1 step 3% strain and 1 step of 6% strain annealed at 700°C for an extended period of time 123

55. CSL boundaries distribution of 1 step 6% strain annealed at 700°C for 168 hours, $3 \leq \sum \leq 29$ boundaries 125

56. Results of special boundaries of increased annealing time up to 168 hours for 1 step 3% strain and 1 step 6% strain annealed at 800°C 126

57. Grain size measurements of 1 step 3% strain and 1 step of 6% strain annealed at 800°C with increased annealing time 128

58. Distribution of CSL boundaries, $3 \leq \sum \leq 29$, for (a) 1 step – 3% strain and (b) 1 step – 6% strain annealed at 800°C 129

59. Figure 59: Graphical representation of the distribution of special boundaries at various misorientation angles processed at
(a) 1 step of 3% strain annealed at 700°C 130
(b) 1 step of 6% strain annealed at 700°C 131
(c) 1 step of 3% strain annealed at 800°C 131
(d) 1 step of 6% strain annealed at 800°C 132

60. Main effect plots for (a) strain, (b) temperature, (c) number of cycles 134

61. Variable effect combinations (a) strain per cycle and number of cycles, (b) strain per cycle and temperature, (c) number of cycles and temperature 134

A2 (a)-(d) OIM maps of multiple step processed samples annealed at 1000°C 153

A2 (e)-(h) Random boundary network of samples annealed at 1000°C 155

A4 (a)-(e) OIM maps of 1 step 3% strain annealed at 700°C for an extended period of time 159

A5 (a)-(e) OIM maps of 1 step 6% strain annealed at 700°C for an extended period of time 161

A5 (f)-(j) Random boundary network of Figures A5 (a)-(e) 163

A6 (a)-(e) OIM maps of 1 step 3% strain annealed at 800°C for an extended period of time 165

A6 (f)-(j) Random boundary network of Figures A6 (a)-(e) 167

A7 (a)-(e) OIM maps of 1 step 6% strain annealed at 800°C for an extended period of time 169

A7 (f)-(j) Random boundary network of Figures A7 (a)-(e) 171

Chapter 1

INTRODUCTION

Grain boundaries are one of the most important features of the microstructure of engineering materials. The properties of a grain boundary are fundamentally related to its structure, and it is known to have various effects on the mechanical, chemical and physical properties of polycrystalline materials.

In the past two decades, researchers have demonstrated that it is possible to manipulate the distribution of the character of grain boundaries and grain boundary network arrangements to introduce higher proportions of boundaries with superior properties, or so called 'special' boundaries. The basis for grain boundary engineering of a material was developed to approach an optimized population of special boundaries to improve its resistance to detrimental effects during service, such as intergranular degradation. The methodology grain boundary engineering utilizes thermo-mechanical (strain – anneal) processing of material to enhance the proportion of special boundaries. This is particularly valuable in the aerospace industry where high material and process costs necessitate superior material performance.

The change in grain boundary population is monitored in terms of the frequency of boundaries having low-Σ coincidence site lattice (CSL) geometries. These low-Σ CSL boundaries have been shown to provide special properties against microstructure failures such as intergranular fracture, corrosion and segregation.

The grain boundary proportion of special boundaries is governed by the original grain texture, as well as introducing modifications to the existing grain boundary. Thermo-mechanical processing is one approach for manipulating the grain boundary population. The degree of strain, annealing temperature and time are the three most important processing parameters to control.

In this thesis, commercially pure nickel (99.5% pure), or Ni-200 was used to study the relationships between thermo-mechanical processing and the grain boundary characteristic distribution (GBCD). The reason for using commercially pure nickel was to avoid difficulties with precipitations segregating along grain boundaries. Electron Backscatter Diffraction (EBSD) technique in Scanning Electron Microscopy (SEM) was used to characterize the grain boundary network. Orientation Image Microscopy (OIM) uses automated diffraction pattern analysis of EBSD patterns to obtain crystallographic data on a point-by-point basis over a selected area of a sample. However, it is hoped that results can be applied or modified to commercial nickel based alloys, where improved mechanical properties (strength, fatigue, creep and weldability) of these alloys would prolong their life during service.

Chapter 2

LITERATURE REVIEW

Physical and mechanical properties of polycrystals depend to a large extent on the atomic structure of grain boundaries of the material. Grain boundaries in metals are influenced by grain boundary characteristics, which are associated to some particular boundary geometry, or the relative misorientation between adjacent grains. Failures during service have been often associated with elements of boundary crystallography such as intergranular corrosion and creep; therefore it is important to control grain boundary structures.

2.1 Grain Boundary Engineering

'Grain boundary design' or 'grain boundary engineering' was first proposed in 1984 by Professor Watanabe of Tohoku University to improve properties of a material. By considering grain boundaries as material constituents, one can vary their role and effectiveness in polycrystals, irrespective of the crystal lattice [1]. This design aims to promote high proportion of "special" grain boundaries to have better properties than an average boundary by applying the strain and anneal technique. These special grain boundaries are beneficial in improving the overall properties of the material, such as strength, fatigue, creep and weldability. Special grain boundaries are produced throughout the entire volume, not just a surface phenomenon [2]. A general way to classify grain boundaries that have the potential to be special is called the 'coincidence

site lattice', or the CSL model. This is a geometrical model that expresses quantitatively the 'goodness of fit' between two adjacent lattices, and across a grain boundary.

Kronberg and Wilson [3] were the first in 1949 to propose a general way of describing the specific structure of grain boundaries based on the misorientation of adjoining crystals. Later Aust and Rutter in 1959 experimentally observed special properties in low-Σ CSL grain boundaries [4] when small solute additions to pure metals showed that the solutes segregated to non-special boundaries, with the consequence that special grain boundary had higher migration rates than the non-special boundaries. Thereafter, many researchers have attempted to optimize microstructures of polycrystals via alteration of the grain boundary character distribution (GBCD), which describes the distribution of grain boundary types in a metal and it has been shown that these low-Σ CSL grain boundaries can possess special mechanical, chemical, kinetic and electronic properties.

2.2 Grain Boundary Types

Grain boundaries are important elements of the microstructure of polycrystalline engineering materials, which are known to have various effects on the mechanical and chemical properties of polycrystalline materials [5]. Polycrystals consists of a large number grains and grain boundaries. The presence of grain boundaries can be either beneficial or harmful to the properties of the material, depending on the type and structure of grain boundaries [6]. Normally, grain boundaries are characterized

geometrically by the relative orientation relationship between adjoining grains, or the misorientation and the orientation of the grain boundary plane (grain boundary inclination) [6]. Grain boundaries can be classified into one of three categories [7]:

- Low-angle boundaries (LABs) consist of low misorientation angles up to 15°.
- Coincident site lattice boundaries (CSLBs) are those high angle boundaries with misorientations of two lattices of the adjacent crystals (grains) have some coincident points.
- High-angle boundaries (HABs) are boundaries with misorientation angles greater than 15°, which are also considered as general random boundaries.

The properties of grain boundaries depend largely on the local atomic arrangement. The effect of texture also should be considered. High incidence of low-angle boundaries and coincidence boundaries often appears in strongly textured materials [8]. It should also be noted that not all CSL structures possess special properties; CSL is not a sufficient predictor of special properties, the orientation of the grain boundary plane may also affect the degree of specialness.

2.2.1 Low Angle Grain Boundaries

When the misorientation between two grains is small, such as $< 15°$, the result is a low angle boundary, which it has been shown to improve the intergranular properties [9]. Low-angle boundaries (LABs) and coincidence-site lattice boundaries (CSLBs) with low Σ orientation ($\Sigma \leq 29$) display improved physical and chemical properties relative to general or high angle boundaries (HABs) ($\Sigma \geq 29$) [10].

2.2.1.1 Methodology to obtain Low Angle Boundaries

Low-angle boundaries can be produced in a number of ways. The general method of producing it is by inducing a small amount of deformation (1 to 10%) and followed with an annealing treatment [11]. The amount of deformation and temperature must be low enough to prevent the formation of new grains by recrystallization [11]. When the material is heated, the dislocations would be grouped into the lower energy configuration of a low-angle boundary by dislocation climb. The resulting structure is a polygon-like network of low-angle grain boundaries.

2.2.2 Coincident-Site Lattice (CSL)

The CSL model can be used to relate grain boundary misorientation. The degree of coincidence is parameterized by the reciprocal ratio of the coincidence fraction, denoted as the Σ number (i.e., the grains adjacent at a $\Sigma 7$ boundary have one-seventh of their representative crystal lattice points in coincidence) [10].

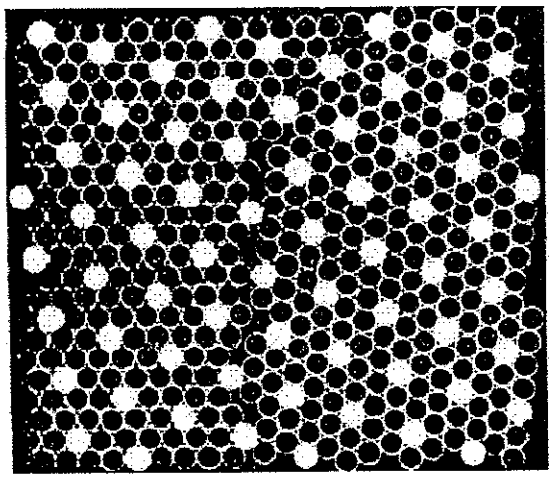

Figure 1: Coincidence Site Lattice model [11]

Atoms in white from Figure 1 represent coincidence sites, and this is a $\Sigma = 7$ coincidence site lattice, one in seven of the lattice sites of a particular grain are white. CSL boundaries characterized by low-Σ values should be considered special, represented by symbol Σ_{sp} [12]. As compared with higher Σ boundaries, low-Σ grain boundaries possess a better fit arrangement of atoms, which are less susceptible to solute segregation and greater resistance to sliding, cavitations, fracture [13] and localized corrosion [14].

For a cubic cell, whenever an even number is obtained for Σ, there is a coincidence lattice site in the center of the cell which then means that the true area ratio, Σ, is half of the apparent quantity. Therefore, Σ is always odd in the cubic system [15].

A correlation between deviations of a boundary from an exact CSL misorientation, can be expressed as the v/v_m parameter. Where v is the angular rotation required to bring the boundary to the exact CSL misorientation, or the actual deviation of

a boundary from the perfect $\Sigma 3$ CSL misorientation; and v_m is the maximum permitted deviation, as defined by Brandon's Criterion [12]:

$$v_m = 15^{\circ} \Sigma^{-1/2} \quad (1)$$

An estimate of the effect on the materials properties due to the increase of the $\Sigma 3$s can be proposed using the v/v_m parameter. A lower deviation parameter is most desired to improve grain boundary fit. This is associated with a lower energy grain boundary configuration and a low mobility. In particular, coherent $\Sigma 3$ on {111} plane annealing twins has a very low v/v_m. The $\Sigma 3^n$s with intermediate v/v_m values are boundaries that have higher mobility, and the resulting material promotes ductility in nickel [16]. At other $\Sigma 3$ grain boundaries, with irrational planes normally have high v/v_m values and act as non-CSL general grain boundaries.

There has been no theoretical upper limit of Σ_{sp}, which a coincidence boundary may not exhibit special mechanical behaviour. Judging from the experimental work reported in the [17], it is likely that the upper limit of Σ_{sp} is approximately 29. The actual value may vary depending on the material composition, microstructure and test conditions.

2.2.3 High Angle Grain Boundaries

The standard high angle grain boundary represents a region of random misfit between the adjoining crystal lattice, Figure 2.

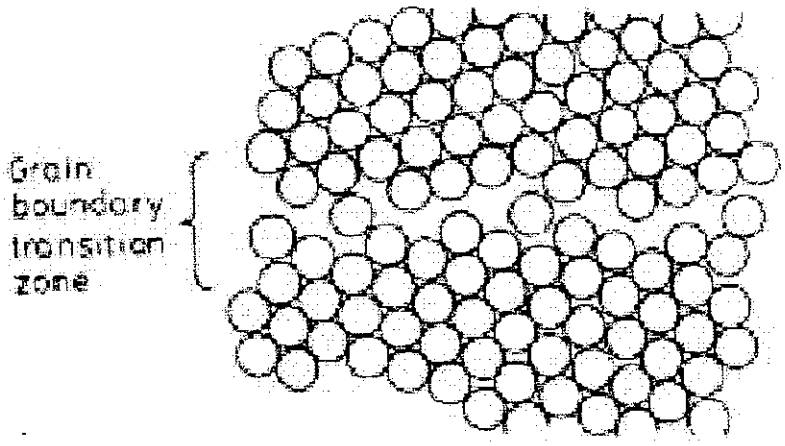

Figure 2: Random High-angle grain boundary transition zone [18]

It has been shown [19] that random high angle grain boundaries absorb lattice defects more readily than CSLs do, and that absorption will progressively be difficult as grain boundaries become more ordered (as Σ value become lowered). As the difference in misorientation between the grains on each side of the boundary decreases, the state of order in the boundary increases [19]. Random high angle grain boundaries are those with high surface energy, where these grain boundaries serve as preferential sites for solid-state reactions such as diffusion, phase transformations, and precipitation reactions. This results in a higher concentration of solute atoms at the boundary than in the interior of the grains. To simplify experimentations, pure metals can be used to minimize most of these solid-state reactions.

2.2.3.1 LAB vs. HAB

The differences between low-angle and high angle grain boundaries are:

- High-angle boundaries contain large area of poor fit while low-angle boundaries contain large areas of good fit.

- For high angle boundaries, the inter-atomic bonds are either broken or highly distorted in the boundary while in case of low-angle boundaries; the inter-atomic bonds are slightly distorted.

- High-angle boundaries have open structures with plenty of free volume while low-angle boundaries have a minimal amount of free volume.

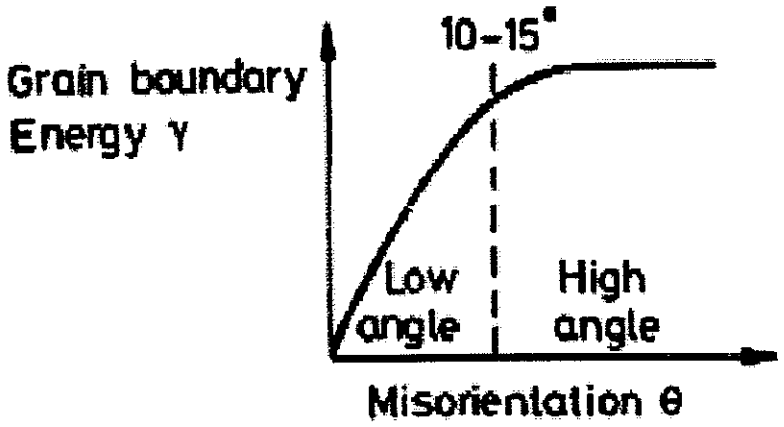

Figure 3: Energy Comparison of Low-angle and High-angle Grain Boundaries [18]

- High-angle boundaries have higher energy then low-angle boundaries, as shown in Figure 3.

- Typical energy values of high angle boundaries are 0.8 – 1.0 J/m^2, while twin boundary energy are lower than 0.1 J/m^2 [19]

2.3 Twin Boundaries

A twin boundary will only form if the total free energy associated with the post-twinning interfacial configuration is less than that of the original configuration [19]. The crystal structure of a pair of twinned grains is identical, but has different orientations in space. The lattice points in one crystal are shared as lattice points in another crystal adding apparent symmetry to the crystal pairs [20]. The twin plane is a mirror reflection that shows the symmetry of crystals of a twin.

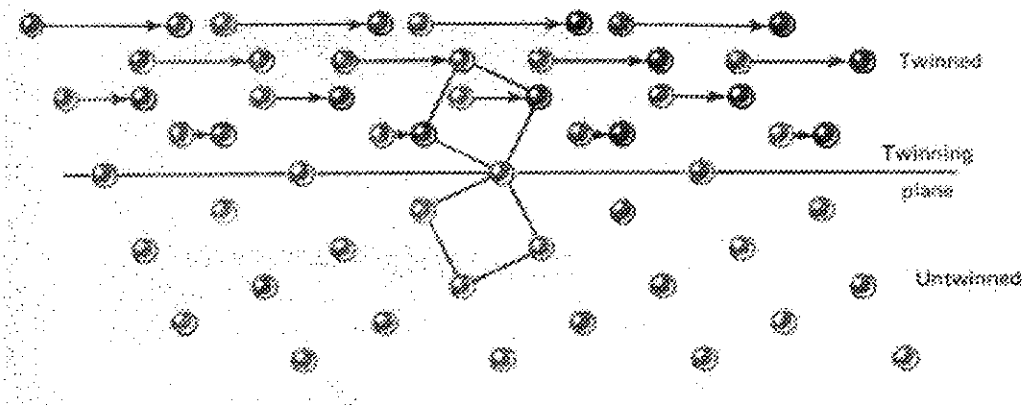

Figure 6: Schematic of simple twinning with black circles represents the atoms with changed positions [21]

Twins have a special orientation relationship since the boundaries separating the twins have a low energy per unit area that enables two crystals to fit together neatly. Commercially pure nickel was found to be prone to twin formation during strain annealing [22], but the presence of impurities could hinder twin formation mechanisms. Due to solute inhibition of twinning, impurities exert a drag effect on grain boundaries, which reduces the occurrence of twin nuclei. The twin boundary interface formed in FCC

is parallel to {111} planes with a stacking sequence ...ABCABCABC... across the boundary.

2.3.1 Mechanical and Annealing Twins

Mechanical twins should be distinguished from annealing twins. The orientation of mechanical twins is generated by a large plastic deformation of a single grain that arranges an entire lattice along a specific plane [20]. The strain energy associated with the formation of a mechanical twin is very high, and the microstructure is determined by the need to minimize strain energy [20]. This contrasts with annealing twins where the shape is determined by the need to minimise interfacial energy to increase CSL proportions.

Annealing twins could form when a crystal grows during recrystallization; and the destruction of newly formed twins was found to be dominant during grain growth [23]. Annealing twins are generally evenly spaced, straight sided and frequently coherent. In contrast, mechanical twins are unevenly spaced, many are bent, and many tail off in irregular fashion within a grain. Annealing twinning occurs by decreasing the overall interfacial energy of the boundaries between grains, and to reorient grain boundaries so as to facilitate dislocation absorption and mobility when reduction in total grain boundary energy is the driving force during recrystallization or grain growth [24].

It has been shown by Randle that twinning is an important part of grain growth in nickel [25]. The process of annealing has to be controlled when a fast boundary migration rate was observed in [25] that it does not to nucleate twins as readily as a slower migration rate. The rate of grain growth is governed by:

$$D - D_o = (Kt)^n \quad (2)$$

Where D is the average grain diameter, D_o is the original grain size, t is the annealing time, K is the rate coefficient for the process and n is the grain growth exponent [25, 26, 27]. The values of K and n are both temperature dependent constants, and the parameter n has a theoretical upper limit of 0.5.

2.3.2 Twins Formation

Twinning phenomenon can be manipulated to form more stable grain boundary configurations; the two categories of Σ3 boundaries are coherent and incoherent twins.

2.3.2.1 Coherent Twins

The coherent twin boundary shown in Fig. 6 is parallel to the twinning plane and normally characterized by a straight edged boundary. The atom positions in this boundary are essentially undistorted. It is accepted that twins, and particularly coherent twins which lie on a 60°/{1 1 1} plane common to both adjoined grains [28], contain a low deviation

v/v_m value from the exact misorientation, low mobility and low energy which would have a low susceptibility to phenomena such as crack propagation [22]. Coherent twins are likely to be sited in the small-grained region than associated with large grains [25]; due to their immobile characteristic, it is to persist in regions where grain growth is static.

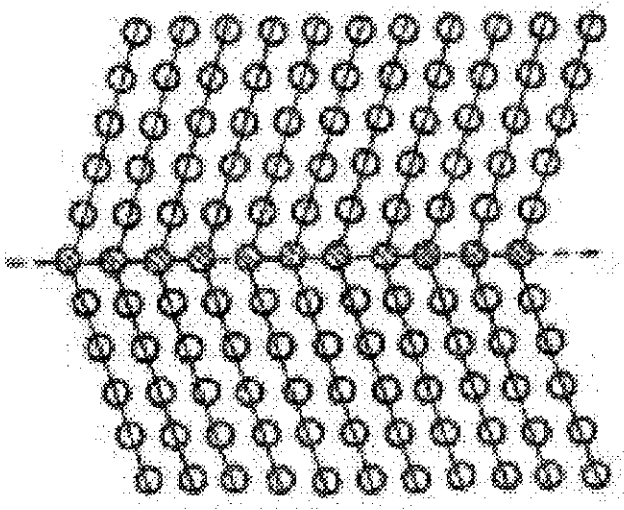

Figure 7: Schematic representation of Coherent Twin Boundary [21]

2.3.2.2 Incoherent Twins

An incoherent twin boundary is not parallel to the twinning plane and is typically curved in appearance. Atoms do not fit perfectly across the boundary, as shown in Figure 7.

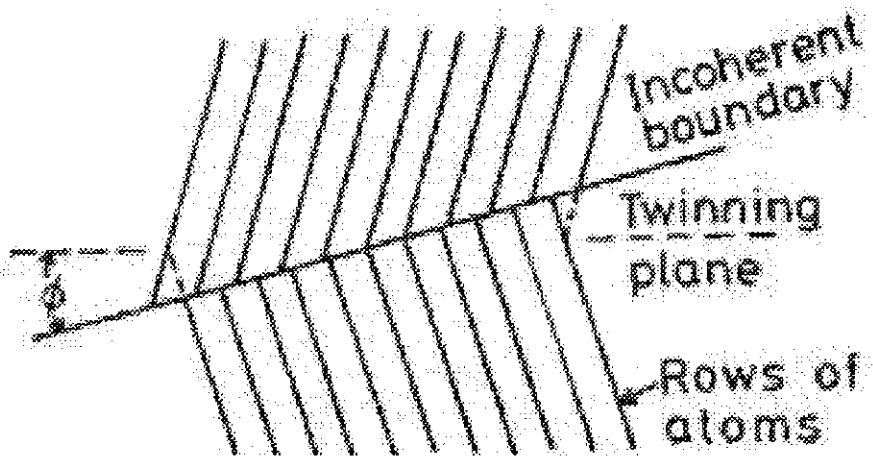

Figure 8: Schematic representation of Incoherent Twin boundary [21]

The energy for incoherent twin boundaries is much higher than for coherent twins; almost ten times the energy of coherent twin boundaries. Although these incoherent twin boundaries have high energy, it is still much lower than random high angle boundaries. The misorientation angle for incoherent twin boundaries could be very high, positive or negative rotation, shown in Figure 9.

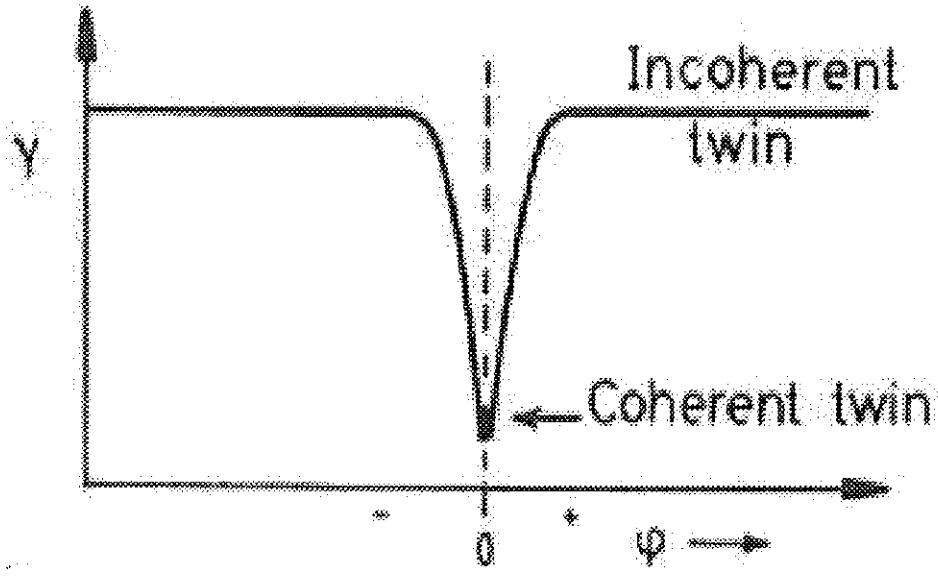

Figure 9: Energy (γ) of a function of misorientation (φ) for Coherent and Incoherent Twins [21]

2.3.3 Factors Affecting Twin Formation

The two factors that exert the most influence on the number of CSLs in a sample are the presence of a strong texture, or orientation of the grain, resulting in $\Sigma 1$ grain boundaries; and the amount of twinning, resulting in $\Sigma 3$ and $\Sigma 3^n$ boundaries [17].

Experimentation performed by Kronberg and Wilson [3] on an annealed cold rolled copper bar for 1 hour at 400°C produced a heavily twinned, cubically aligned structure with a grain size of ~30μm. When the annealing temperature increased to 850°C, consumption of twins occurred while the grain size increased to ~ 80μm. It was observed that grain growth almost always started within the body of the sample, then spread toward the edges.

Low-Σ CSL boundaries have been reported to be low energy configuration [29]. In general, the lower the stacking fault energy, the higher the $\Sigma 3$ proportion [9]. Pande, Imam and Rath have studied the formation of annealing twins in fcc metals, where three models were proposed for the development of annealing twins, which were developed by other authors and re-stated in [26, 27]:

1) Growth Accident model: Coherent twin boundary forms at a migrating grain boundary due to stacking error during grain growth

2) Grain Encounter model: When initially separated grains encounter each other during grain growth, while having twin orientations to each other, the boundary between would become coherent

3) Fault Packet model: A grain boundary during its migration nucleates a twin such that its incoherent segment remains at grain boundary.

Important factors to determine twinning frequency during grain growth were reviewed by Pande, Imam and Rath [27], these are grain size, temperature, time of anneal, velocity of grain boundary migration, grain boundary energy, texture, pre-strain and inclusions. There have been very few studies in the past where all these factors were taken into account.

2.3.4 Multiple Twinning

Majority of grain boundary engineering relies on multiple twinning, resulting in generation of large numbers of $\Sigma 3^n$ boundaries [9]. An increase in overall $\Sigma 3$ numbers is almost entirely as a consequence of the increase in annealing twin numbers [12]. Due to the geometrical properties of triple junctions, the fraction of $\Sigma 3^n$ (where n = 2, 3) may be enhanced, such as $\Sigma 9$ and $\Sigma 27$ [29]. This geometry criterion can be simplified as

$$\Sigma A + \Sigma B \leftrightarrow \Sigma (A \times B) \text{ or } \Sigma A + \Sigma B \leftrightarrow \Sigma (A/B) \quad (3)$$

Where A/B is an integer and A > B. It was found in [19, 24, 29] that coherent $\Sigma 3$ twin boundaries are virtually immobile, and the mobile $\Sigma 3$s are incoherent twin boundaries, which have a higher v/v_m value away from the exact orientation. Hence the meeting of two mobile $\Sigma 3$s leads to a $\Sigma 9$ [30], or forming a $\Sigma 3$ - $\Sigma 3$ - $\Sigma 9$ junction where $\Sigma 9$ is now the most mobile boundary and therefore continues to migrate [24]. If two boundaries at a

triple junction are Σ3 and Σ9, the third junction is either another Σ3 or a Σ27. Other Σ interactions, including the $\Sigma 3^n$ family, were experimentally measured and recorded by Furley and Randle [30]. It was reported that these reactions were likely found during heat treatments as a consequence of either grain growth or grain rotation.

In many investigations [9, 24], the proportion of Σ9 is one-fifth that of the Σ3s and the portion of Σ27s are only slightly higher than that for a random distribution [9]. Furley and Randle observed that the Σ3 family of CSL's can frequently be regenerated when a large source of Σ3s are available from twinning [30]. Multiple twinning was found to be the basis of grain boundary engineering in low or medium-stacking fault energy materials [17].

2.4 Effects of Cold Working and Heat-treatments

Strain hardening or cold working is an important industrial process that is often used to harden metals or alloys. The result of cold working is an altered microstructure, and the mechanical properties of crystalline material vary with direction; this has the effect of rotating the grains so that the grains may have a preferred orientation [31]. Diagram representing the microstructures of a typical cold worked material is shown in Figure 4:

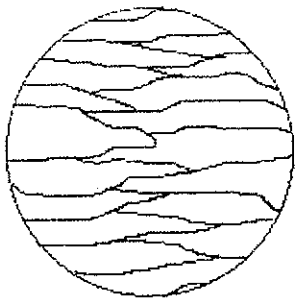

Figure 8: Microstructure of a cold rolled alloy showing elongated grains [33]

In most cases, the effect of cold work is to increase the strength of the metal, but ductility is reduced. It was found that deformation microstructures are characterized by grain subdivision into differently oriented regions [32]. The long boundaries shown in Fig. 4 are arranged in parallel and have orientations with respect to the deformation axis. At medium to high strains, some population of grain boundaries increased in misorientation angle to the extent that would be classified as high angle boundaries. Deformation induced high angle boundaries contains high stored energy, which is the driving force in the formation of new grain structure upon heating.

A post deformation anneal performed at the correct temperature and for the right amount of time should modify these structures to produce a microstructure showing fine equiaxed grains as seen in Figure 5:

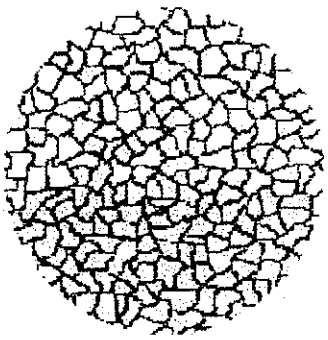

Figure 9: microstructure of a strain - annealed alloy [33]

Cold working processes and heat treatment can be used to alter the structure of a material to improve its properties [32]. These structure-altering procedures are often employed in combination to achieve desired results. The process of recrystallization was used to describe the formation of a new grain structure in a deformed material by the formation and migration of high angle grain boundaries driven by the stored energy [32]. It was found [34] that the time for recrystallization decreases as annealing temperature is increased. Recovery includes all annealing processes releasing stored energy without the migration of a high angle grain boundary. Typical recovery processes involved with the formation of low angle boundaries to lower boundary energies [32]. Grain coarsening is another boundary energy minimization process involved with migration of grain boundaries to increase the mean grain size, which were driven by the reduction in grain boundary area per unit volume [34].

2.5 Thermo-mechanical Processing

Grain boundary engineering focuses on manipulating the structure of grain boundaries to permit property improvements. The Coincidence Site Lattice (CSL) model is a geometrical construction based on the geometry of the lattice. When a fixed fraction of lattice sites are coincident, the expectation is that the boundary structure will be more regular than a general boundary [35]. The initial texture of the material is an important factor with a high proportion of grains having nearly the same orientation, resulting in a large number of low angle boundaries to improve intergranular properties [36]. Low-Σ CSL grain boundaries were found to naturally occur in all polycrystalline materials; their frequency of occurrence is strongly dependent upon the processing history of the material [35].

As was stated by Watanabe 1984 [37], thermo-mechanical treatment can alter the crystallographic orientation of a grain. A driving force such as the stored energy of cold work is required to overcome the barrier to energy minimization of grain boundaries. Controlling thermo-mechanical processing conditions may lead to an alteration of the type of boundaries and increase the frequency of low-Σ special grain boundaries [38] to improve material properties.

Watanabe tested Fe-0.8 atomic % Sn alloy for intergranular fracture failures [35], and results showed that fracture occurs preferentially at random boundaries under high normal stress. Two common types of fracture paths were considered: zigzag path and

planar path [37]. The zigzag path was formed by interlinkage of intergranular fracture, and the planar path was formed by transgranular fracture that produced a relatively smooth fracture surface with fracture surface waviness, much less than that of zigzag path [39]. When the frequency of random boundaries were high, they were more likely to be linked to each other, and a crack nucleated at a random boundary would continue to propagate selecting random boundaries at every triple point for further propagation [5]. Evidence [37, 39] showed low-Σ CSL boundaries were difficult paths for crack propagation due to their high fracture resistance; therefore, it is beneficial to manipulate grain boundary structures to increase the proportion of low-Σ CSL boundary distributions.

2.6 Grain Boundary Population Variation

Many publications have reported the conscious exploitation of thermo-mechanical treatments to increase special grain boundary populations. Different methodologies to improve the number of low-Σ CSL boundaries have been employed by various research groups. Processes used to increase the proportion of low-Σ CSL boundaries can be categorized as the following [9]:

- Multiple step recrystallization
- One step recrystallization
- Multiple step strain annealing
- One step strain annealing

2.6.1 Multiple Step Recrystallization

Palumbo along with other workers have demonstrated [40] that increasing the relative proportion of special low-Σ CSL grain boundaries can improve high temperature intergranular degradation susceptibility and weldability of Nickel and Iron based Superalloys. Three different types of alloys were analysed: Alloy 625, Alloy V-57 and Alloy 738. Thermo-mechanical treatments involved were a series of deformation (5% to 30% thickness reduction) and recrystallization – anneal steps at temperatures ranging between 975°C and 1200°C for 2 to 10 minutes. These parameters were chosen to ensure recrystallization was effected without excessive grain growth. The effects of processing the alloys were analysed and recorded as follows: the frequency of special low-Σ CSL boundaries increased by an absolute value of 45.9% for Alloy 625, 38.3% increased for Alloy V-57 and a 36.9% increase for Alloy 738. A table of special boundaries with $\Sigma \leq 29$ are listed below showing each sample's initial and final special boundaries percentage:

Table 1: Distribution of special boundaries for the three alloys

Sample	Initial Special Boundaries	Final Special Boundaries
Alloy 625	24.8%	70.7%
Alloy V-57	21.4%	59.7%
Alloy 738	9.6%	46.5%

As the proportion of low-Σ CSL boundaries increased, all of the mechanical properties tested for these alloys also increased, showing that a high frequency of low-Σ CSL special grain boundaries could significantly enhance alloy performance, such as intergranular stress corrosion cracking [41, 42].

King and Schwartz [43] have used a two-step strain – anneal processing in fully recrystallized oxygen-free electronic (OFE) copper to increase the fraction of special boundaries. Heat-treatments for the OFE copper are shown in table 2:

Table 2: Strain – anneal treatments for Oxygen-free electronic copper

	OFE-1	OFE-2	OFE-3	OFE-4
Strain (%)	-7	-6	-6	-6
Heat-treatment	8hr / 344°C 14hr / 532°C	14hr / 275°C 7hr / 375°C	14hr / 225°C 6hr / 325°C	6hr / 325°C

Low strain deformation applied was intended to not induce full recrystallization upon heating, but to localize the deformation energy at random boundaries [43]. Upon heat-treatment, the stored energy near random boundaries was expected to provide sufficient driving force to rearrange these boundaries into special types [43]. Samples were analysed using EBSD from an OIM system. The initial material was recrystallized and showed a total fraction special boundaries of nearly 70%, where $3 \leq \sum \leq 29$ were considered as special boundaries. Final fractions of special boundaries recorded were:

Table 3: Fraction special boundaries of OFE 1-4

	OFE-1	OFE-2	OFE-3	OFE-4
Special Boundaries (%)	55	85	82	79

The effect of heat-treatments on OFE-1 decreased the fraction of special boundaries. It was indicated that a significant and undesirable increased in grain size was the cause of the problem. OFE-2, 3, 4 strain – annealing treatments all exhibited increased in special boundaries compared to the starting material. Observations made on these samples found

that the average deviation from exact misorientation decreased, at the same time the $\Sigma 3^n$ fraction increased [43]. This was a consequence of the final anneal; high temperature anneal resulted in a reduction of special boundaries (OFE-1), and lower temperature treatments resulted in an increased fraction of special boundaries (OFE 2,3,4).

2.6.2 One Step Recrystallization

Romero and Murr [44] studied lamellar carbide growth with annealing twins in 304-stainless steel. Concepts of understanding the directional growth of carbide precipitates in austenitic stainless steels, in the context of coherent annealing twins and crystallographic issues with twin/grain boundary intersections were studied. The experimental technique used was to strain and anneal 304-stainless steel to observe the change in lamellar growth direction with annealing twins. The material had an initial grain size of 50μm. It was cut into strips and cold-rolled to 70% reduction, annealed at 1000°C for 1 minute to produce a recrystallized grain size of 15μm. The small grain size produced was desirable to locate annealing twins in the Transmission Electron Microscope (TEM). Some samples received further processing of 10%, 15% and 20% uniaxial tensile strain at room temperature and aged at 625°C and 775°C for times up to 50hours. Results regarding to coincidence boundaries or the amount of twinning was not reported, only the direction of lamellar growth and the resolved extensive coherent twin boundary formation were considered.

Lim and Raj [29] performed thermo-mechanical processing experiments, utilizing tensile strain followed by subsequent annealing for 270-grade Nickel. The focus of this paper was to maximize the amount of low-Σ CSLB, knowing that a high proportion of CSL boundaries could improve material's property. The experimental technique applied was 5% strain in the uniaxial direction at room temperature, annealed at 1300°C ($0.9T_m$) with flowing argon for 10 minutes. The high temperature anneal resulted in an average grain size of about 1mm. Lim and Raj [29] explained the reason for enlarged grain size was that twinning occurs readily during high temperature anneals; and their mutual impingement would result in the formation of CSLs, which were crystallographically related to the $\Sigma 3$ orientation. The initial special boundary percentage for this material was not clearly stated. Results from a total of 222 boundaries were evaluated for this recrystallized polycrystal, only 36% were random boundaries and 64% low-Σ CSLB.

Table 4: Results of the occurrence of CSLs in grade 270 pure nickel [29]

CSL	$\Sigma 3$	$\Sigma 9$	$\Sigma 27$	$\Sigma 81$	Other $\Sigma \leq 97$	Random
Percentage (%)	41.0	9.0	5.8	1.8	6.4	36

It should be noted that $\Sigma > 97$ were considered as random boundaries. The reason was due to a greater incidence of $\Sigma 9$, $\Sigma 27$ and $\Sigma 81$ twin related boundaries found. These $\Sigma 3^n$ twin related boundaries originated from a geometrical model of $\Sigma 9$ boundaries created by the impingement of two $\Sigma 3$ boundaries [29], where the impingements of growing grains have $\Sigma 3$ relationships during high temperature anneal. As a result, $\Sigma 3^n$ boundaries have a higher proportion of special boundaries than other CSL boundaries.

Lin, Palumbo and Aust have also used one-step strain – anneal recrystallized Cu, Stainless Steels and Ni-based alloys to alter the frequency of twinning [45]. Materials were cold rolled in the range of 10% - 67% and subsequently annealed at 1000°C (600°C for Cu) in an argon atmosphere for 5 minutes, followed by air-cooling to achieve fully recrystallized structures. Electron Backscattered diffraction technique was used to analyse CSL distributions and annealing twins. A significant result obtained was the maximum frequency of twin boundaries $\Sigma 3^n$, occurred at 61%, which was proved to be consistent with the theoretical limit of 2/3, proposed by Palumbo et al [Palumbo et al., 1992]. The maximum frequency of special boundaries $\Sigma 1$ - $\Sigma 29$ was 83.2% processed using Alloy-600. It was found [45] that high occurrence of $\Sigma 3^n$ grain boundaries was attributed to the geometric interaction of twin related variants.

2.6.3 Multiple Step Strain Annealing

One of many experiments to increase the proportion of $\Sigma 3$ boundaries by multiple steps strain annealing technique was found by Thaveeprungsriporn and Was [36, 46] using Nickel based alloy Ni-16Cr-9Fe (Alloy 600). It was found that the average creep rate decreased by an order of magnitude when the number of CSLBs increased from 1/6 to 1/3 of the total boundary population. Two different grades of Ni-16Cr-9Fe alloy was used, UHP8 and UHP9. The compositions of weight percentage listed in table 5:

Table 5: Nominal Composition of Ni-16Cr-9Fe Alloys (wt %) [36]

Alloy Designation	Ni	Cr	Fe	O	C
UHP8	bal	17.0	9.3	0.0029	0.0004
UHP9	bal	16.6	9.2	0.0022	0.0008

The processing route used to improve the number of CSLBs was to initially anneal samples at 1025°C under flowing argon for 20 minutes, followed by a water quench. After receiving a 45% thickness reduction, some specimens were given a heat-treatment of 800°C for 1 hour; and others were heat-treated at 800°C for 10 minutes followed by a sequence of deformation and annealing stages (two or three stages), where the deformation level was a relatively small tensile strain, in the order of 2-5%, followed by annealing in the range of 890°C to 940°C for 1-20 hours. Samples from the UHP9 alloy required an additional treatment of 2% tensile strain and heat treatment of 900°C for 7.5 minutes to achieve a comparable grain size of 35μm.

Two different types of samples were produced; solution annealed (SA) samples and coincident-site lattice enhanced (CSLE) samples. SA samples are those containing mostly random boundaries and CSLEs are coincident site lattice enhanced samples with high fractions of special boundaries. Results of SA and CSLB samples are listed as follow:

Table 6: GBCD of the SA and CSLE Tensile samples [36]

Alloy	Sample Designation	Fraction of Random High Angel Boundaries	Fraction of CSLB (Σ1 - Σ49)	Fraction of Twin Related Boundaries (Σ3+Σ9+Σ27)
UHP8	SA	0.84	0.16	0.11
UHP8	CSLE	0.70	0.30	0.25
UHP9	SA	0.82	0.18	0.07
UHP9	CSLE	0.60	0.40	0.33

Higher fractions of CSL boundaries and twins were found in CSLE samples compared to SA samples. It is worth noting that the upper limit of Σ was Σ49, based on the work of Shvindelerman and Straumal found in [7]. Alloy UHP9 resulted in higher CSLB and twin fractions than alloy UHP8. Additional strain – anneal treatment and the metal purity were main reasons for the elevated special boundaries proportion of UHP9. Was [36] described the reason for these CSLBs to have good properties during deformation was their ability to increase the internal stress by trapping run-in lattice dislocations at the grain boundaries as extrinsic grain boundary dislocations (EGBDs), creating back-stresses on following dislocations rather than annihilating them, as in the case of high angle grain boundaries. It was observed from the literature that the processing sequence and the duration of anneal was not clearly explained; the methodology leading to the increased in special boundaries can not be readily understood.

Douglas and Was [7] have also used Ni-16Cr-9Fe alloy (Alloy 600) to analyse the effects of grain boundary misorientation on intergranular cracking behaviour of CSLBs and general high angle boundaries (GHABs). Tests were conducted by constant extension rate tensile tests (CERTs) in 360°C flowing argon and in deaerated high purity water

atmosphere. The experimental procedure was set-up similar to Thaveeprungsriporn and Was' paper, where samples were initially annealed and followed by multiple step thermo-mechanical processing listed below:

Table 7: Thermo-mechanical Processing steps of Alloy 600 [7]

Ann.	1200°C: 1hr
Seq. 1	Ann. + 5% tensile strain + 945°C: 75min. + 2% tensile strain + 890°C: 15hr + 3% tensile strain + 890°C: 20hr
Seq. 2	Ann. + 5% tensile strain + 890°C: 16hr + 3% tensile strain + 890°C: 20hr

The proportion of CSLBs found in solution annealed (SA) samples was 12 to 20 percent, and the coincident-sited lattice enhanced (CSLE) samples contained 27 to 44 percent CSL boundaries, for $\Sigma \leq 49$, not including coherent twin boundaries. These samples also showed that CSLBs are more crack resistant than GHABs in either environment, and both types of boundaries are more crack resistant in argon than in water. The result of characterizing these low-Σ CSL boundaries effectively block dislocation movements, generating back stresses within the material to reduce creep rate and intergranular stress corrosion cracking [7]. All of the Σ CSL boundaries were collected manually, possible fewer special boundaries analysed than if it were to be done by automated systems. It should also be noted that coherent twin boundaries were excluded from the analysis because the authors recognized that many experiments have verified coherent twin boundaries encompass good mechanical properties, hence a lower fraction of CSL boundaries was apparent compared to other investigations.

Thermo-mechanical processing of Inconel 600 and OFE-Cu has shown an increase in the relative fraction of special boundaries, investigated by Kumar, Schwartz and King [47]. Treatments used for Inconel 600 were 20% thickness reduction, annealed at 1000°C for 15 minutes in air followed by a water quench. The same sequence of strain – anneal was performed for seven trials. OFE-Cu received similar sequential treatments as Inconel 600, which the applied strain was 20%-30%, annealed between 500°C and 600°C for 15 minutes. EBSD observations revealed both materials showed increase in the fraction of special boundaries with each processing cycle, and a reduction in connectivity of random boundaries as the fraction of special boundaries increased.

2.6.4 One Step Strain Annealing

A variety of thermo-mechanical treatments have been tested with commercially pure Nickel (99.5% pure) to study twin formation during strain-annealing processes [9, 12, 19, 22, 25, 48]. The presences of low-Σ CSL boundaries and annealing twins have been associated with favourable properties such as resistance to corrosion and intergranular fracture [22]. Thermo-mechanical processing details of Thomson and Randle's experiments are shown in Table 8:

Table 8: Strain annealing processing details of commercially pure nickel [22]

Sample	Strain	Strain Rate	Thermal Processing
A	-6%	None	None
B	-6%	Fast	12hr / 750°C (vacuum) + 12hr / 750°C (air)
C	-6%	Fast	9hr / 500°C (air) + 12hr / 750°C (air)
D	-6%	Fast	9hr / 500°C (air) + 12hr / 750°C (air)
E	-6%	Fast	9hr / 500°C (air) + 12hr / 750°C (air) + 20min. / 1000°C (air)
F	-6%	Slow	24hr / 750°C (vacuum)
G	-6%	Fast	9hr / 500°C (air) + 12hr / 850°C (air)

Samples were forged using a low compressive strain (i.e. 6%) at room temperature, followed by thermal treatments performed either in air or under vacuum to determine if the resultant precipitation of oxide may affect the recovery mechanism, and twinning in particular. Single step and multiple steps strain-anneal treatments were tested and analysed for low-Σ CSL boundaries and twin boundaries.

Sample A was the reference specimen, received no strains or heat treatments. The difference between samples C and D was that sample D was produced from sample C by removing a surface layer to compare the twinning processes in the bulk and surface regions. Other samples were processed as outlined in the Table 8 and the results are summarized in Table 9.

Table 9: Results of twinning frequency and LAB (approximate values) [22]

Sample	Twinning Frequency (%)	Frequency of LAB (%)
A	15.3	6.9
B	26.2	5
C	39.8	2.5
D	27.2	5.3
E	33.8	2.4
F	27.5	8.5
G	37.9	1.8

Results obtained in Table 9 were based on the percentage twinning ($\Sigma 3$), coherent and incoherent twins, and the frequency of LAB occurrence. Data regarding $\Sigma \leq 29$ boundaries were not given. Coherent or incoherent twin boundaries were clearly distinguished by the authors, using Brandon's criterion.

It was described in the paper that the annealing temperatures selected at 750°C or below were low enough to ensure that recrystallization does not occur in the annealing time allowed, but the recovery mechanism is still operative [22]. Only the 850°C and higher treatments were sufficient to activate grain boundary migration resulting in grain growth.

Experiments involving 2- 5 stages of iterative thermo-mechanical treatments enhance the portion of twins [9] more than a single stage treatment. While the twin fraction decreased slightly during the first anneal, as it was found to be a necessary step in the evolution of the final fraction of CSLs [24]. It was found that multiple strain-anneal treatments resulted in a high proportion of secure triple junctions [12], with increased low-Σ CSL boundary populations. A secure triple junction is one where at least two of the adjoining interfaces are of the low-Σ CSL type, which can be considered to possess special properties [12] against detrimental effects such as intergranular crack propagation. A high proportion of secure triple junctions have proven [12] to enhance various mechanical properties of the material.

It was shown in [25] that increasing the annealing temperature could increase the twinning proportion for commercially pure nickel. Moderate grain growth or increase in grain size initiated the grain boundary migration process to form annealing twins [25, 48]. A fast rate of grain growth could cause a fast boundary migration which in turn drastically reducing the total grain boundary area, rendering twinning redundant [25]. A low strain rate (0.000833mm/s) increased the proportion of low angle boundaries, as well as twin boundaries. The reason was that samples strained at a lower rate were inclined to spread the strain more uniformly, leading to a higher density of lattice dislocations, resulting in greater levels of polygonization occurring in the grains during annealing [24].

The temperature of anneal should also be controlled when a fast boundary migration rate did not nucleate twins so readily as at slower migration rate, as shown in Table 9. The annealing temperature was sufficiently high that grain boundary migration can be activated as a process by which the overall free energy was reduced, and some degree of grain growth was needed to avoid initial strains to be absorbed into the grain boundaries [48].

It was also found that twinning could be influenced by specimen purity. A significant level of impurity was found in commercially pure nickel [25], which provided preferential sites for oxygen to precipitate at grain boundaries. Impurities hinder twin formation mechanisms [25] by solutes saturating at grain boundaries, and hampering grain boundary migrations during recovery. Samples annealed in a vacuum atmosphere were found to minimize this effect. Both the degree of plastic strain and annealing

temperature were two major factors to provide the driving force for the grain and grain boundaries to rotate to a more stable orientation.

2.7 Effects of Grain Size

Grain size has been taken as one of the important factors to fractures in polycrystalline materials. Watanabe found the frequency of random boundaries increases as grain size increases [6]. The frequency of low angle boundaries and coincidence boundaries decreased with increasing annealing temperature [8], when Fe-3 mass% silicon alloy was tested. Watanabe explained this behaviour in [35] that low-Σ boundaries generated at early stage of nucleation are modified to random grain boundaries during grain growth. In-turn, the frequency of random boundaries increases for a high annealing temperature. Palumbo et al. have also shown [49] that decreasing grain size could significantly improve the intergranular cracking resistance of Ni-base material.

The opposite effect was found in another of Watanabe's experiments [35], when iron-silicon alloy ribbons was rapidly solidified and annealed, the frequency of low-Σ boundaries increased with increasing grain size. It was then stated [35] that GBCD strongly depend on processing methods, grain size dependence of GBCD differs between polycrystalline materials produced differently.

Pande, Imam and Rath established a relationship for grain size 'D' and twin density 'p'. The mechanism of the formation of annealing twins was studied using strain – anneal treatments in pure nickel [26, 27].

$$(p / p_o) = (D_o / D) \log (D / D_o) \quad (4)$$

Where p_o and D_o are constants (scaling factors), that are independent of temperature. It was found in [26] that grain size is an important factor, where twin density was determined uniquely by grain size; twin density 'p' decreases with increasing grain size for sufficiently large grains.

Was, Thaveeprungsriporn and Crawford's experiments [10] used Ni-based alloys to characterize CSL boundaries, and the mean grain size was controlled to 35μm and 300μm, using the strain and anneal technique. A figure in [10] reported the difference in grain boundary character distribution of coarse grain samples and small grain samples. The results showed coarse grain samples (300μm) contained a higher frequency of low-Σ boundaries ($\Sigma \leq 49$) than small grain samples (35μm).

Randle's previous work involved with recrystallization and grain growth as energy minimization process. Evidence in [50] showed that smaller recrystallized grains were more likely bordered by a high proportion of low-Σ boundaries than are larger recrystallized grains. It was also found in [25] that an increased in twinning in commercially pure nickel with increasing grain size. An important feature reviewed was

that specimen purity could significantly influence twinning proportion; impurities hinder the twinning mechanism of twin nucleation as grain boundaries migrate. The relationship between temperature and grain size with respect to grain boundary characteristic is that insufficient thermal treatments would not bring about boundary migrations, while excessive grain growth could destroy special boundaries.

Grain size has always been taken as one of the important microstructural factor and to be related to characteristic features of fracture in polycrystalline materials [37]. In fact, grain size itself is not sufficient in discussing the brittleness associated with intergranular fracture [35]. It can only determine the density or the spacing of grain boundaries; it does not describe the structure [37], or the connectivity between like or unlike grain boundaries [5]. It is now known that the types of grain boundaries and the frequency of different types of grain boundaries produced by specific processing have a large effect on the resultant characteristics of the polycrystalline material.

2.8 Extended Time of Anneal Processing

Increase in annealing times (greater than 168 hours) with single step or multiple steps processing have been shown by Randle [19] to improve the grain boundary population, by shifting the average v/v_m ratio for $\Sigma 3^n$ s to lower values. The thermo-mechanical treatments for extended periods of anneal is detailed in table 10.

Table 10: Table of Heat-treatments for 99.999% pure nickel [9]

Sample	Thermo-mechanical Treatment (in air)
1	$\varepsilon_1 = -6\%$, $T_1 = 850°C$, $t_1 = 168hr$
2	$\varepsilon_1 = -6\%$, $T_1 = 850°C$, $t_1 = 168hr$, $\varepsilon_2 = -6\%$, $T_2 = 850°C$, $t_2 = 24hr$
3	$\varepsilon_1 = -6\%$, $T_1 = 850°C$, $t_1 = 168hr$, $\varepsilon_2 = -6\%$, $T_2 = 850°C$, $t_2 = 48hr$
4	$\varepsilon_1 = -6\%$, $T_1 = 850°C$, $t_1 = 168hr$, $\varepsilon_2 = -6\%$, $T_2 = 850°C$, $t_2 = 168hr$

The overall population of coincidence site lattice boundaries did not increase with extended annealing times. It was found however that the proportion of $\Sigma 3^n$s, which approach the exact $\Sigma 3$ configuration, was increased. As the total $\Sigma 3$ proportions remained static during heat-treatments, the reduction in mean deviation from exact misorientation is the result of an adaptation of existing grain boundary network, rather than the generation of new twins [19]. The term 'fine tuning' was proposed to describe this type of behaviour. The CSL boundaries of $\Sigma 9$ and $\Sigma 27$ can progress towards to a closer CSL matching than $5 \leq \Sigma \leq 29$, due to the potential for grain boundary energy reduction is greater at $\Sigma 3$ and $\Sigma 3^n$s; where $\Sigma 9$ and $\Sigma 27$ are attributed to the geometrical necessity of $\Sigma 3$ [19].

2.9 Material

Commercially pure (99.5%) wrought Nickel has a Face Center Cubic structure, which represents spheres of uniform size are in the closest packing. The planes in this fcc structure are stacked in the sequence ABCABC [34]. It was shown in many research [20, 22] that the most stable coherent twin boundaries exist when twin interface is parallel to the {1 1 1} plane.

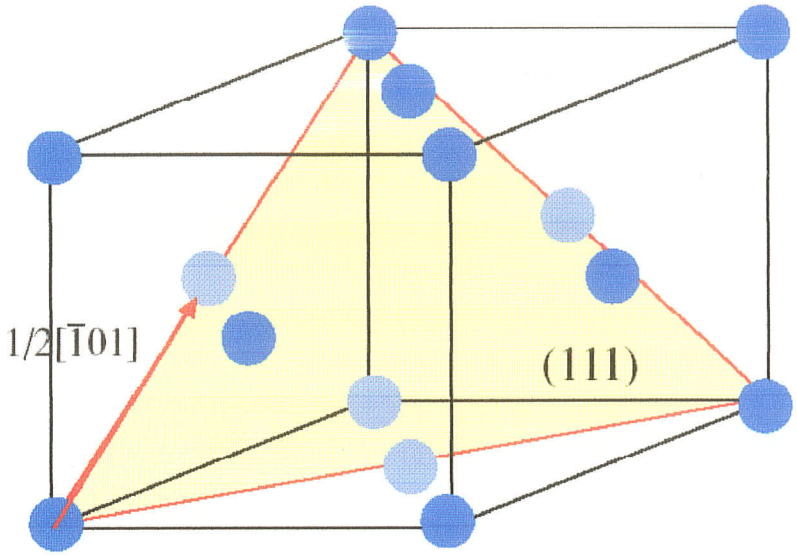

Figure 10: Picture of an fcc cubic structure with {1 1 1} plane [33]

2.10 Grain Boundary Network

Grain boundary connectivity was described as the geometrical configuration of different types of grain boundaries [51], which may control a dominant fracture mode and the probability of continued intergranular crack propagation in a polycrystal. High angle random boundaries were found to be preferential sites for crack nucleation and propagation [8]. The arrows shown in Figure 11 indicate possible crack propagation paths from a primary crack. Random boundaries labelled 'R' are general high angle boundaries, while low angle boundaries and coincidence boundaries are represented by 'L' and 'Σ' respectively. In Figure 11, transgranular (left bold lines) and intergranular (right bold lines) cracking are different crack propagation modes observed in polycrystals.

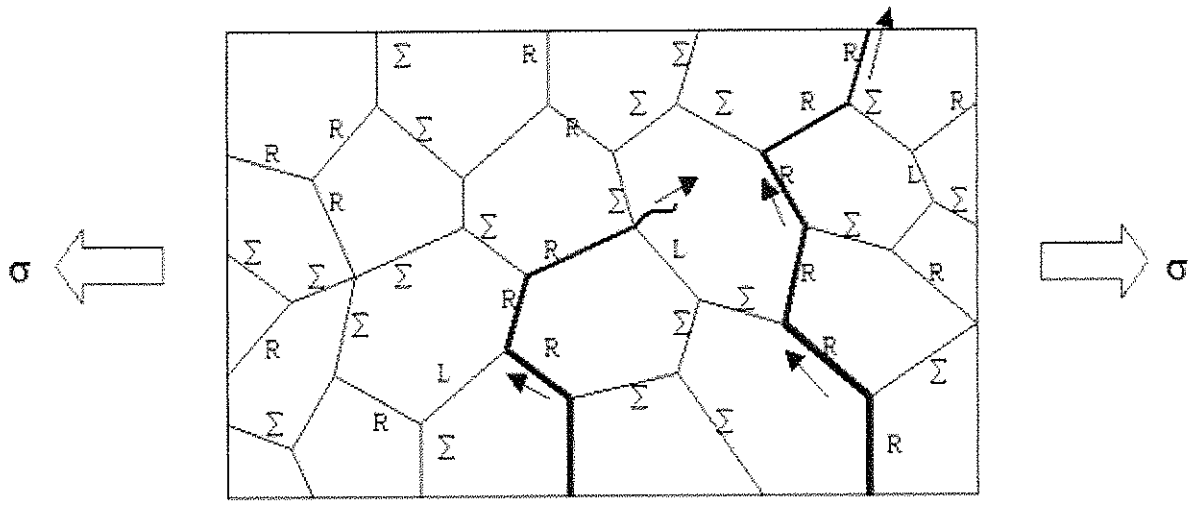

Figure 11: Schematic representation of grain boundary structure fracture [37]

Intergranular fracture generally depends on the boundary type [8]. Premature cracks formed preferentially at random boundaries and tend to connect to each other and propagate onto other random boundaries [5]. When a high frequency of random boundaries is contained in a polycrystal, chances of these weak boundaries to interconnect would increase. Once a crack nucleates, it can easily propagate along these random boundaries, resulting in possible material failure.

Watanabe [5, 6, 37, 51] described the concept of breaking up the connectivity of random boundary network by the introduction of low angle grain boundaries and twin boundaries. Schwartz, Kumar and King [52] and Schuh et al. [53] showed improvements of breaking-up random boundary network after subsequent thermo-mechanical processing cycles of Inconel 600. A sharp decreased in the relative frequency of random boundaries beyond one-step processed cycle. The network of random boundaries in the

microstructure of Inconel 600 in Figure 12 shows the break-up of random boundary connectivity as a result of sequential processing of 30% deformation annealed at $0.8T_m$.

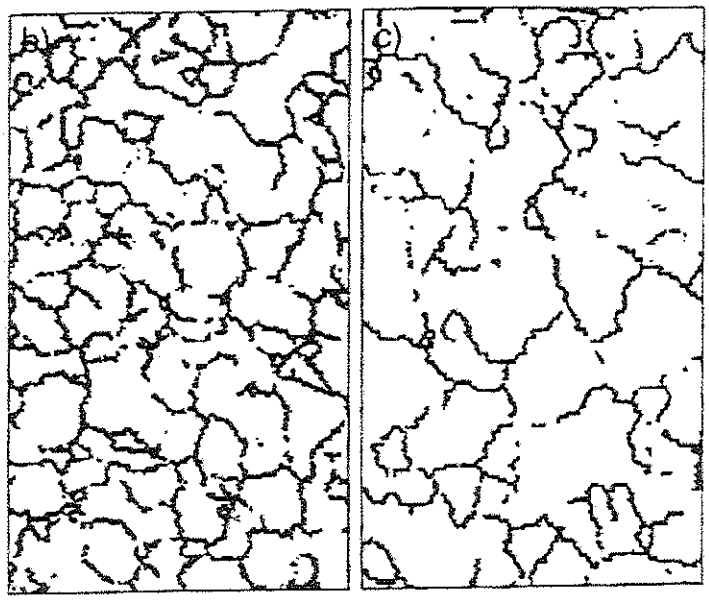

Figure 12: Misorientation map of break-up of random boundary network for the case of sequentially processed Inconel 600 [52]

Schuh et al. [53] identified a flaw to this concept that increasing special boundary fraction alone was not a good predictor of the network topology; it does not describe the size and size distribution of random boundary clusters. The authors suggested the criterion based on the triple junction distributions were more reasonable for ranking processes to break up random boundary connectivity.

Guo et al. [54] showed modification to the grain boundary character by intersection of twin boundaries to liquated grain boundaries during welding. Almost all the liquated boundaries were found to be random type and twin boundaries were never observed to liquate [54]. It was reported that twin intersected grain boundary exhibits

different types of characters and exhibits different resistance to intergranular liquation. Segments of liquated boundaries were rescued by twin boundaries intersecting with the high angle boundary and modifying the character of this boundary with segment of low-Σ types.

Randle [12] has shown increased in Σ3-boundary fraction promotes the formation of triple junctions comprising of 3-CSL boundaries, where three of the adjoining interfaces are of CSL type boundary using commercially pure nickel (99.5% pure). The result of secure triple junctions showed minimizations of detrimental effects, such as intergranular crack propagation [12] and stress corrosion cracking [42]. Was et al. [55] also witnessed a crack that initiated on a CSLB segment was stopped from advancing to the adjacent HAB by the twin intersection in Ni-16Cr-9Fe-xC alloys. This demonstrates rather a rare situation of the role twins played in for arresting grain boundary crack propagation, considering cracking of CSLBs is less common than HABs.

2.11 Electron Back-Scattered Diffraction (EBSD)

Kikuchi was the first to observe electron diffraction, through a thin mica crystal in 1928 [56]. This was also the first recorded observation of a divergent beam diffraction pattern, a description of the technique that now carries his name, Back-scattered Kikuchi Diffraction (BKD). With continuous developments of Scanning Electron Microscope through 1960's, the technique for microtexture developed and was known as the Electron

Backscatter Diffraction (EBSD) system. From then on, grain boundary characteristic distributions could be determined by analyzing backscattered diffraction data.

2.12 Scope of Present Investigation

In summary, grain boundary engineering was developed two decades ago to promote high proportions of special grain boundaries or low-CSL boundaries by applying strain and anneal technique. As can be seen from the literature survey, both low and high strain, as well as single and multiple processing have been used. The beneficial effects of increasing these special boundaries have shown to improved mechanical properties of the material during service.

As shown in previous sections of the literature review, changes in the frequency of special grain boundaries have been observed for various thermo-mechanical processing. However, there is a lack of information regarding the mechanism operative in such microstructural changes. In addition, there are no references in the literature directly concerned with evaluating key processing characteristics and their interactions that directly influence low-Σ (≤ 29) formation.

Keeping this background in view, the present investigation was undertaken in order to acquire comprehensive understanding of the mechanisms involved in producing high proportions of low-Σ boundaries and the influence on grain boundary connectivity. Due to microstructural complexity of alloys, commercially pure nickel or Ni-200 (99.5%

pure) was used to minimize solute inhibition of twinning, thereby reducing drag effects on grain boundaries during the occurrence of twin nuclei. Nickel provides medium stacking fault energy to enable twinning or twin related boundaries to occur [29] to increase the CSL boundary population.

Samples were heat-treated in an argon atmosphere to avoid oxygen precipitation within the grain boundaries, hindering grain or grain boundary rotations. Processing parameters to control the thermo-mechanical processing are the amount of deformation (3% to 12% tensile strain), annealing temperature (500°C to 1000°C) and the time of anneal (10min. to 168hours). The strain and anneal technique used were in combination of three processing parameters; varying degrees of low strain, annealed at above and below the recrystallization temperature and the time of anneal. The electron Backscatter Diffraction (EBSD) technique was employed to microscopically analyze these grain boundaries, with the objective to increase the level of low-Σ CSL boundaries greater than 50%. In addition to understanding the key process characteristics controlling the generation of special boundaries (Σ3 - Σ29), a processing model was also developed relating fraction special boundaries to processing parameters.

Chapter 3

EXPERIMENTAL PROCEDURE

3.1 Chemical Composition of Ni-200

Pure nickel has relatively good mechanical properties over a wide range of temperature, and excellent resistance to many corrosive media. The chemical composition of the commercially pure Nickel (Ni-200) used is given as:

Table 11: Limiting Chemical Composition, wt. %

Ni	Co	Cr	Cu	Fe	Mn	Mo	Nb	Ti	W
Bal	0.0006	0.009	0.052	0.021	0.18	0.00036	0.00024	0.023	0.00037

Ni-200 has good resistance to corrosion in acids and alkalis and is most useful under reducing conditions, but it is also severely attacked in oxidizing salt solutions [57]. It is used for a variety of processing equipment, particularly to maintain product purity in handling foods, synthetic fibres, and alkalies [57].

3.2 Sample Preparation

The material was received as a square sheet of 1.2m X 1.2m, cut into many strips of 12.5mm wide and machined according to the ASTM E8 specification.

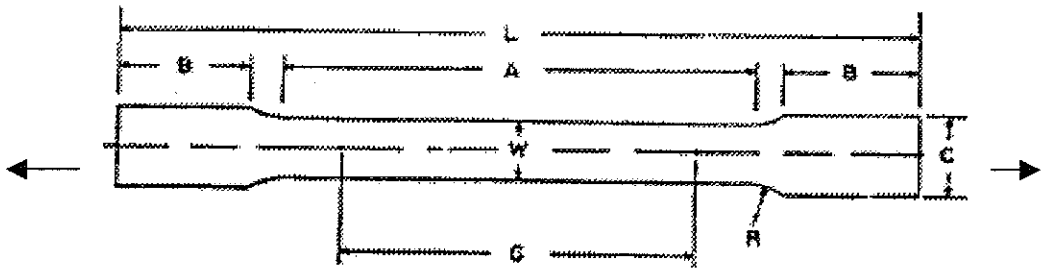

Figure 13: Schematic representation of machined standard tensile sample [58]

The values of gauge length, width and thickness are given as follows:

Legend	Dimensions
Gauge Length (G)	65.0mm
Width (W)	12.5mm
Thickness	3.25mm

All the samples were machined using a programmed computer numerical control unit at the University of Manitoba. An Instron tensile machine was used to perform tensile test along the gauge length, indicated by arrows in Figure 13. An extensometer was attached to the center of the gauge length to accurately measure the applied strain. It was taken into consideration that the strain applied is evenly distributed through the gauge length of the sample; therefore samples analysed were taken from the gauge length (G) cross section from the straining direction.

3.3 Stress and Strain under Axial Loading

Whether the material will break under the given loading depends on the material itself, and the ability to withstand the intensity of the distributed internal forces (P) through a cross sectional area (A) [59] , known as the stress on that section.

$$\sigma = P / A \tag{5}$$

Stress was denoted by the Greek letter σ (sigma), expressed as force per unit area. The sign convention to indicate tensile stress is positive (+), a negative sign (-) to indicate compressive stresses.

The normal strain (ε) in a material under axial loading is the deformation (δ) per unit length (L) of that specimen.

$$\varepsilon = \delta / L \tag{6}$$

3.3.1 Engineering Stress-Strain Curve

Plotting the stress verses the strain as loading continuous to apply to the specimen would yield a stress-strain diagram that can determine some strength parameters and the ductility of the material.

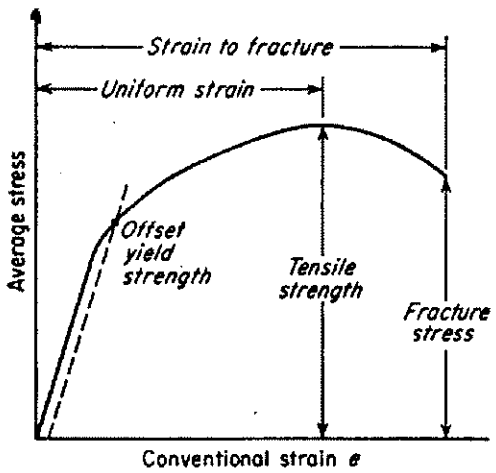

Figure 14: Engineering stress-strain curves [59]

Figure 14 is a typical engineering stress-strain curve for a ductile material. Stress – strain curves are unique for each material, and it is found by recording the amount of deformation (strain) at distinct intervals of tensile loading.

The 0.2% offset yield strength σ_y (ASTM E8) [58] is the point after which any continued stress results in permanent, or inelastic (plastic) deformation. Plastic deformation is permanent (irreversible); material is permanently deformed even when the load is released to zero. The stress to produce continued plastic deformation increases with increasing plastic strain, or the metal strain-hardens, as in the case of cold working. As the specimen elongates, its width and thickness decrease uniformly along the gauge length in cross-sectional area. This is the region where the percentage deformation is measured. A material is considered to have completely failed once the fracture stress was reached.

3.4 Tension Test

Tension tests were performed using an Instron Tensile machine. A software called "stress – t" was used to control the tensile machine, written by Don Mardis, a technician from the Metallurgical Science Laboratory at the University of Manitoba. Samples were tensile strained at room temperature and the yield stress was taken as the 0.2% offset yield strength. Data acquisition controlled valuables are listed below:

Tensile strain properties

Sample speed:	2 samples/sec.
Strain options:	Extensometer
Sample type:	Plate
Strain rate:	$5X10^{-4}$mm/sec.
Strain increment:	0.005mm/mm
Cross – head speed:	5mm/min.
Full scale strain:	10 volts
Full scale load:	3000kg

All processed samples were observed in an optical microscope after polishing and etching using standard metallographic techniques. The etchant was a solution containing 50% nitric acid and 50% acetic acid.

3.5 Hardness Measurements

Vickers Hardness tester with 10kg load was used to measure the hardness of each sample. Tests were performed following the Standard test method for Vickers Hardness of Metallic Materials E92 [60]. An indentation hardness test using a calibrated machine to force a square based pyramidal diamond indenter having a face angle of 136°, into the surface of the material under test and to measure the diagonal of the resulting impression removal of force. Vickers Hardness number (VH) relates to the applied force and the surface area of the permanent impressive, in terms of kgf/mm^2. Five to eight measurements were taken per sample and hardness curves were plotted using the average value measured.

3.6 Thermo-mechanical Processing

A wide selection of physical parameters, such as the annealing temperature, degree of pre-strain, time of anneal, grain size, and the atmosphere of heat-treatments can influence the results from a strain annealing experiment. A limitation on the number of experimental variables is considered judicious.

3.6.1 Short Annealing Time Experiments

Experiments were designed using a 2^3 factorial matrix, to determine the effects of different combinations of pre-strain (low and high) and temperature (low and high) on

grain boundaries, while holding the time of anneal constant for 10 minutes. An example of the 2^3 factorial matrixes is demonstrated in the Table 12:

Table 12: Example of 2^3 factorial matrixes

Strain (%)	Temperature (°C)	Total Strain (%)
Low	Low	Low
High	Low	Low
Low	High	Low
High	High	Low
Low	Low	High
High	Low	High
Low	High	High
High	High	High

The three processing parameters to control and manipulate for the design matrix are:

Strain: 3%, 6%, 9%, 12% (tensile strain)

Temperature: 500°C, 600°C, 700°C, 800°C, 900°C, 1000°C

Time: 10 minutes

Heat-treatments were performed in an inert atmosphere (argon gas) to avoid precipitation of the oxygen that may affect the recovery mechanism, followed by air cooling to room temperature. In the early stages of experimentations, the time of anneal were held constant while manipulating the strain and temperature valuables only, to observe changes in special boundaries. Single step and sequential multiple steps strain – anneal treatments were performed following the 2^3 factorial matrix procedure by selecting

different combinations of strain levels and temperatures, while holding the time of anneal constant.

3.6.2 Time Extended Experiments

Extending the time of anneal beyond 10 minutes were processed to observe changes in GBCD compared to short annealing time processes. This was done by using a low pre-strain of 3% and 6%, annealed at temperatures of 700°C and 800°C. Table 13 outlines the format of the time extended experiment.

Table 13: Time extended experimentations

Strain + anneal	Time				
3% at 700°C	0.167hour	48 hours	72 hours	96 hours	168 hours
6% at 700°C	0.167hour	48 hours	72 hours	96 hours	168 hours
3% at 800°C	0.167 hour	42 hours	84 hours	126 hours	168 hours
6% at 800°C	0.167 hour	42 hours	84 hours	126 hours	168 hours

Samples annealed at 0.167 hours or 10 minutes are considered as the starting point of the long time anneals experiment. The maximum annealing time used was 168 hours, based on some of Randle's experiments [19] where extensive coherent $\Sigma 3$ twin boundaries were found for a long annealing period. Intermediate times were recorded and analysed between 0.167 hours to 168 hours, to observe the transition change between annealing.

3.7 Scanning Electron Microscopy (SEM)

Electron microscopy is often used to study microstructural as well as morphological features of engineered materials. Scanning Electron Microscope (SEM) uses a stream of electrons generated by thermionic emission, accelerated toward the specimen inside of a vacuum.

Samples were observed in JEOL, JSM-5900LV scanning electron microscope using the secondary electron image and back-scattered electron image. Difference in crystal orientation can be obtained by utilizing the backscattered electron mode, which is a function of Bragg's Law.

The diagram shown in Figure 15 is a typical Scanning Electron Microscope with its components labeled:

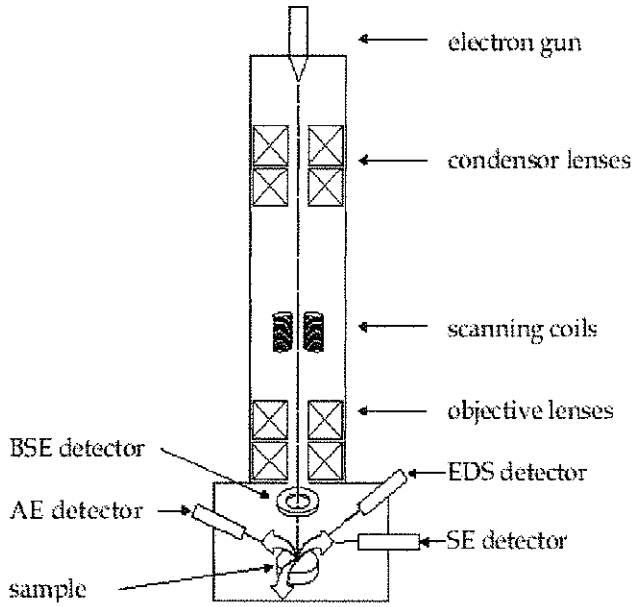

Figure 15: Schematic representation of the Scanning Electron Microscope [18]

A stream of electrons is confined and focused using metal condensor lenses into a thin, focused beam which impinges onto the sample using objective lenses. A variety of signals could be sensed using the detectors shown in Figure 15.

3.8 Analyses Techniques (EBSD Pattern Formation)

Electron back-scattered diffraction (EBSD) has become a recognized technique for studying microstructure since 1970's [61]. This technique relies on positioning the sample within the SEM chamber such that a small angle, typically 20°, made between the incident electron beam and the specimen surface [62]. The purpose of the tilt angle is to reduce the path length of electrons, enhance the fraction of backscattered electrons to experience diffraction by lattice planes in the sampled volume [63]. As electron beam enters the sample, it would diffuse and scattered in all directions. Some electrons would diffract at the Bragg angle θ_B at every set of lattice planes [62]. Bragg's Law is defined as:

$$\lambda\, n = 2d^{*}\sin\theta_B \tag{7}$$

Where n is the order of reflection and it is equal to 1 for EBSD [62]. λ is the electron wavelength, d is the lattice spacing and θ_B is the angle between incident x-rays and the diffracted beam, which was found to be about 0.5° [62].

As diffraction occurs in all directions, the locus of the diffracted radiation, [62] is the surface of a cone, extending about the normal of the reflecting planes having a half apex angle 90 - θ_B°. When the source of electron scattering was considered between lattice planes, two cones would radiate from each side of the planes. With a small Bragg angle, diffracting cones are nearly flat, at 180° [62]. The resulting electron diffraction pattern (EBSP) or the Kikuchi pattern, can be imaged by a fluorescent screen located inside the specimen chamber.

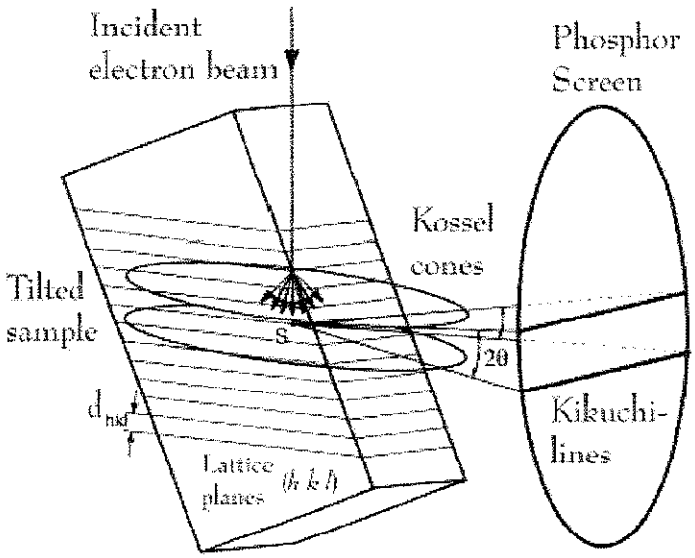

Figure 16: Inelastic Scattered electrons from specimen generating Kikuchi-lines on fluorescent screen [62]

EBSD Kikuchi pattern consists of pairs of parallel lines that correspond to a distinct crystallographic plane, each pairs of lines are known as a Kikuchi band. The intersection of bands corresponds to a zone axis (pole). The Kikuchi patterns essentially embody all the angular relationships in a crystal, both the interzonal (angle between each strong band) and interplanar angles, and therefore implicitly contain the crystal symmetry

[61]. This would permit a direct imaging of the specimen almost at the same time as the diffraction pattern is taken [64], despite the highly inclined specimen geometry with respect to the electron beam.

The interaction of these Kikuchi diffraction patterns defines the characteristic grain boundary. Adjoining grains with a high degree of lattice matching from the crystal orientation, which can be signified by a low coincident site lattice (CSL) number ($\Sigma \leq 29$ normally considers as low CSL) using the EBSD system.

3.9 Orientation Imaging Microscopy (OIM)

A technique that monitors both the microstructural and orientation information is essential. Electron Backscatter Diffraction (EBSD) system is the technique now used in correlation with software incorporating fully automated procedures for recognizing and indexing diffraction patterns [65]. This reconstruction technique is known as the Orientation Imaging Microscopy (OIM) set up by Dingley and Adams by TSL in Salt Lake City, Utah.

To accurately obtain the orientation from the indexing of a diffraction pattern during scanning, three calibration constants x, y, *l* are necessary to derive. Coordinates x and y indicates the sample position with respect to the electron beam, as shown in Figure 17; which arises from the intersection of a vector originating at the intersection of the

electrons with the sample normal to the electron beam, called the 'Pattern Center' (PC) [61]. Pattern Center is altered as the beam changes its position on the sample surface; the optimize position for a perfect calibration is to set PC 2/3 of the way up from the bottom of the screen [65]. Another important valuable *I* is the normal distance from the intersection of the electron beam with the sample to the phosphor screen. Normal distance *I* between 350 and 500 for a working distance of 12mm would provide good spacing between sample and the camera.

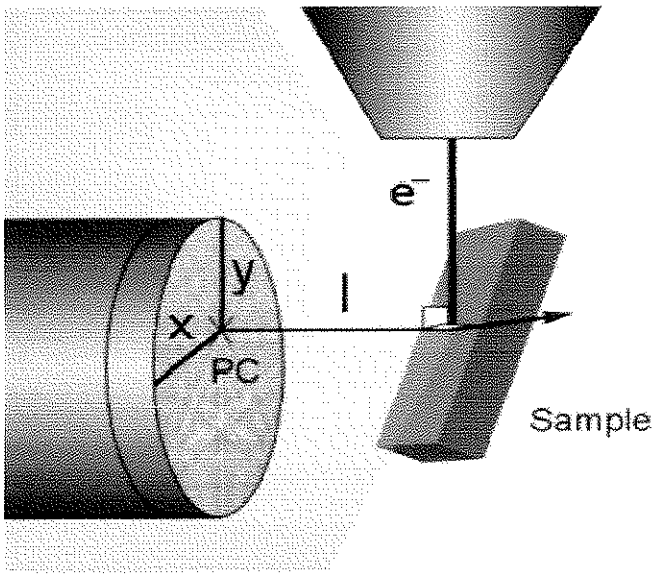

Figure 17: Schematic of the EBSD geometry including calibration parameters [66]

One of the most important components of the OIM system is the camera, which obtains diffraction images [65] from the sample. The capability of the camera system in obtaining images with low brightness in a short time will dictate the SEM operating conditions required. The camera control unit (CCU) receives the signal from the camera and provides a television output video signal. The CCU generally has controls for

electronically altering the intensity gradient across the detector, in which the raw image is as smooth as possible. Gain control and black level are also typically included for user manipulation of the raw images. The output signal is sent to an image-processing unit which enhances the signal and corrects for any intensity gradients across the phosphor screen. This is done by first collecting a signal from a large volume of the material being analyzed.

The EBSP collected from the large area (background) is stored in a buffer. Each time an EBSP is captured, this buffer is automatically subtracted from the EBSP, which result an enhanced contrast level. The processed signal simultaneously with the EDS data is sent to the computer for analysis. The formation, capturing and subsequent indexing of the Kikuchi patterns are the basic mechanisms which are necessary for electron backscatter diffraction.

Although it has been acknowledged that EBSD is an important use for determination of crystallographic textures, there are still a number of inherent problems with the system [67]. These problems include the ability to index deformed microstructures and the difficulties of analyzing patterns in the region of grain boundaries [67].

3.9.1 Orientation and Misorientation

A coordinate system with a reference frame consisting of at least two axes is essential to specify an orientation of a specimen. The important surfaces and directions to define the axes are surface normal (SN), rolling direction (RD) and transverse direction (TD). Directions and axes in the crystal specify the crystal coordinate system; the axes [100], [010] and [001] as shown in Figure 18 could be recognized and calibrated through OIM.

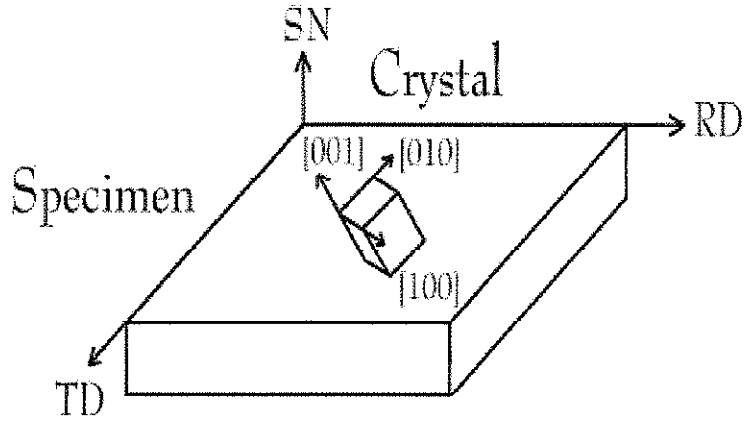

Figure 18: Coordinate systems of specimen and cubic symmetric crystal [18]

3.9.2 EBSP Image Processing

The first step in automated indexing of electron backscatter patterns (EBSP) or Kikuchi patterns is to extract the bands from the pattern. Using the Hough transform

(Radon transform) 1962, to extract band information is the most commonly method employed today [68]. The equation governing the Hough transform is:

$$\rho = x \cos \theta + y \sin \theta \tag{8}$$

Where (x , y) describe a set of pixel coordinates forming a line, ρ is the perpendicular distance from the origin and θ is the angle with the normal; where the Hough parameters (ρ, θ) provide a wave like function in Hough space. An alternate description of Hough parameters (ρ, θ) are shown schematically in Figure 19.

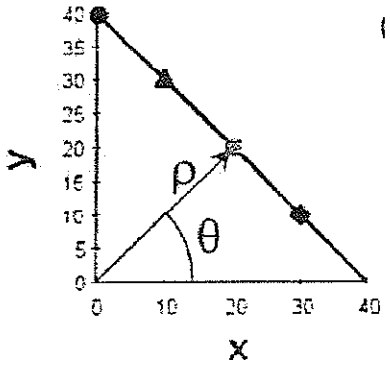

Figure 19: Schematic of Hough transform parameters in x-y space [69]

The purpose of the Hough transform is to convert the parallel lines found in EBSD patterns to become single points in the Hough space [69]. These converted points are easy to identify and be used in automatic computation. A Kikuchi band can be found by adding the intensity of each (x , y) pixel and find the peak of relatively high intensity in the Hough transform.

3.9.3 Automated Indexing

Once the Kikuchi bands have been detected, the reflecting planes associated with the detected bands can be identified. Band characteristics can be used for indexing the width of a band (d-spacing through Bragg's law) and the angle between the located bands (compared to interplanar angles). For a given diffraction pattern, several orientations may be found which satisfy the diffraction bands detected by the image analysis route. The reliability of the indexing bands depends on several parameters: the confidence index (CI), the image quality (IQ), and the fit between the recalculated and the detected bands.

3.9.4 Confidence index (CI)

Confidence index is given by

$$CI = \frac{(V_1 - V_2)}{V_{total}} \tag{9}$$

where V_1 and V_2 are the two highest numbers of votes (possible indexing solutions within the tolerance angle from the orientation) and V_{total} represents the total possible number of votes from the detected bands. CI value yields between 0 and 1, and in general, CI values greater than 0.4 or 0.5 represents a proper indexing pattern [65].

3.9.5 Image Quality (I.Q.)

The image quality reviews the relative quality of the electron backscatter diffraction pattern using the intensities of the found Hough peaks. I.Q. is a function of the technique and parameters used to index the pattern, and it is dependent on the material and the video processing (changing the contrast and brightness affects the I.Q. values). Properly polished and calibrated samples would yield an I.Q. value >200. In the vicinity of a grain boundary or precipitate, the I.Q. would drop dramatically as the system may view two diffraction patterns with the change in orientation on going from grain to grain [62].

3.9.6 Fit Parameter

The fit parameter defines the average angular deviation between the recalculated and the detected bands, or how well the system is calibrated with the crystal structure parameters defined. This gives an indication of the reliability of the pattern during indexing. Low fit value, such as <1 means a good fit.

3.10 OIM Data Collection

Orientation Image Microscopy (OIM) has largely superseded other experimental techniques, such as Transmission Electron Microscopy (TEM) and Electron Channelling in the SEM. This is due to the straightforward specimen preparation and the large number

of orientation measurements attainable in a relatively short period of time. A picture inside of the SEM chamber is shown in Figure 20:

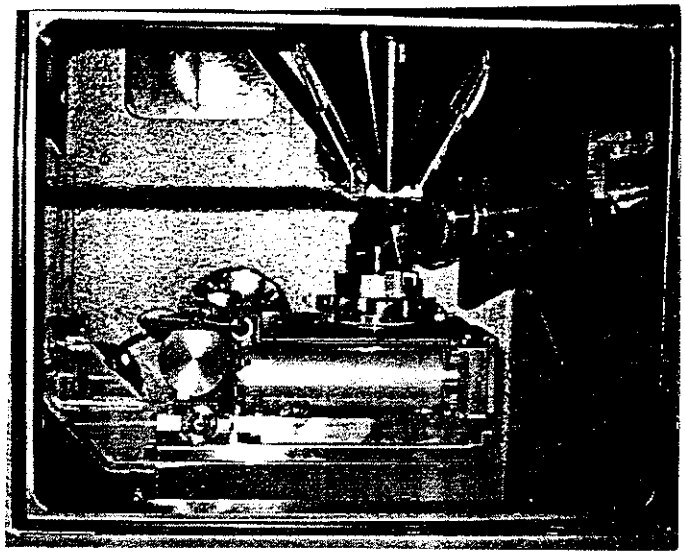

Figure 20: Picture inside of SEM chamber

Samples were observed in SEM with an integrated OIM attachment supplied by TSL, Inc. (Draper, UT) automatically acquires and processes EBSPs for the determination of local orientations, misorientations, and microtextures.

The software used to collect orientation data points was OIM data collection version 3.5 by TSL, Inc. It allows the orientation at spatially specific points in planar sections of the microstructure to be measured. Individual orientation measurements were made at discrete points on a sample by a hexagonal cell, located in a rectangular grid of dimensions prescribed with a certain width and height, depending on the step sizes of 1-8μm over an area of $4X10^3 - 5X10^6 \mu m^2$ in dimension.

At each point in the grid, the backscattered Kikuchi diffraction patterns are captured, frame averaged and automatically indexed. The image quality, confidence in

indexing the EBSP and the three Euler angles that describe the orientation are recorded along with coordinates describing the position. Therefore, images can be generated by mapping the crystal orientation onto a colour or greyscale and shade each point on the grid according to the crystal orientation.

The orientation data were further analysed using OIM data analysis version 3.5 by TSL, Inc. There are also situations where OIM has difficulties identifying some orientations, such as at grain boundaries where patterns often are made up of two superposed diffraction patterns from both crystal lattices. Incorrect solution near grain boundaries or triple points may result as bands were detected from both of the superposed patterns.

The CSL model was used to characterize the grain boundaries. Low-Σ boundaries were colour coded as follows,

$\Sigma 3$ = Green,

$\Sigma 9$ = Orange,

$\Sigma 27a,b$ = yellow,

Other $\Sigma \leq 29$ and $\Sigma \neq 1$ = Red,

Random = Black.

An average of 300 grains was examined per specimen.

3.10.1 OIM Data Clean-Up

OIM provides several clean up methods that clean up individual data points based on the neighbouring orientation. The steps used to clean up datasets are:

1) Grain CI standardization,
2) Neighbour Orientation Correlation,
3) Grain Dilation.

This sequence of steps for the clean up routine was suggested by TSL. The importance of the clean up routine is to treat points with a low confidence index (< 0.1). The certainty in indexing of EBSP is nearly constant at ~95% for confidence indices greater the 0.1, whereas the certainty decreases sharply when confidence indices is less than 0.1 [61].

The function of Grain CI Standardization changes the CI's of all points in a grain to the maximum CI found among all points belonging to the grain. Neighbour Orientation Correlation is a check to determine if the orientation of each data point is different from its neighbours with a grain tolerance angle. A grain tolerance angle of 5° was used to signify that only one nearest neighbour must be different, along with the minimum grain size set at 2μm and a minimum confidence index of 0.1. The last step is the Grain Dilation method. This is an iterative routine that only acts on points that do not belong to any neighbouring grains. If the majority of neighbours of a particular point belong to the same grain, then the orientation of the particular point is changed to match that of the majority grain. This process is repeated until each point in the data set becomes a member of a grain. Thereafter, colour-coded boundaries can be assigned with respect to their type of boundary, random or special. Boundaries with $\Sigma \leq 29$ are considered to be special, while boundaries with $\Sigma > 29$ are random high angle boundaries.

Chapter 4

RESULTS AND DISCUSSION

4.1 Mechanical Properties of Ni-200

Mechanical properties of the as – received commercially pure nickel or Ni-200 (99.5% pure) are listed in Table 14:

Table 14: Mechanical Properties of Ni-200

Yield Strength (0.2% Offset)	290 MPa
Ultimate Tensile Strength	502 MPa
Fracture Strength	411 MPa
Uniform Elongation	47.8 %
Maximum Strain	64.0 %

Values were recorded as the specimen tensile strained until fractured at room temperature. An engineering stress strain curve was also generated for the same sample strained until fractured, shown in Figure 21.

4.1.1 Stress – Strain Curve

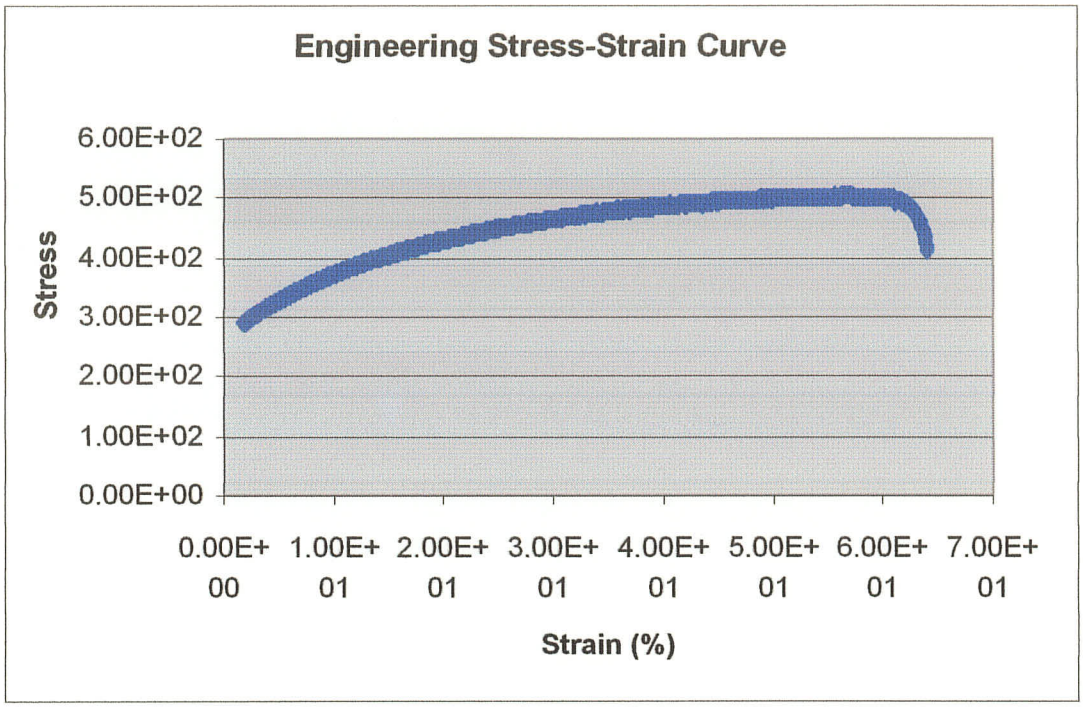

Figure 21: Engineering stress-strain curve

The elastic region of Figure 21 was eliminated, as only the plastic deformation was of interested in this experiment. It can be observed that Nickel is considered relatively ductile; a maximum uniform elongation of 47.8%, enabling sufficient uniform strain to be available for the strain values used in the project (3-12% strain).

4.2 Microstructure of As-Received Material

The as-received commercially pure nickel (Ni-200) is shown in Figure 22.

(a)

(b)

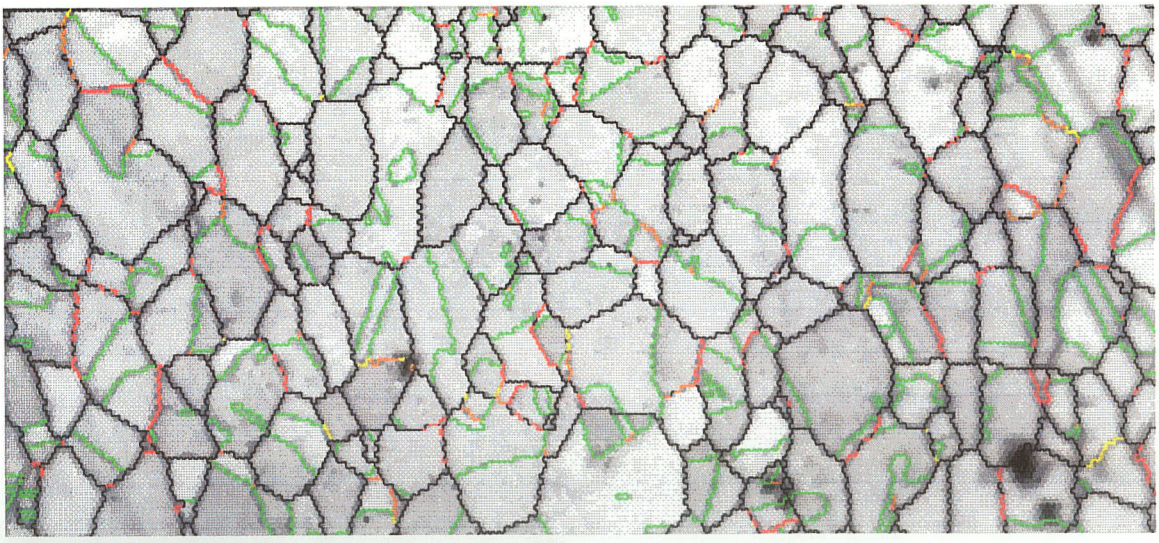

(c)

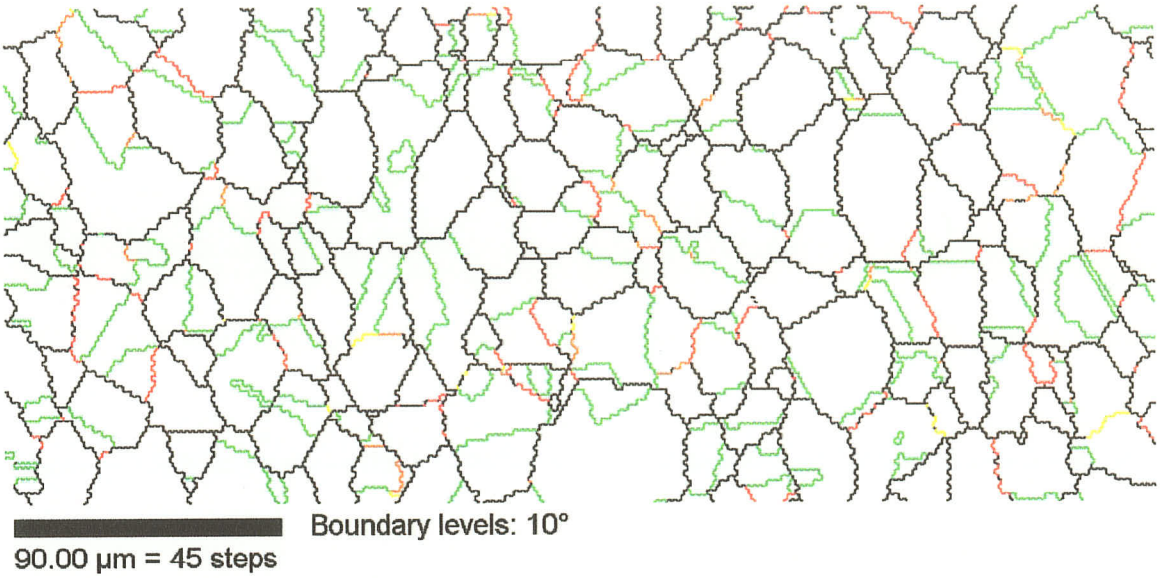

Figure 22: As – received Ni-200 observed in (a) Optical microscope magnification 200X, (b) Grey scale shaded OIM image with colour coded CSL boundaries, $3 \leq \sum \leq 29$, (c) Non-grey scale shaded OIM maps with colour coded CSL boundaries

The optical micrograph (Fig.22a) reveals uniformly distributed austenitic equiaxed grains through out the entire volume. The initial grain size is 26µm, measured using a manual linear cross-intercept method with over 500 intercepts counted.

Figure 22(b) is an OIM image generated from the as-received material, with grey scale shading for each grain according to EBSD pattern image quality. Figure 22(c) is the same image but without grey scale shading. It can be observed that the non-grey scale shaded OIM image, or Figure 22(c), is a much clear image to distinguish colour coded boundaries compared to a grey scale shaded image, Figure 22(b). Therefore, it is convenient from here on to use coloured images such as Figure 22(c) when describing OIM maps.

Thin black lines are boundaries representing random high angle boundaries, and the other coloured lines (green, orange, yellow and red) represent low-Σ boundaries, as described in the experimental procedure section. A list of tolerance angles and fractions of CSL boundaries ($3 \leq \Sigma \leq 29$) are shown in Table 15.

Table 15: List of tolerance values and fractions of Sigma boundaries of as-received sample with $3 \leq \Sigma \leq 29$

Sigma (Σ)	Tolerance (^{o})	Fraction
3	8.66	0.269
9	5	0.02
27a	2.89	0.005
27b	2.89	0.005
5	6.71	0.011
7	5.67	0.005
11	4.52	0.014
13a	4.16	0.001
13b	4.16	0.005
15	3.87	0.004
17a	3.64	0
17b	3.64	0.006
19a	3.44	0.002
19b	3.44	0.004
21a	3.27	0.002
21b	3.27	0.002
23	3.13	0.006
25a	3	0.001
25b	3	0.003
29a	2.79	0
29b	2.79	0.001
Total		0.365

The tolerance value indicated for each sigma boundary was obtained automatically by the analysis program using the "Brandon Criterion" in section 2.2.2, which represents the maximum deviation permitted for that sigma boundary. It can be observed in Figure 22(b),(c) and the values in Table 15 that $\Sigma 3$ boundaries (green boundaries) have the highest occurrence for low-Σ boundaries, when $3 \leq \Sigma \leq 29$ was

considered. For the as-received material, the fraction of $\Sigma 3$ boundaries recorded was 26.9% out of 36.5% total special boundaries. This indicates that $\Sigma 3$ boundaries are essential to the development of special grain boundaries. It should be noticed that grain boundaries are in contact 3-dimensionally with many other grain boundaries in addition to those viewed in a single 2-dimensional section; therefore results developed are applied to the system as a whole, rather than to individual boundaries as observed in each mapping.

The total frequency of special grain boundaries does not include contributions from low-angle (Σ 1) grain boundaries, due to ambiguities in distinguishing interfaces from substructures presented in the as-received materials. Hence, the total frequency of special boundaries reported is likely skewed toward lower values than are actually present. This is a function of the TSL software used

4.3 Effects of Deformation on GBCD

Plastically strained samples were analysed using OIM to observe and detect the effects of cold work in the microstructure with respect to the distribution of special grain boundaries.

4.3.1 OIM Observations of Low Strained Samples

Figure 23 shows the cross section of specimens deformed by 3% and 12% strain at room temperature.

(a)

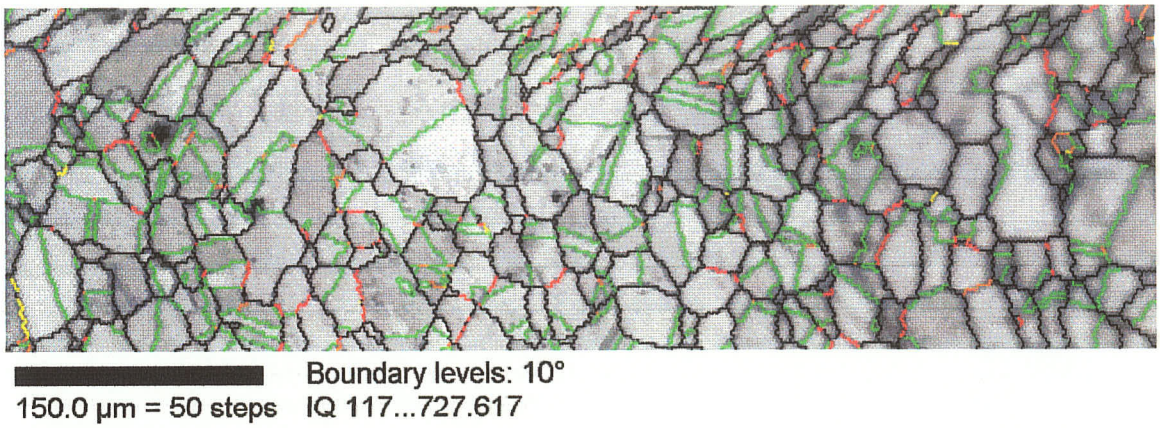

(b)

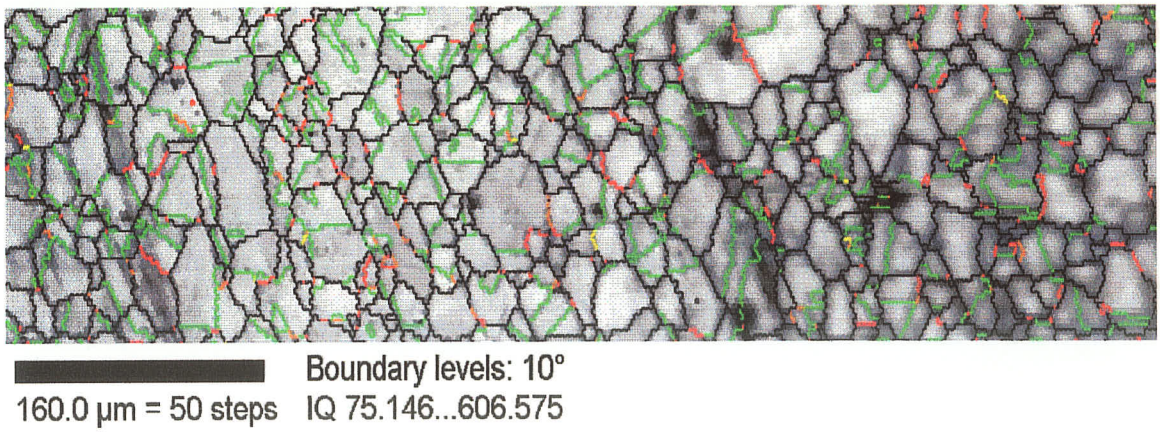

Figure 23: Processed OIM maps of samples strained at room temperature without Heat-treatment: a) 3% strain and b) 12% strain

Changes in microstructures from Figure 23(a) to 23(b) were dependent on the degree of cold work. During sample calibration and data collection, it was observed that

pattern from the unstrained material was characterized by sharp Kikuchi line pairs, whereas the deformed materials were more diffused. The quality of diffraction patterns captured became more blurred as the level of deformation increased.

It is possible to distinguish visually where deformation exists, as the microstructures showed elongated grains, with thick dark deformation bands aligned along the rolling direction (vertical bands). Grains became smaller and more elongated as the amount of deformation increased. Close observation reveals that deformation bands first form at the sides of the samples and then propagate through the volume of the sample. This is in agreement with analyses made by Basson and Driver [70] as the width of the sample decreased.

4.3.2 OIM analyses of low strained samples

The fraction of special boundaries recorded for these samples are summarized in Table 16.

Table 16: Fraction of Σ_{sp} for Samples Deformed at Room Temperature

Deformation at Room Temperature	Σ_{sp} % ($3 \leq \Sigma \leq 29$)
3% strain	38.0
6% strain	31.9
9% strain	29.8
12% strain	25.6

It was found that an applied strain of 3% does not have much effect the overall Σ_{sp} population when compared to the as-received sample, Σ_{sp} = 36.5%. As the applied strain increased to 12%, a decreased in Σ_{sp} was observed, as shown in Table 16. This was caused by a high degree of defects inserted in the microstructure during deformation, increasing the number of higher misorientated angle boundaries, leading to decreased special boundaries.

It has been observed in the literature [19, 22, 36, 43] that the formation of these deformation induced boundary structures provides the driving force to alter the grain boundary characteristics upon heat-treatment. Grain boundary energy minimization processes, such as recovery, recrystallization and grain growth could change the GBCD during heat-treatment. The effects of heat-treatment alone to GBCD of commercially pure nickel (without deformation) have been studied by Randle, in [25]; therefore, annealing on the sample alone will not be analysed in this project. It should be noted that the results in [25] showed an increased in twin density as the annealing temperature increased, where grain growth was the driving force behind the energy minimization process. This is in agreement with observations made by Pande et al. [26].

4.4 Hardness Results

Hardness tests were measured using Vickers Hardness, which can provide a coarse measure of the spatial extent of strain fields [63]. The hardness of the as-received sample had a hardness measurement of 116VH. Cold worked samples were tensile

strained with 3%, 6%, 9% and 12% deformation. Individual hardness measurements were measured at each strain level.

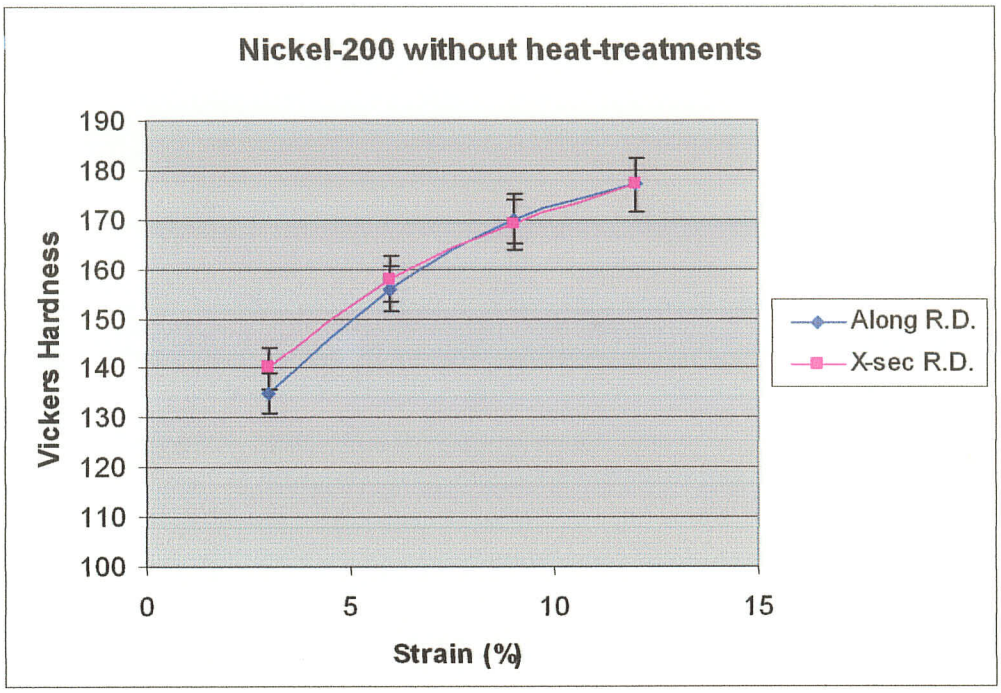

Figure 24: Cold Worked Hardness Curves

Two hardness curves plotted in Figure 24 were obtained by deforming the material along the rolling direction (direction of cold-work) and cross-section from the rolling direction. Averaged hardness values were plotted for each samples with a standard deviation no more than ±5VH. It can be observed the two curves nearly overlapped each other, which indicates the hardness for both directions of cold worked samples are very similar. It is to be assumed that samples taken from either direction cold worked would result in similar material properties. To simplify this project while maintaining a high degree of consistency, cross section from the rolling direction samples were examined.

4.4.1 Strain – annealed Processed Hardness Results

Hardness results of 3%, 6%, 9%, and 12% strain, annealed at 500°C, 600°C, 700°C, 800°C and 900°C for 10 minutes are summarized in Table 17.

Table 17: Strain – annealed hardness results in Vickers Hardness

	500°C	600°C	700°C	800°C	900°C
3% strain	129VH	119 VH	114 VH	99 VH	100 VH
6% strain	146 VH	134 VH	123 VH	92 VH	101 VH
9% strain	158 VH	146 VH	133 VH	99 VH	96 VH
12% strain	170 VH	161 VH	136 VH	95 VH	92 VH

Results from Table 17 are plotted in Figure 25 with percentage strain verses Vickers Hardness.

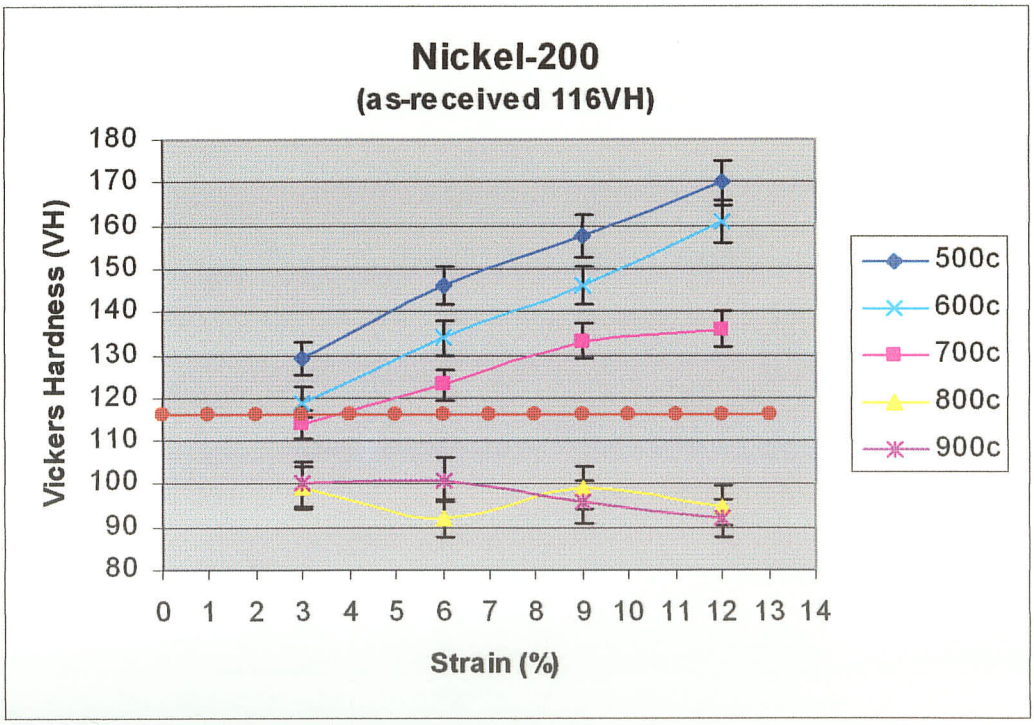

Figure 25: Vickers Hardness verses Percentage strain curves at various temperatures. The horizontal dotted line represents the hardness of the as-received sample

Figure 25 shows the relationship between hardness and single step strain – annealed processed samples with a confidence level (C.L.) of 95% of ± 4.8VH, shown in Equation 10.

$$95\%\ \text{C.L.} = (t*SD)/n^{1/2} \qquad (10)$$

Where SD is the standard deviation of the sample, n is the number of observations, which is equal to 5 and t = 2.132.

Samples strained at 3%, 6%, 9% and 12% annealed at 500°C, 600°C and 700°C showed a near linear increase in hardness as strain increases due to strain hardening effect. At low temperatures, insufficient thermal energy was imparted to the system to allow strain energy to relieve the cold worked state.

Hardness curves for samples annealed at 800°C and 900°C however showed decreased in hardness compared to the as-received sample, which had a hardness of 116VH. A consistent range of 90 to 100 VH was recorded for all strain levels for these two curves. The observed reduction in hardness with increased temperature is evidence of stored energy being expended, causing the material to soften. Increased in grain size was observed for samples annealed at 800°C and 900°C. The grain size of samples strain and annealed at 800°C averaged 57μm and samples processed at 900°C averaged 80μm, compared to samples for 700°C was ~27μm. The influences of this behaviour to the distribution of $\sum_{sp}$ was further analysed using the EBSD technique in the latter sections.

4.5 Thermo-mechanical Processing

It has been shown in the previous section that the applied strain alone does not increase the fraction of special boundaries, with an applied strain up to 12%. As well, it was found in [16] that heat-treatment alone increases the proportion of $\Sigma 3^n$ within a sample volume, not the overall Σ_{sp} distribution. The level of strain and annealing temperature needed to reach a high level of special grain boundaries is unclear from Figure 25. Therefore, one step strain – anneal treatments were processed and analysed.

4.5.1 One Step Strain Anneal Processing Results

A pre-strain of 3% (minimum) and 12% (maximum) were chosen as lower and upper limits of strain to apply to individual samples. The applied deformation is not intended to be sufficient to act as potential nucleation sites for recrystallization, but yet, the recovery mechanism is still operative for grain boundary migration. Annealing temperatures of 500°C and 700°C were chosen to observe the change in GBCD for samples that strain hardened in Figure 25. 800°C was the temperature first observed a drop in hardness in Figure 25, which dictates that energy minimization processes may have occurred for boundary migrations. Resulting fractions of special boundaries are listed in Table 18:

Table 18: Single step special boundaries percentage obtained by 3% and 12% strains and annealed at 500°C, 700°C, 800°C

	500°C Σ_{sp} (%)	700°C Σ_{sp} (%)	800°C Σ_{sp} (%)
3% strain	32.2	25.3	36.6
12% strain	29.6	29.5	33.1

Σ_{sp} represents the total percentage of special boundaries, where $3 \leq \Sigma_{sp} \leq 29$.

Results from Table 18 show that single step processing of 3% and 12% strain, annealed at these temperatures do not show enhancement in the total fraction of special boundaries, when the Σ_{sp} values remained similar to the as – received sample, at 36.5%. OIM images of these samples are shown in Figure 26 with colour coded to distinguish special boundaries from random boundaries.

(a)

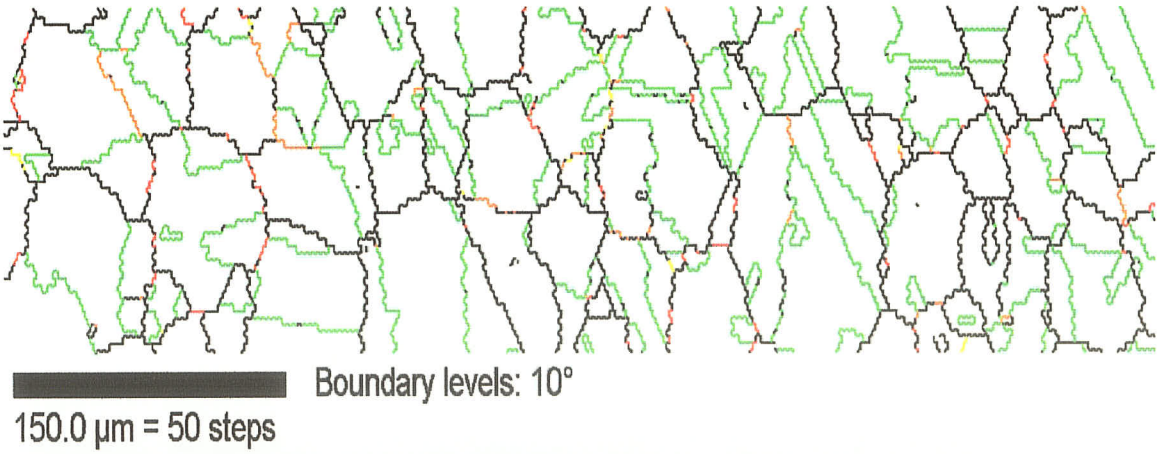

(b)

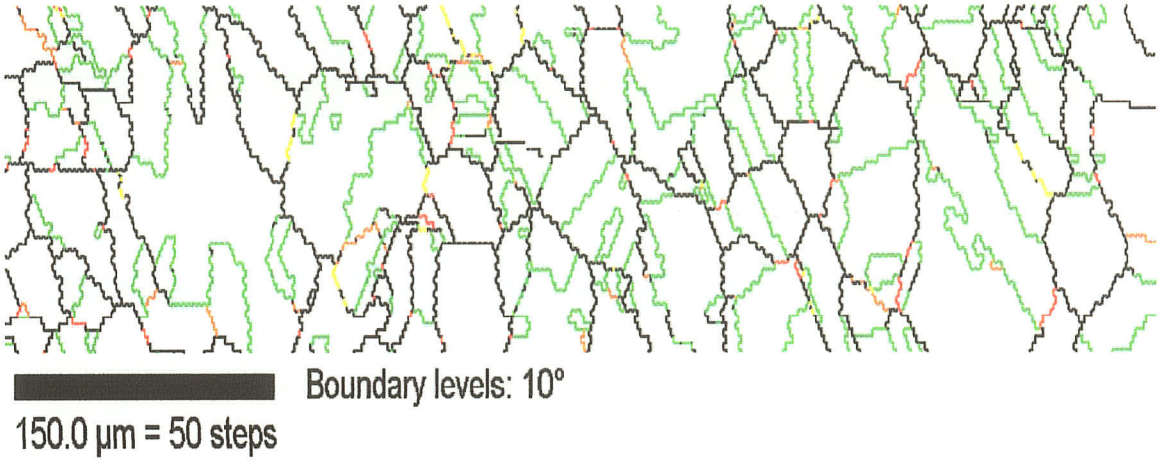
Boundary levels: 10°
150.0 µm = 50 steps

(c)

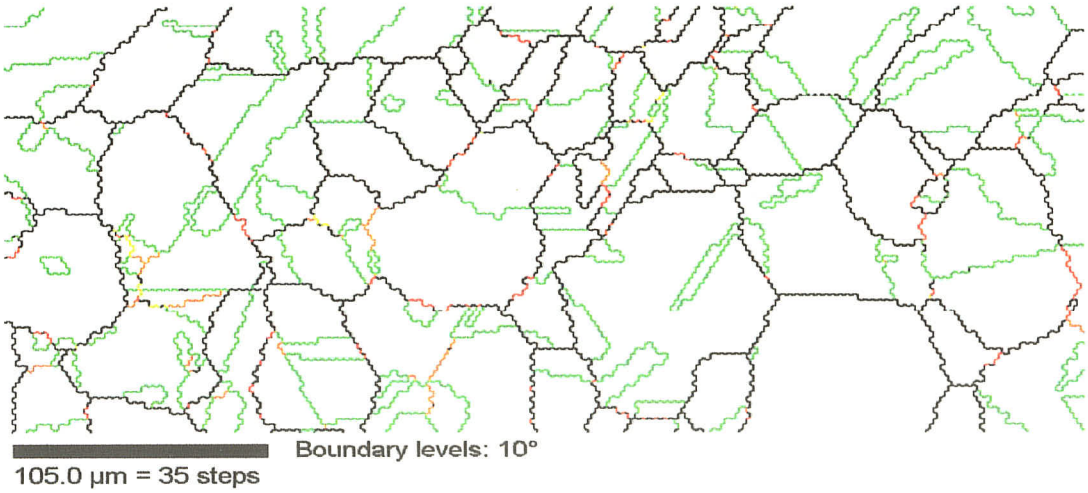
Boundary levels: 10°
105.0 µm = 35 steps

(d)

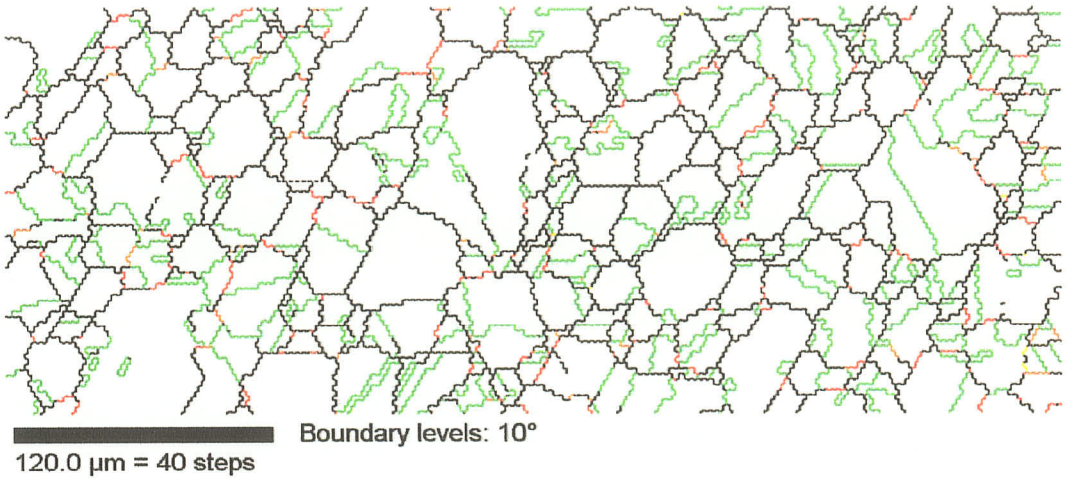

(e)

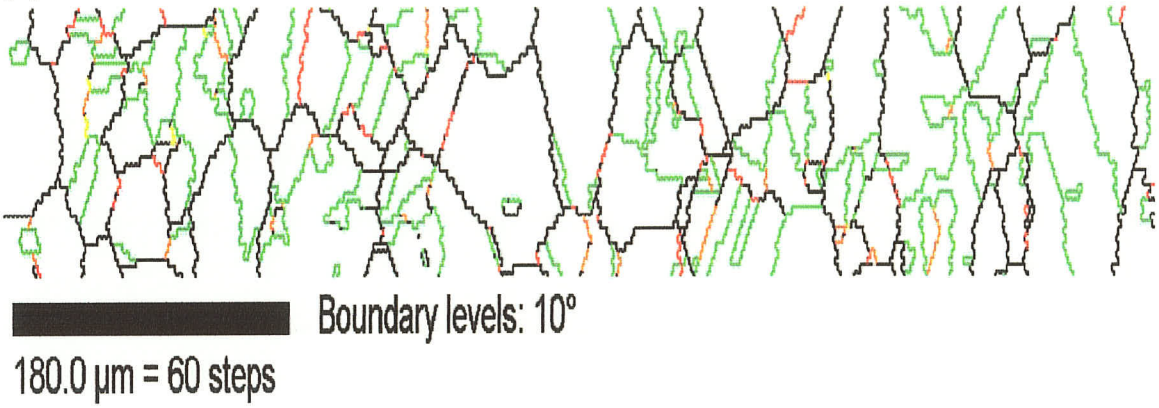

(f)

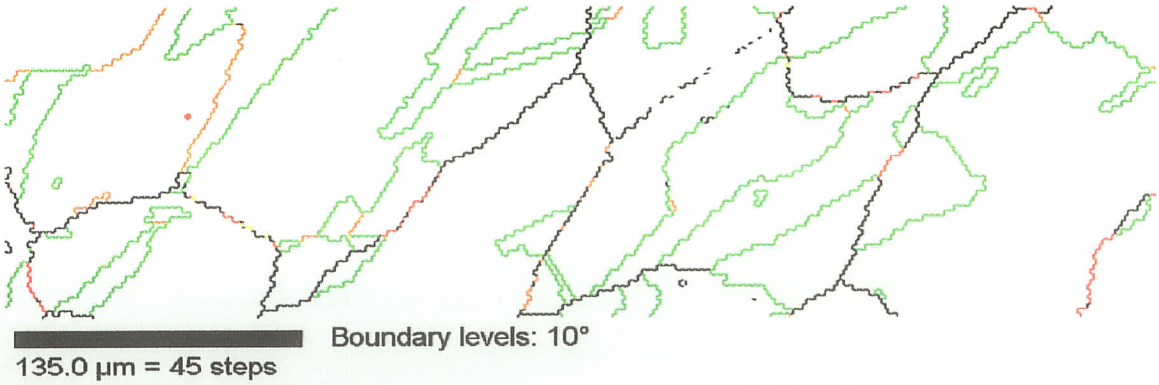

Figure 26: OIM maps of (a) 3% strain annealed at 500°C, (b) 12% strain annealed at 500°C, (c) 3% strain annealed at 700°C, (d) 12% strain annealed at 700°C, (e) 3% strain annealed at 800°C and (f) 3% strain annealed at 800°C.

An annealing time of 10 minutes was chosen because for pure metals, grain growth is expected to occur at high temperatures in a short period of time, owing to the lack of solute inhibition compared to alloys. Grain size measurements of these one-step processing are detailed in Table 19.

Table 19: Grain size measurements of one-step strain anneal treatments

Process	Grain size (μm)
As-received	26
1 step – 3% annealed at 500°C	27
1 step – 12% annealed at 500°C	23
1 step – 3% annealed at 700°C	31
1 step – 12% annealed at 700°C	29
1 step – 3% annealed at 800°C	29
1 step – 12% annealed at 800°C	53

It can be observed from Table 19 that grain growth occurred for the 12% strain sample annealed at 800°C being double the as-received value of 26μm. Meanwhile the grain size for the other samples remained static compared to the as-received material. Sample with 3% strain annealed at 800°C showed minimal increased in grain size at an elevated temperature was possibly due to an insufficient strain energy supplied at grain boundaries to instigate grain growth. At 12% deformation annealed at 800°C, sufficient amount of energy was stored and released for grain coarsening, driven by the reduction in grain boundary area. Special boundaries recorded in Table 18 do not show significant change from the as – received sample. Therefore, these single step strain - anneal

processes has no impact on the distribution of special grain boundaries over the range of temperatures (500°C, 700°C and 800°C) and strain level used (3% - 12%).

4.5.2 Multiple Steps Strain Anneal Treatments

Further analyses were investigated using multiple steps strain – anneal experiments to observe change in special boundaries proportion. The format of the multiple steps strain – anneal treatments is shown in Table 12.

4.5.2.1 Annealed at 500°C and 700°C for 10minutes

Eight samples were developed in this experiment, and the percentage strain and temperatures used are given in Table 20:

Table 20: Values for 2^3 Factorial Multiple Steps Strain – Anneal Treatment

Strain (%)	Temperature (°C)	Total Strain (%)	# of Cycles
3	500	6	2
6	500	6	1
3	700	6	2
6	700	6	1
3	500	12	4
6	500	12	2
3	700	12	4
6	700	12	2

One step and multiple steps strain – anneal processes were involved in this set of experiment. Low strains and the annealing temperatures applied were similar to the one step strain – anneal process performed in the previous section. This enables one to differentiate the effects of one step strain - anneal processing against multiple steps strain - anneal processing on the final fraction of special boundaries. Results of these eight processed samples are represented in a bar graph, plotted as percentage special boundaries in Figure 27.

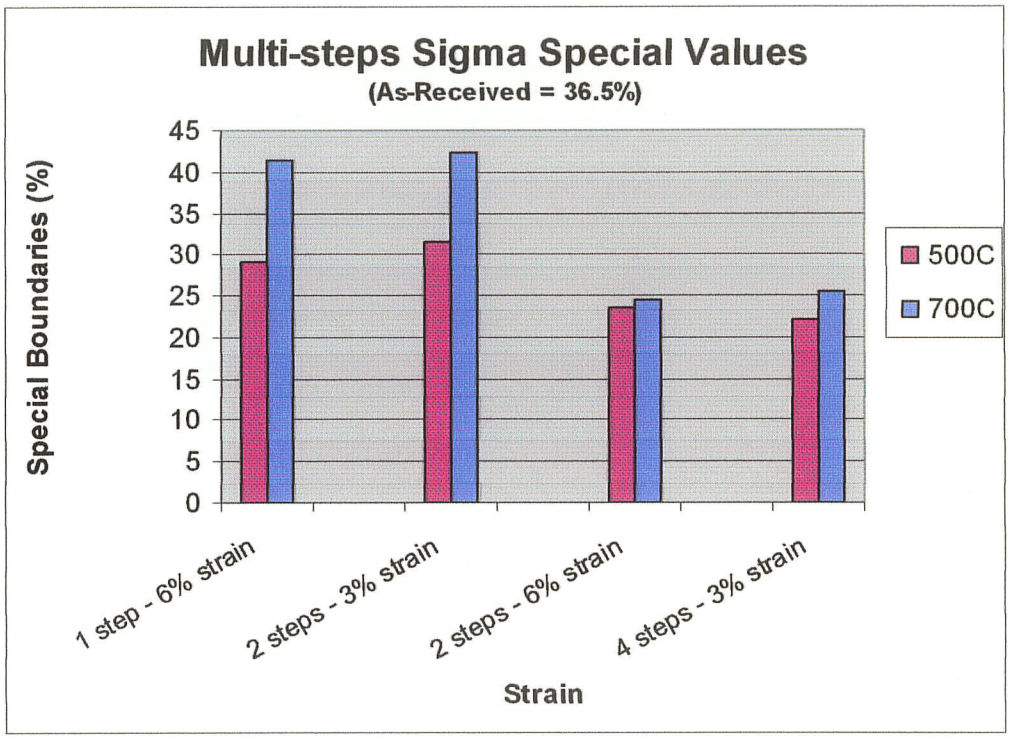

Figure 27: Graphical representation of multiple steps processing results annealed at 500°C and 700°C

Special boundaries fraction of multiple steps processing samples annealed at 500°C and 700°C are indicated in Figure 27. The annealing time for these samples was

again held constant for 10 minutes. Samples processed at 1 step – 6% strain and 2 steps – 3% strain (6% strain total) showed a higher fraction of special boundaries than 2 steps – 6% strain and 4 steps – 3% strain (12% strain total) samples.

Special boundaries values of multiple steps processing are given in Table 21.

Table 21: Result Values of Multiple Steps Processing Annealed at 500°C and 700°C

	500°C Σ_{sp} (%)	700°C Σ_{sp} (%)
1 step - 6% strain = 6% strain	29.2	41.5
2 step - 3% strain = 6% strain	31.5	42.3
2 step - 6% strain = 12% strain	23.6	24.5
4 step - 3% strain = 12% strain	22.1	25.6

The Σ_{sp} values for samples strain and annealed at 500°C showed a negative improvement of special boundary fractions, with $\Sigma_{sp} \leq 31.5\%$. Samples with a strain of 12% annealed at both 500°C and 700°C showed a greater drop in special boundaries compared to the as-received sample at 36.5%.

At lower pre-strain (total of 6% strain), samples processed at 1 step and 6% strain and 2 steps of 3% strain annealed at 700°C showed an increased in special boundary percentages, with $\Sigma_{sp} \sim 42\%$. Possible grain boundary recovery occurred for some rotation of grain boundary plane when grain growth was not observed for all the samples processed at 700°C. The grain size measured for these samples is between 24-30μm. Results shows that a low strain of 6%, annealed at 700°C for 10 minutes could increase

the total special grain boundaries, regardless of single step or multiple steps. OIM maps of samples with 6% (absolute) strain annealed at 700°C are shown in Figure 28.

(a)

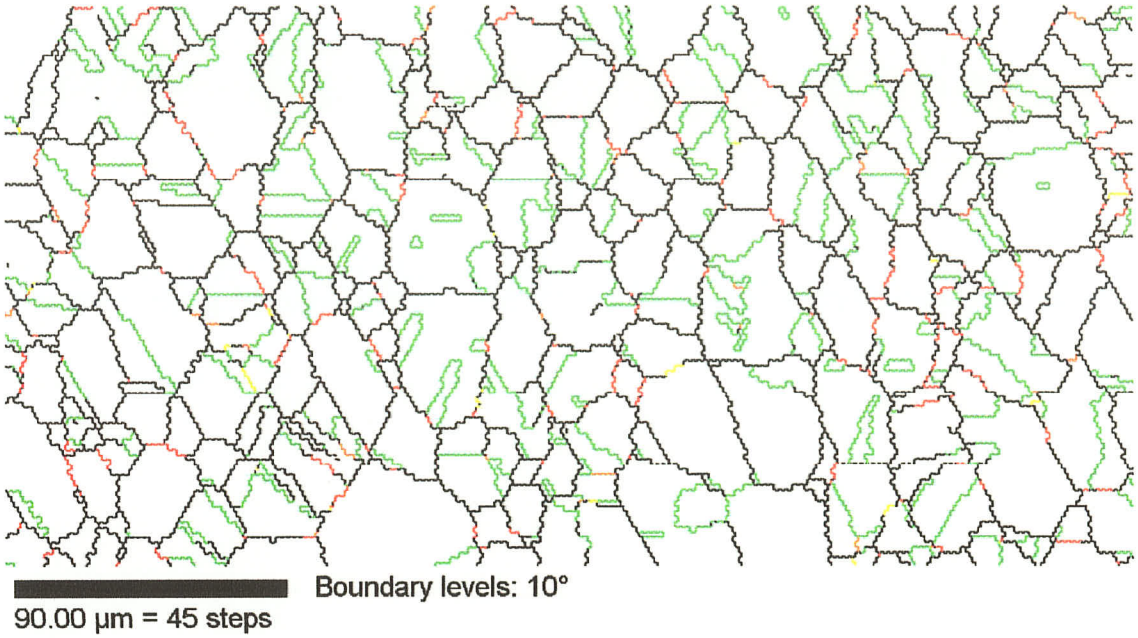

(b)

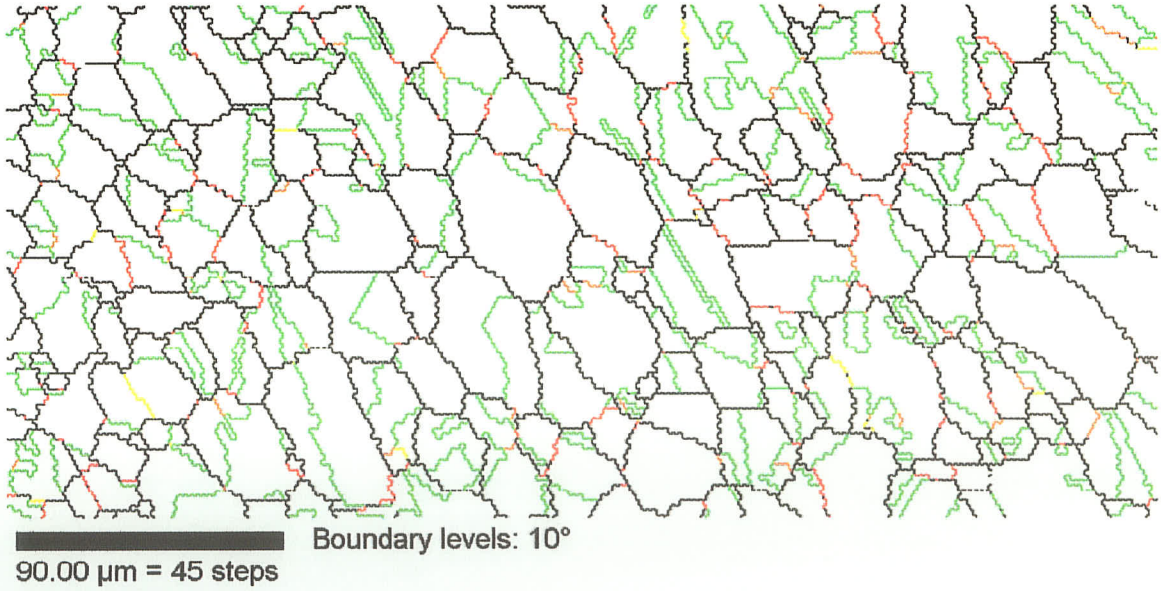

Figure 28: OIM maps of processed samples (a) 1 step – 6% strain, (b) 2 steps – 3% strain annealed at 700°C

4.5.2.2 Annealed at 800°C for 10minutes

The multiple steps strain – anneal experiment in the previous section was the foundation for modifications the varying processing parameters to increase the fraction of special boundaries. According to the Vickers Hardness results in Figure 25 and the grain size measurements in Table 19, the temperature where grain growth begins is 800°C. An experiment was conducted to determine what the effects of increasing the annealing temperature up to 800°C have on the GBCD. To be consistent with previous experiments, only the annealing temperature was changed to 800°C, while the sequence of strain and the time of anneal remained the same. The combined results are shown in the Figure 29:

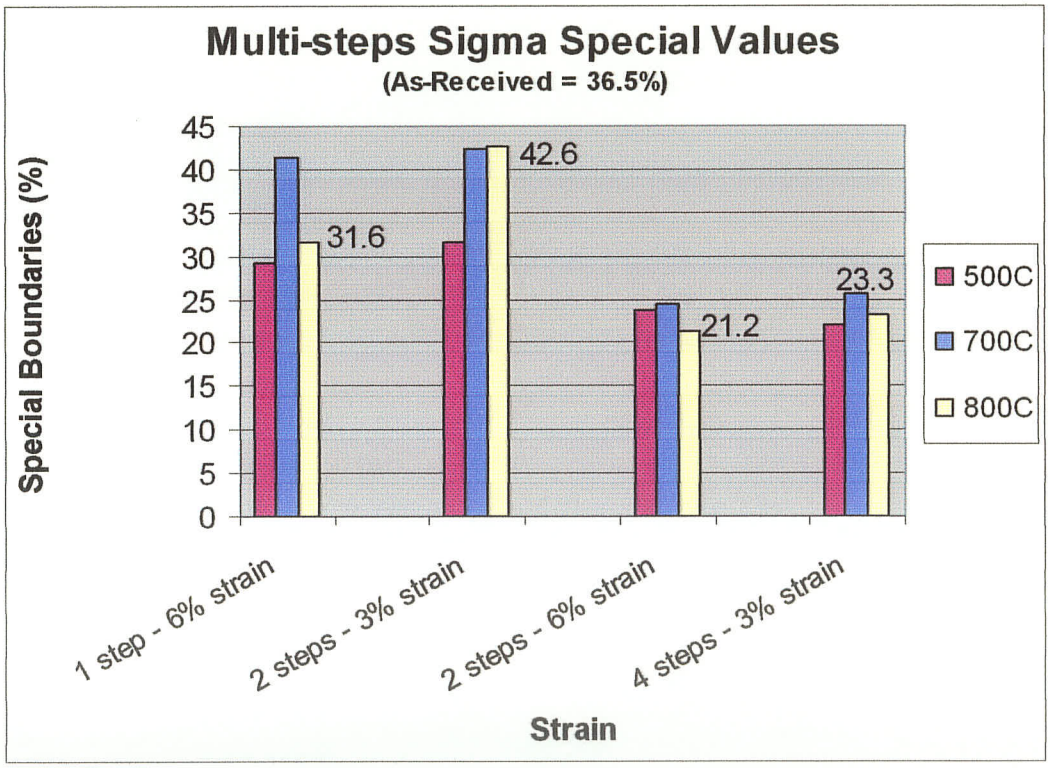

Figure 29: Multiple steps special boundaries percentage annealed at 500°C, 700°C and 800°C

Again the results of 2 steps of 6% strain and 4 steps of 3% strain (total of 12% strain) processed samples annealed at 800°C showed a low percentage of special boundaries. This was similar to samples annealed at 500°C and 700°C, with the percentage of special boundaries below the as – received sample. Thus, this approach is consistent with the trend of high strain (12% strain) and low annealing temperature ($\leq$ 800°C) results in lower special boundaries proportions than the as-received material (Σ_{sp} = 36.5%).

Grain growth was observed for all of the samples with multiple steps processed at 800°C. Grain size measurements for these samples are indicated in Table 22.

Table 22: Grain size measurements of multiple steps processing at 800°C

Process	Grain Size (μm)
1 step – 6% strain	50
2 steps – 3% strain	58
2 steps – 6% strain	55
4 steps – 3% strain	56

Only the sample processed at 2 steps of 3% strain and an annealing temperature of 800°C increased the fraction of special boundaries to 42.6%, similar to the results found in section 4.5.2.1 (results of 6% strain samples annealed at 700°C, single or multiple step processing). It is believed that recovery mechanism remains operative at 800°C, with some grain boundary migration and grain growth occurrence to enhance the special boundaries proportion. OIM maps for the sample processed with 2 steps of 3% strain, annealed at 800°C for 10minutes is shown in Figure 30.

(a)

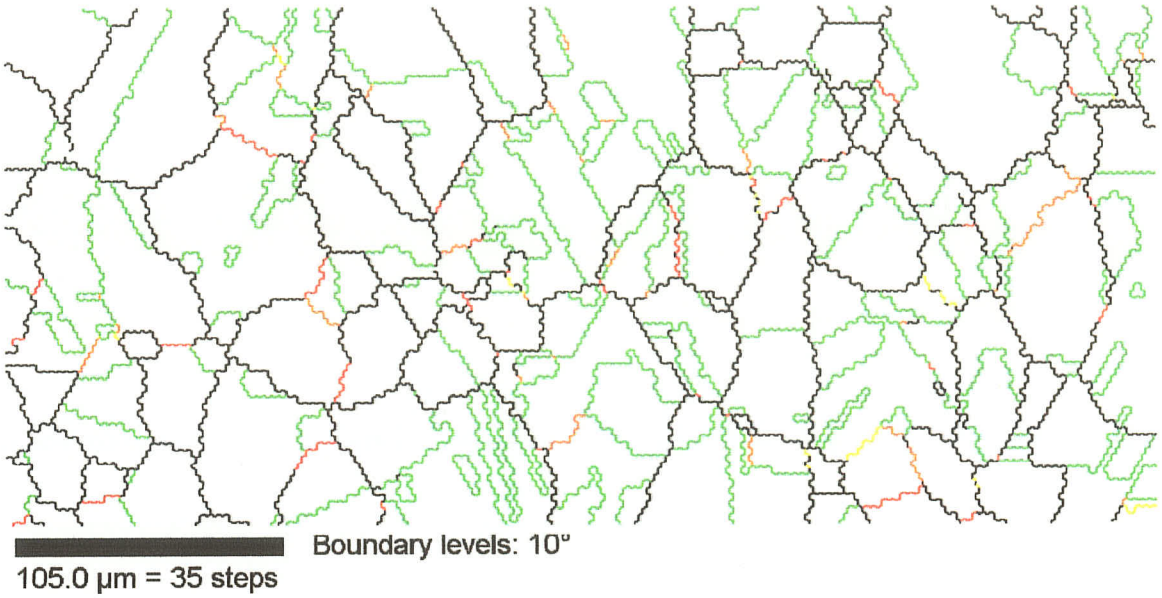

(b)

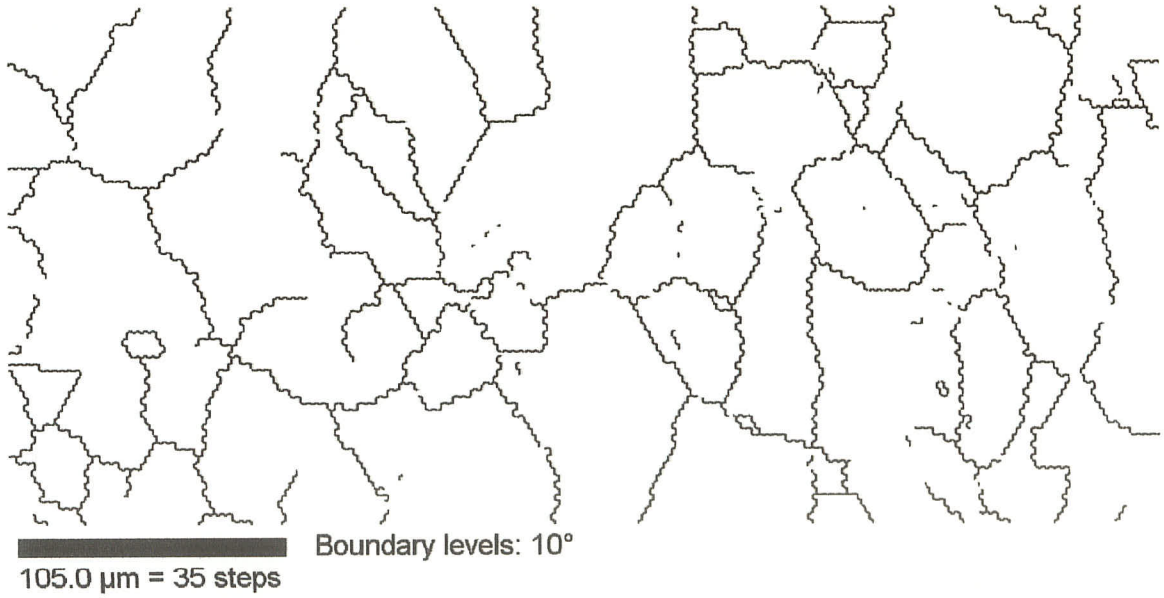

Figure 30: OIM maps of (a) grain boundary network, (b) random boundary network of 2 steps – 3% strain for a total of 6% strain annealed at 800°C

The random boundary network of Figure 30(b) appears to be insufficient to break-up the connectivity of the random boundary. High clusters of random boundaries remained in connectivity, similar to the results found in [53] when the total fraction of special boundaries is less than 50%. Continuous processing modification is necessary to further increase the fraction of special boundaries to break-up the random boundary connectivity.

With the data collected for the three temperatures so far, multiple steps strain-anneal processing of low strains (6% strain) annealed at 700°C and 800°C has enhanced the fraction of special boundaries more effectively than single step treatments. On the other hand, multiple steps strain – anneal with high strain (12% strain) have shown to lower the fraction of special boundaries. Therefore, multiple steps strain – anneal may induce a higher fraction of special grain boundaries than single step strain – anneal processing at low strains and high temperature.

4.5.2.3 Annealed at 900°C for 10minutes

The next set of experiment were analysed using an annealing temperature of 900°C, while holding the same sequence of deformation and the time of annealing constant for 10 minutes, Figure 31.

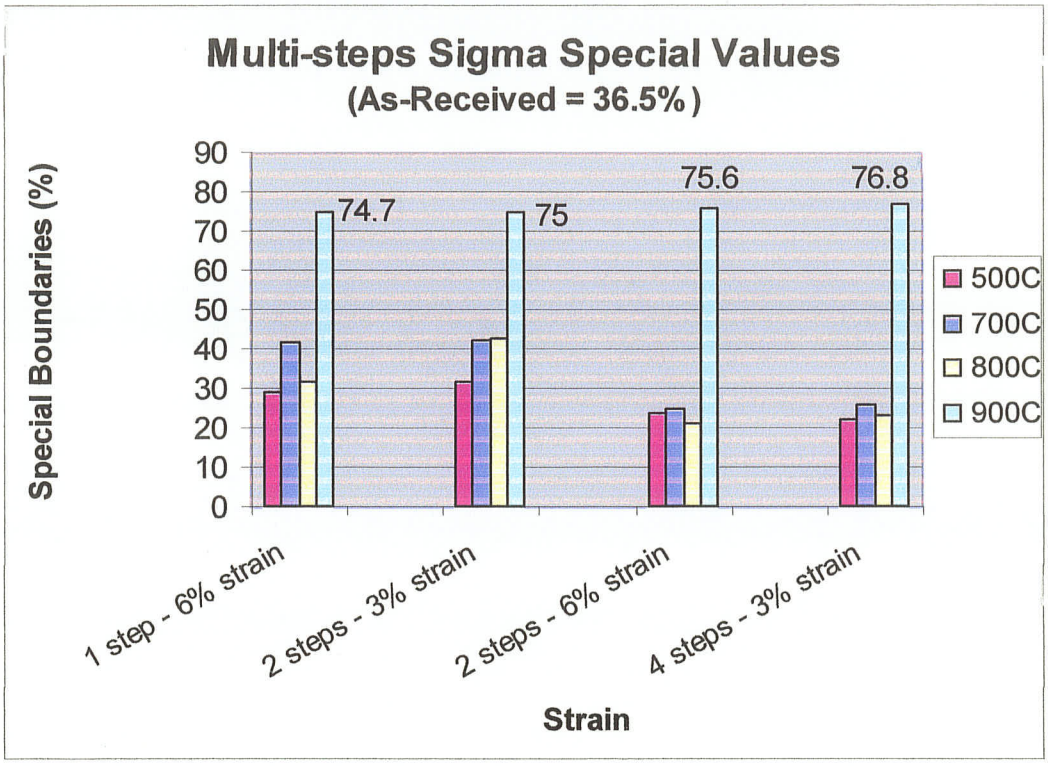

Figure 31: Multiple Steps Processing Results of Special Boundaries Percentage Annealed at 500°C, 700°C, 800°C and 900°C

Samples annealed at 900°C showed an increased of nearly twice as much of special boundaries, for all four strain and annealed samples compared to the as-received. As the annealing temperature increase, the grain size increased and the proportion of special boundaries also increased.

The dramatic increased in special boundaries processed and annealed at 900°C compared to samples annealed at lower temperatures using identical sequence of strain(s) could be explained by energy minimization processes of recovery and grain coarsening. Deformation energy stored was released during recovery by the formation of low-Σ boundaries, followed by the increase in mean grain size as grain boundary area decreases.

decreases. Even at the low percentage strains used in this thesis, recrystallization may occur and the enhanced formation of annealing twins leads to Σ_{sp} values up to 74%.

As a comparison, samples annealed at lower temperatures than 900°C formed minimal low-Σ boundaries and limited grain size increase, resulted in similar fractions of special boundaries to the as-received sample as shown in Figure 31. The observation that special boundaries fraction increase with grain size were similar to observations by Randle [25] that an increase in twinning was found with increasing grain size, and by Pande [26] that twins were determined uniquely by grain size, as shown in equation (4).

Figure 32 shows the change in grain size of microstructures processed with 6% strain, annealed with increasing temperatures.

(a) 1 step of 6% strain, annealed at 500°C. Grain size = 25μm

(b) 1 step of 6% strain, annealed at 800°C. Grain size = 50μm

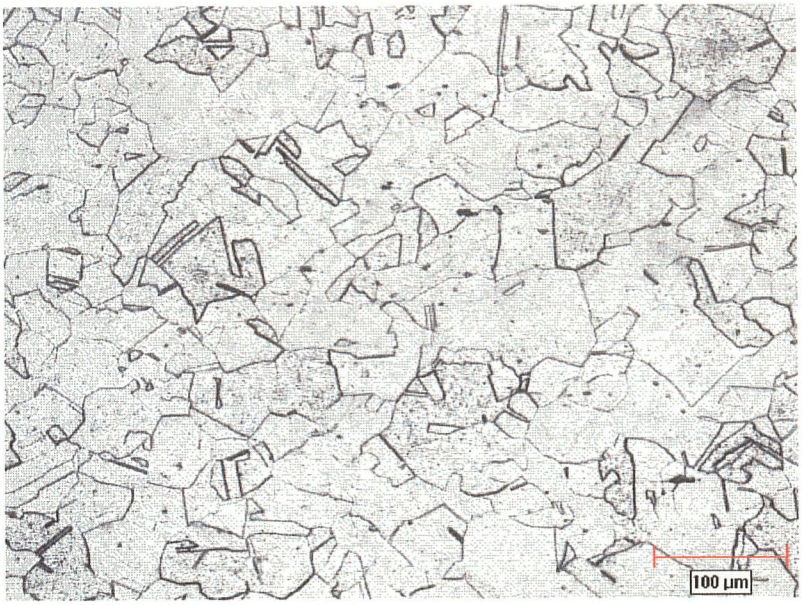

(c) 1 step of 6% strain, annealed at 900°C. Grain size = 60μm

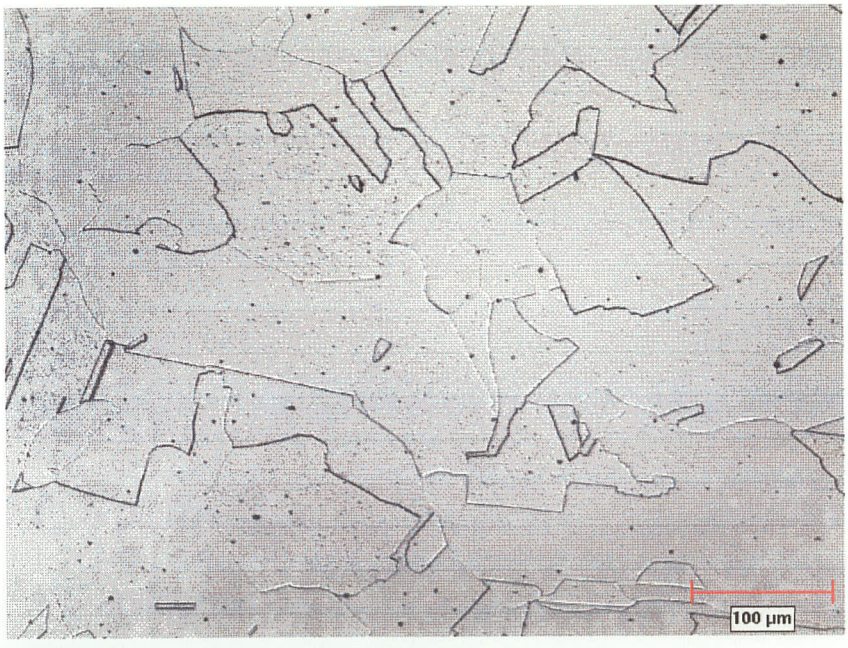

Figure 32: Microstructures of nickel annealed at (a) 500°C, (b) 800°C, and (c) 900°C 200X magnifications

The grain size of the 6% strained sample progressively increases as the annealing temperature increase, shown in Figure 32. The grain size of the as-received sample, and the four samples processed with multiple steps and annealed at 900°C are shown in Figure 33.

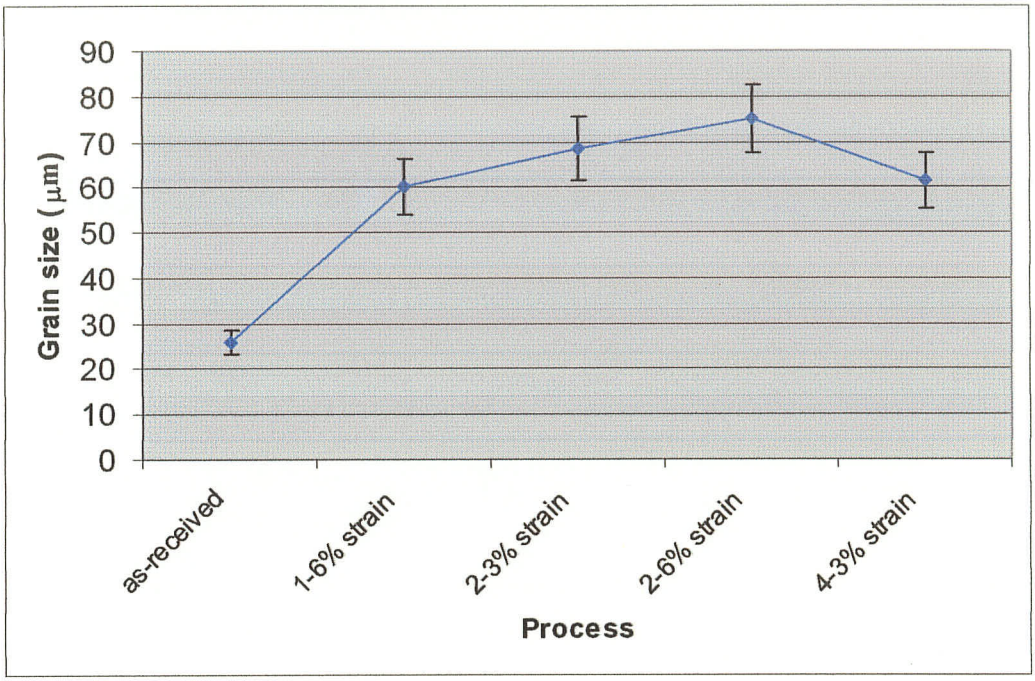

Figure 33: Grain size distribution of as-received and processed samples annealed at 900°C

Grain size values are subjected to a 95% confidence level of ±8μm using equation 10, as each measurement was averaged over 600 boundaries. An increased in grain size up to 60-75μm was observed for the samples annealed at 900°C. In the Pande et al model for twinning [26], it was described that twin density is the function of grain size only, when twinning being based on growth accidents associated with migrating boundary during annealing.

OIM images of the four multiple steps processed samples annealed at 900°C are shown in Figures 34-37.

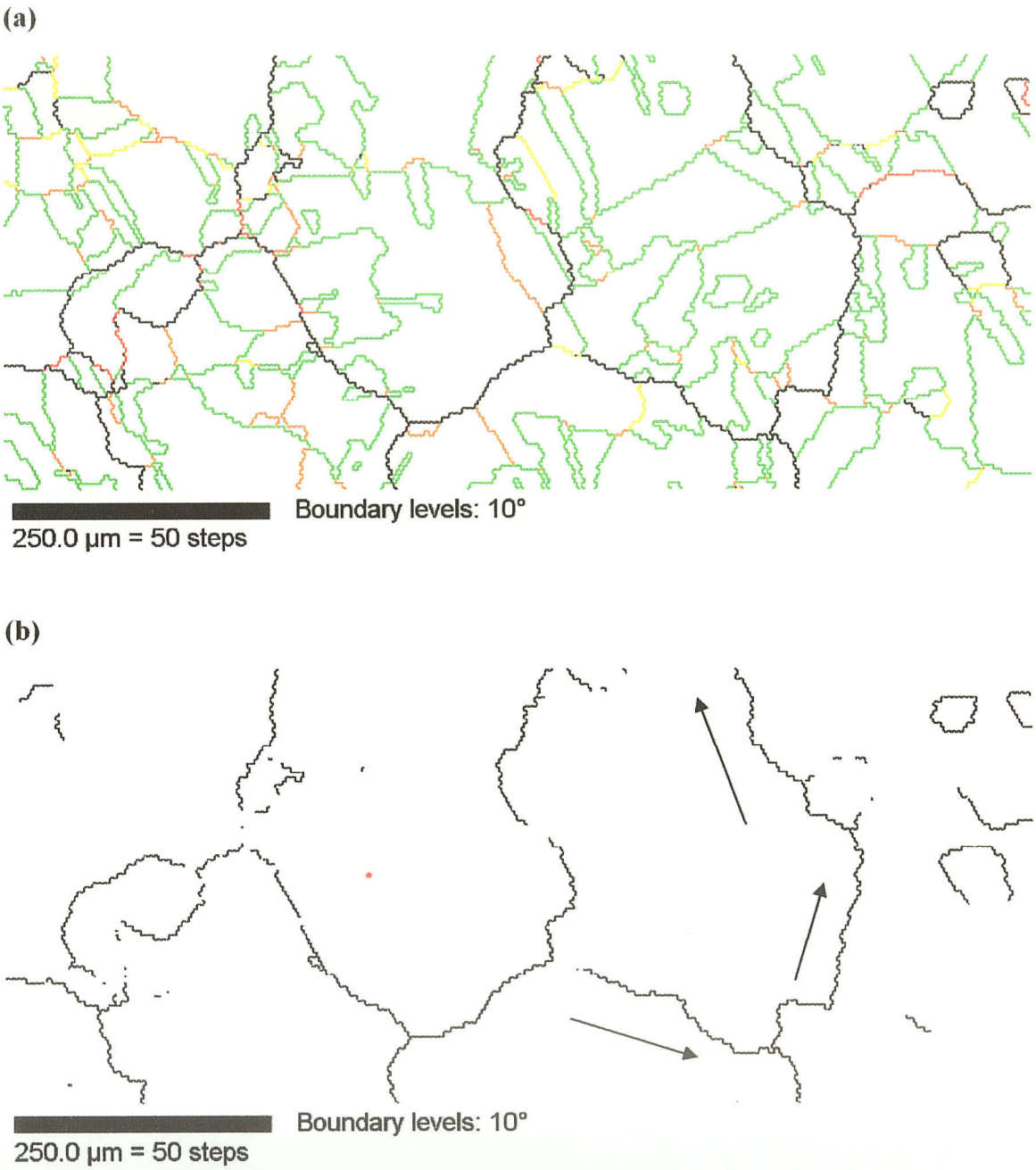

Figure 34: OIM maps of sample processed at 1 step – 6% strain at 900°C. (a) full network of grain boundaries with special boundaries colour coded, (b) only the random high angle boundary network. Grain size = 60µm

(a)

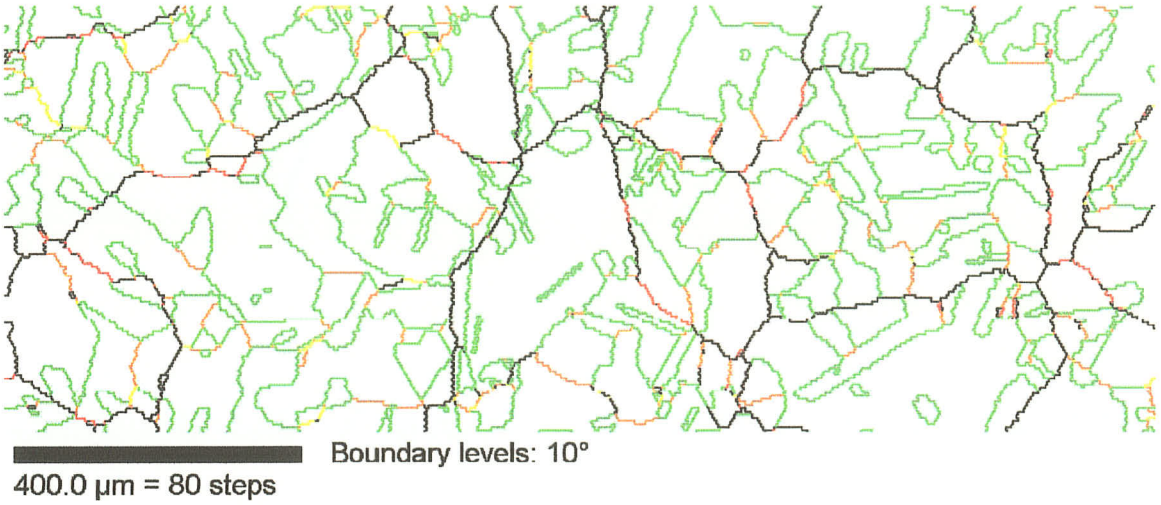

(b)

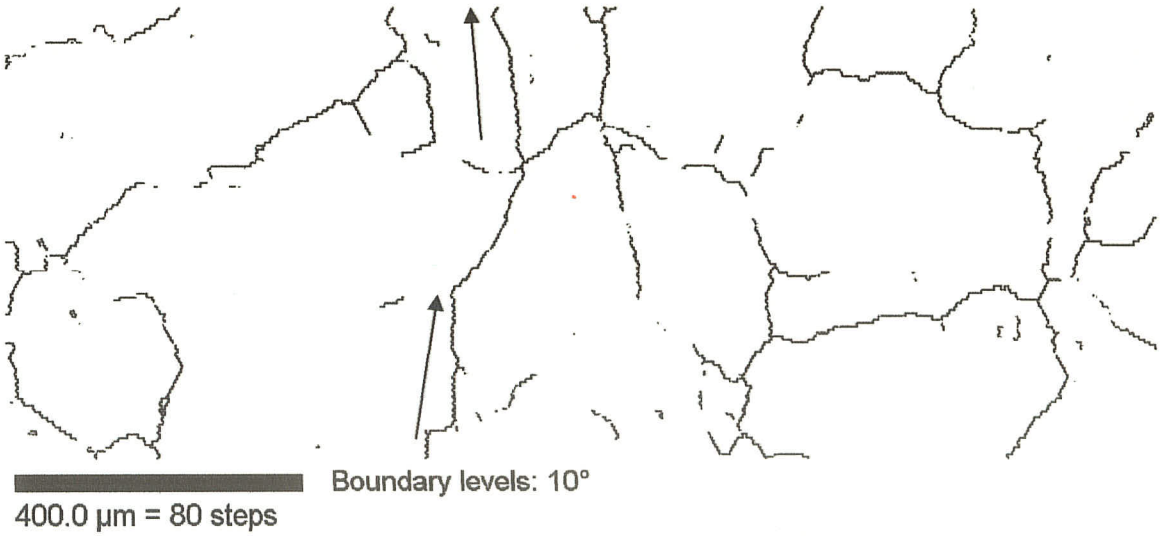

Figure 35: OIM maps of sample processed at 2 steps – 3% strain at 900°C. (a) full network of grain boundaries with special boundaries colour coded, (b) only the random high angle boundary network. Grain size = 68µm

(a)

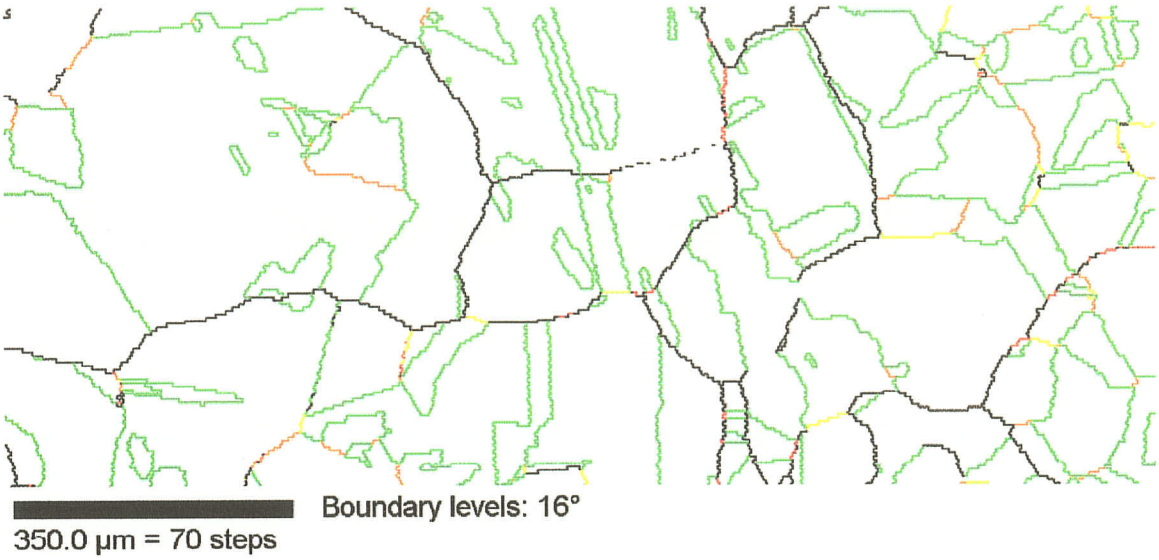

(b)

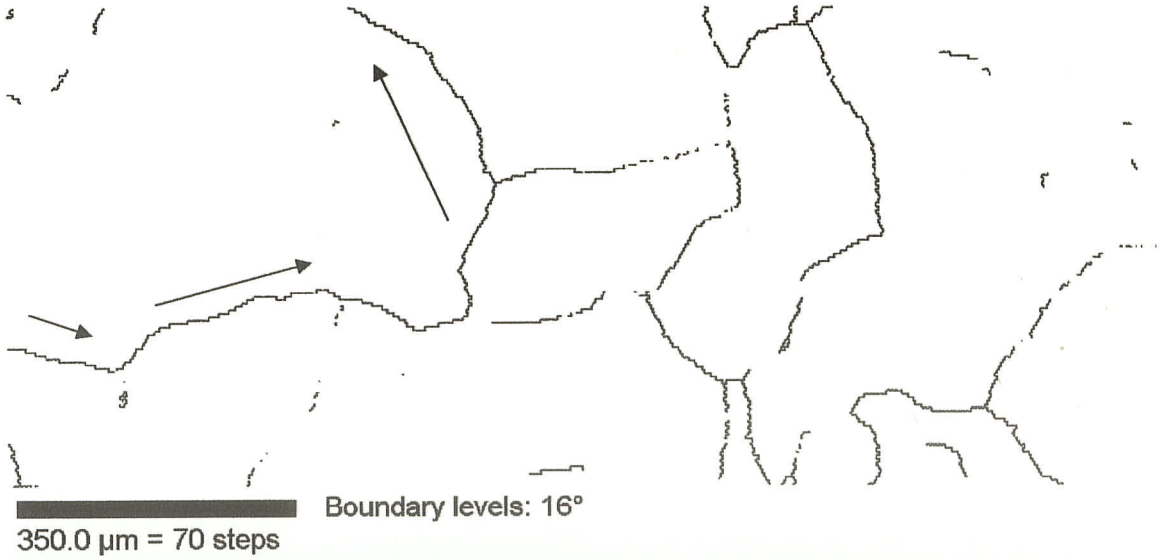

Figure 36: OIM maps of sample processed at 2 steps – 6% strain at 900°C. (a) full network of grain boundaries with special boundaries colour coded, (b) only the random high angle boundary network. Grain size = 75µm

(a)

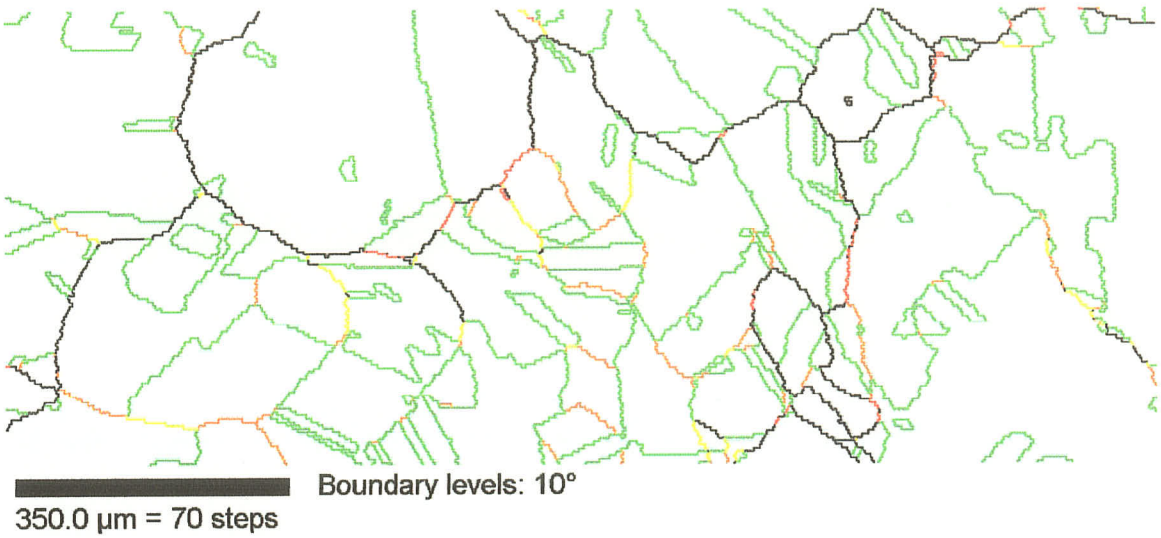

(b)

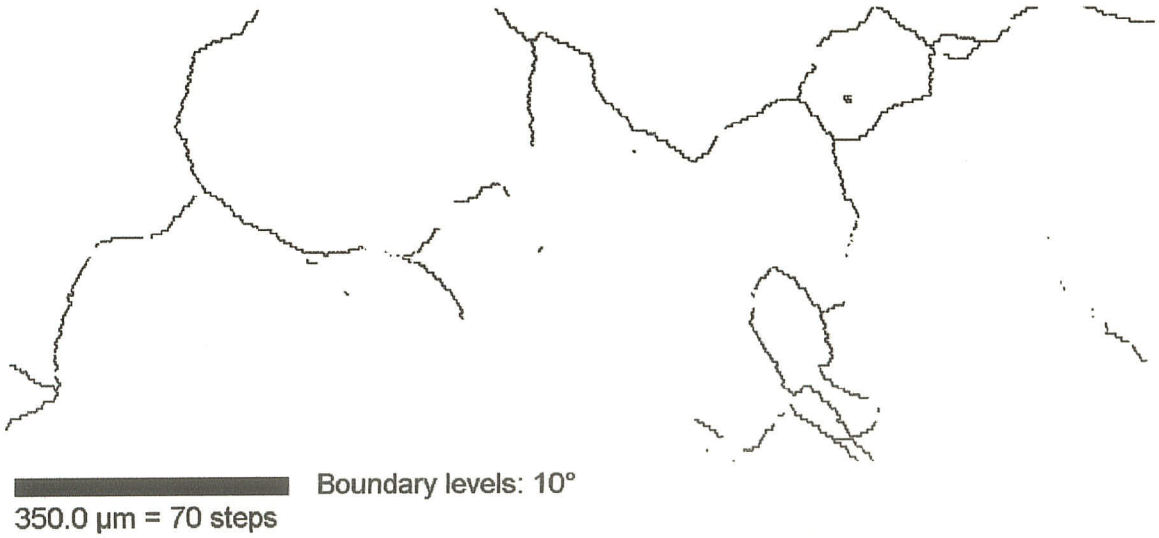

Figure 37: OIM maps of sample processed at 4 steps – 3% strain at 900°C. (a) full network of grain boundaries with special boundaries colour coded, (b) only the random high angle boundary network. Grain size = 61µm

Figures 34-37 consist of two OIM maps in each figure. OIM maps of Fig. 34-37(a) are the entire grain boundary network, and Fig. 34-37(b) are identical to Fig. 34-37(a) only with special boundaries eliminated. Grain growth was observed for these samples annealed at 900°C, with the growth of these grains being as expected larger than samples annealed at 700°C and 800°C. It can be observed that many enlarged grains were bounded by random boundaries, indicated by black lines in Figures 34-37(b) on the random boundary network maps.

A decrease in the connectivity of random boundaries has been shown in some studies [5, 6, 37, 53] that could minimize intergranular degradations. Multiple steps processed samples annealed at 900°C provided an increased fraction of special boundaries, up to Σ_{sp} ~75% and a much improved connectivity of random boundaries compared to Figure 30 for a low percentage of special boundaries. Minor clusters or a path of like boundaries, consisting of interconnected random boundaries may still exist, which are indicated by black arrows in Figures 34(b), 35(b), 36(b). These interconnected random boundaries are likely paths favoured to crack propagation.

A sample processed in 4 steps of 3% strain annealed at 900°C, with the random boundary network shown in Figure 37(b) is the only exception from the four samples annealed at 900°C that do not have a distinct path or clusters of random boundaries. Grain growth was observed in this sample as the size of each grain was approximately 61μm, and this only limited extraneous large grains bounded by random boundaries was observed.

Many interconnected random boundary paths were arrested at triple junction, formed by at least two special boundaries. An increased in the $\sum_{sp}$ fraction promotes the formation of triple junctions comprising of three low-$\sum$ CSL boundaries, to break up the random boundary continuity. Processing of 4 steps of 3% strain annealed at 900°C consisted of a combination of the highest fractions of special boundaries ($\sum_{sp}$ = 76.8%) and the observed connectivity of such secure junctions that have been proven [12] to provide invaluable protection against many detrimental effects, such as intergranular crack propagation.

4.5.2.3.1 CSL distributions

Figure 38 is the CSL boundary distribution graph of multiple steps processed samples annealed at 900°C, $3 \leq \sum \leq 29$. The legend 1-6% means, one cycle with one 6% deformation. Similarly, 2-3% means 2 cycles, each of 3% deformation, etc....

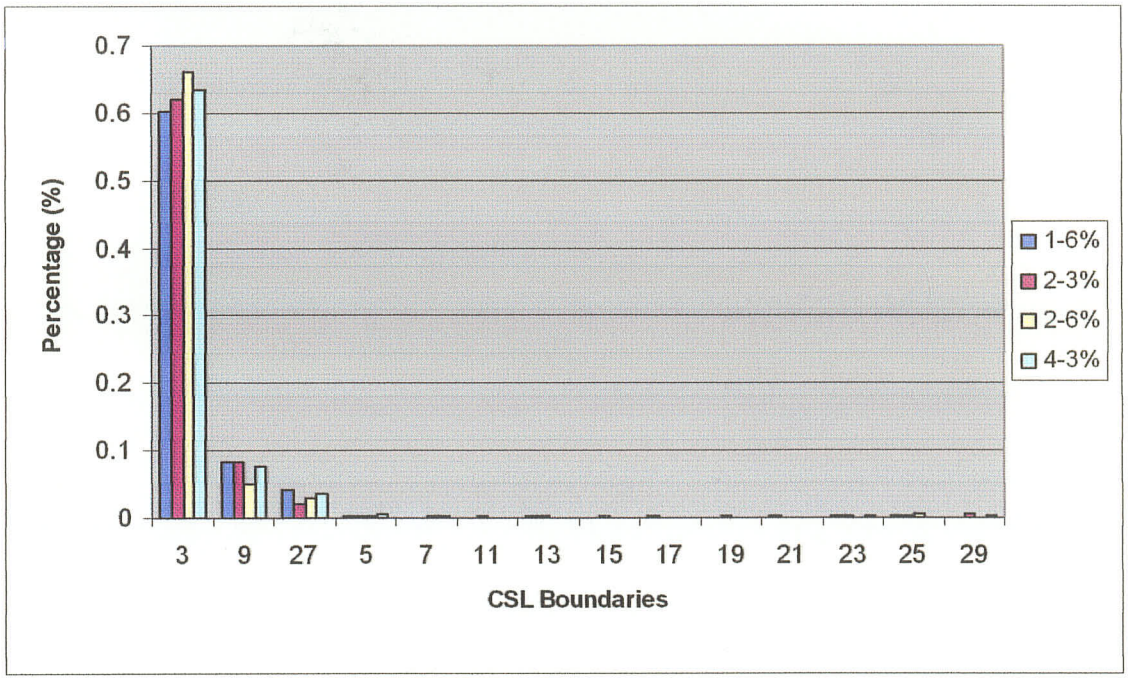

Figure 38: CSL distributions of multiple steps processing samples annealed at 900°C

Detailed values for the CSL distributions of for the four samples annealed at 900°C can be seen in Appendix A1. Figure 38 shows that the majority of the increased levels of special boundaries were derived from the evolution of $\Sigma 3$ twin boundaries and $\Sigma 3^n$ ($\Sigma 9$ and $\Sigma 27$s), which were referred to as twin related variants [Randle and Brown, 1989]. According to Mahajan et al [71], grain boundary movement is needed for twin formation, with the driving force being proportional to grain size, such as boundary curvature.

The break up of the connectivity of the random boundary network in turn is effectively accomplished by the integration of $\Sigma 3$ twin boundaries into the network of grain boundaries. This correlates to Guo's work [54] that twins formed by models such as Pande et al [26], produce $\Sigma 3$ twins across grains which alter the grain boundary

characteristics of the HAB's. It was shown that CSL boundaries of $\Sigma 15$ and $\Sigma 23$ segments were intersperse between HAB segments. A stress corrosion crack running along this boundary is likely to be arrested by the low CSL segments. Evidence highlighting the importance of twinning is presented in Figure38, which correlates the frequency of $\Sigma 3$ boundary and low-Σ special boundaries for $3 \leq \Sigma \leq 29$.

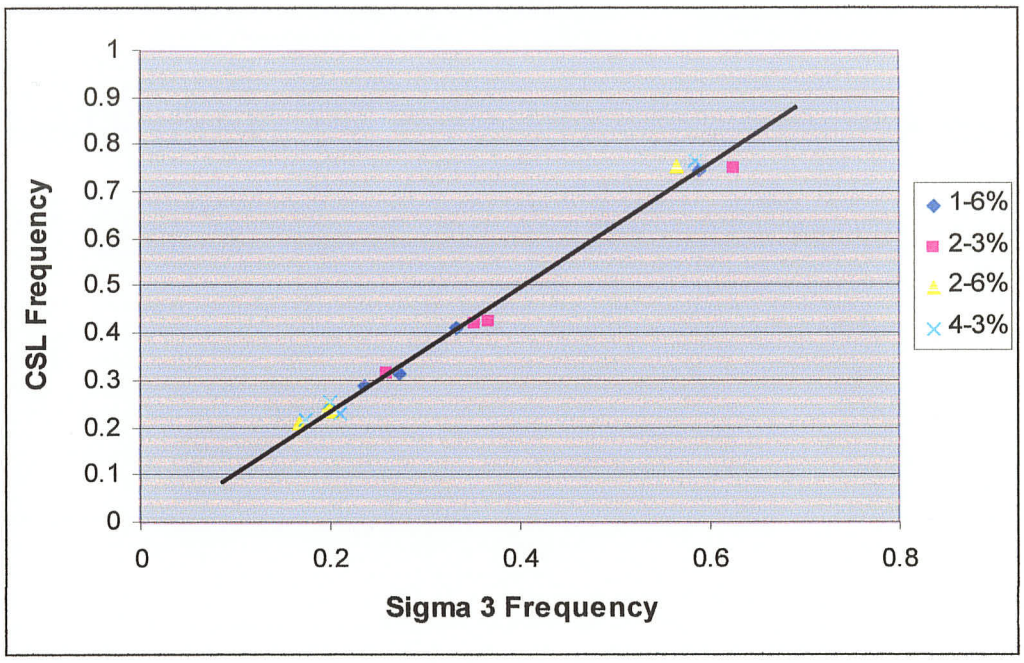

Figure 39: Contribution of annealing twins ($\Sigma 3$) to grain boundary characteristic distribution ($3 \leq \Sigma \leq 29$). A linear relationship exist as $\Sigma 3$ boundaries increases with special boundaries between Σ 3 and Σ 29

Four temperatures (500°C, 700°C, 800°C and 900°C) were plotted for each set of strain sequence. In Figure 39, 1-6% represents one step of 6% strain; 2-3% represents two steps of 3% strain, etc.... As the annealing temperature increased for each set of strain sequence, the fraction of special boundaries increased. This indicates that the increased in total fraction of special boundaries directly increases with thermal treatment.

It was also observed that increasing the annealing temperature increases the grain size. Multiple steps processing of samples annealed at 900°C showed an increased in grain size (Figure 34), and a dramatic increased in special boundaries, which contains mostly twins and twin variants. A correlation between grain size and twin fraction exists, and it is shown in Figure 40.

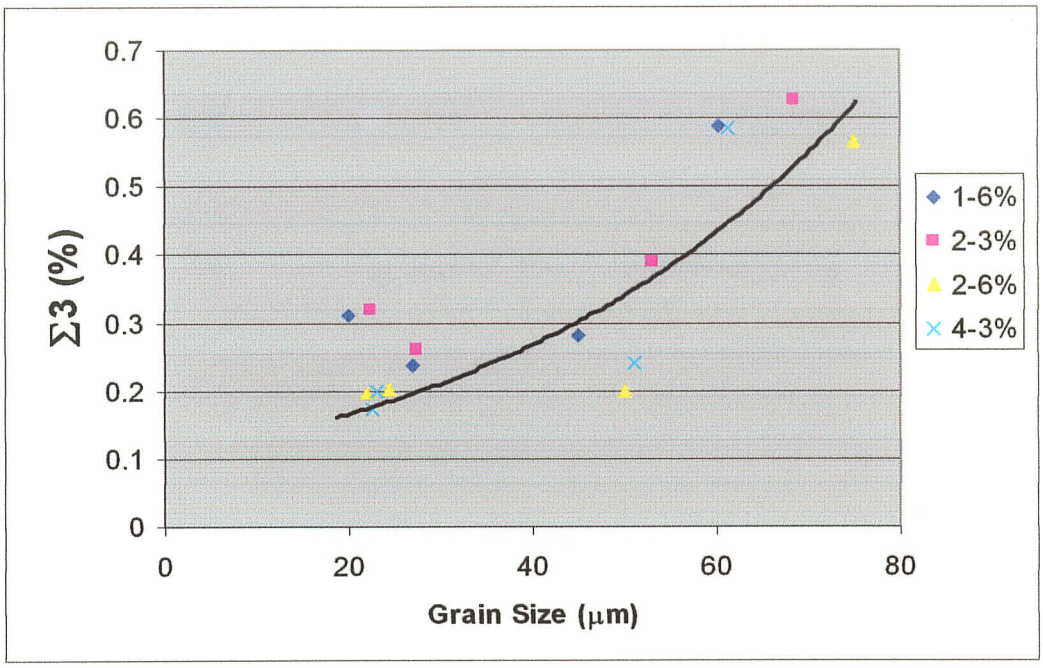

Figure 40: Graphical representation of the effects of grain size on the distribution of ∑3 boundaries at annealing temperatures 500°C, 700°C, 800°C and 900°C

Temperatures 500°C, 700°C, 800°C and 900°C were plotted for each set of strain sequence, indicated by the legend on the right of the graph. Low percentage of ∑3 boundaries were recorded for grain size between 20-50μm (samples annealed from 500°C to 800°C). As the grain size increased to 60μm or higher (900°C samples), the percentage of ∑3 nearly doubled, shown in Figure 40. The observation that ∑3 twin boundaries can increase with grain size are similar to observations by King and Schwartz [43], and

Pande's equation [26, 27]. The driving force for grain growth was by the migration of grain boundaries at elevated temperature (900°C), decreasing the total boundary area, to yield an attendant reduction in the total grain boundary energy and to form twins.

The percentage of $\Sigma 3$ boundaries is almost 80% of the total Σ_{sp} boundaries examined thus far. The increased frequency of $\Sigma 9$ and $\Sigma 27$ in addition to $\Sigma 3$ shown in Figure 38, support the observation made by Randle [9] and by Palumbo [45] that the enhanced frequency of special boundaries was predominantly due to the repeated geometric interaction of twin related variants. The relationship developed for $\Sigma 3$ boundary and low-Σ special boundaries, where multiple twinning or twin intersection events at $\Sigma 3^n$ boundaries raised from the geometrical necessity of connecting multiple $\Sigma 3$ boundaries in the grain boundary network.

By maximizing the proportion of twins, superior grain boundary properties should occur when considering random high angle boundaries are reduced and lengths of HAB's are broken up by intersection of twins with HAB's. It is now verified that the formation of annealing twins contributes directly to the special boundary fraction for these grain boundary engineered samples.

4.5.2.4 One Step Strain Anneal at 900°C

It was shown in Figure 31 that samples from multiple steps processing annealed at 900°C resulted with the highest fraction of special boundaries so far. A set of experiment of one step, strained at different strain levels and annealed at 900°C were processed to

determine the effects on the distribution of special boundaries against multiple steps strain – anneal processed samples annealed at 900°C.

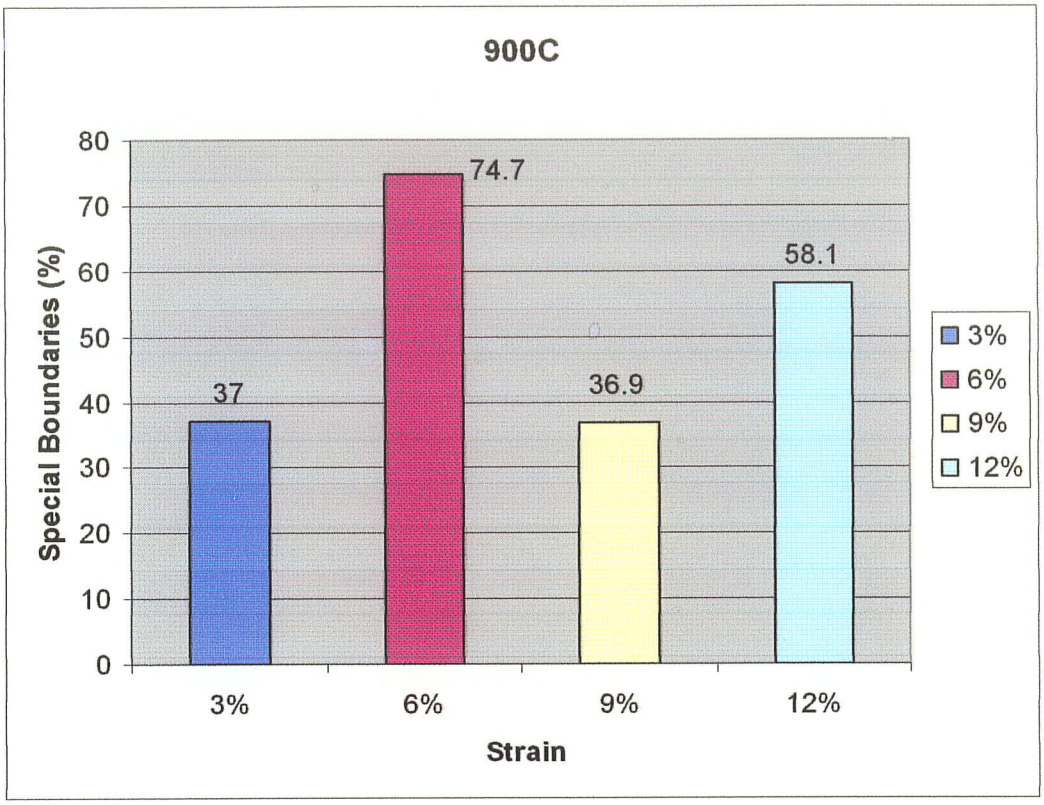

Figure 41: One Step Strain - Anneal Processed Samples, annealed at 900°C

Results of single step processing with 3%, 6%, 9% and 12% strain, annealed at 900°C are shown in Figure 41. It is clearly shown that a low strain level of 3% does not enhance the total faction of special boundaries, when compared to the as-received material with $\Sigma_{sp} = 36.5\%$. It is believed that insufficient cold work was stored to accumulate the proper boundary conditions to rearrange these boundaries into low-Σ boundaries types. An input of 6% strain contains sufficient amount of deformation energy to initiate recovery to form low-Σ grain boundaries, and as a consequence increased the

percentage of special boundary to 74.7%. As the applied strain increased to 9% and 12%, the proportion of Σ_{sp} dropped below the 1 step of 6% strain sample. OIM maps of grain boundary network and random boundary network are illustrated in Figures 42-45.

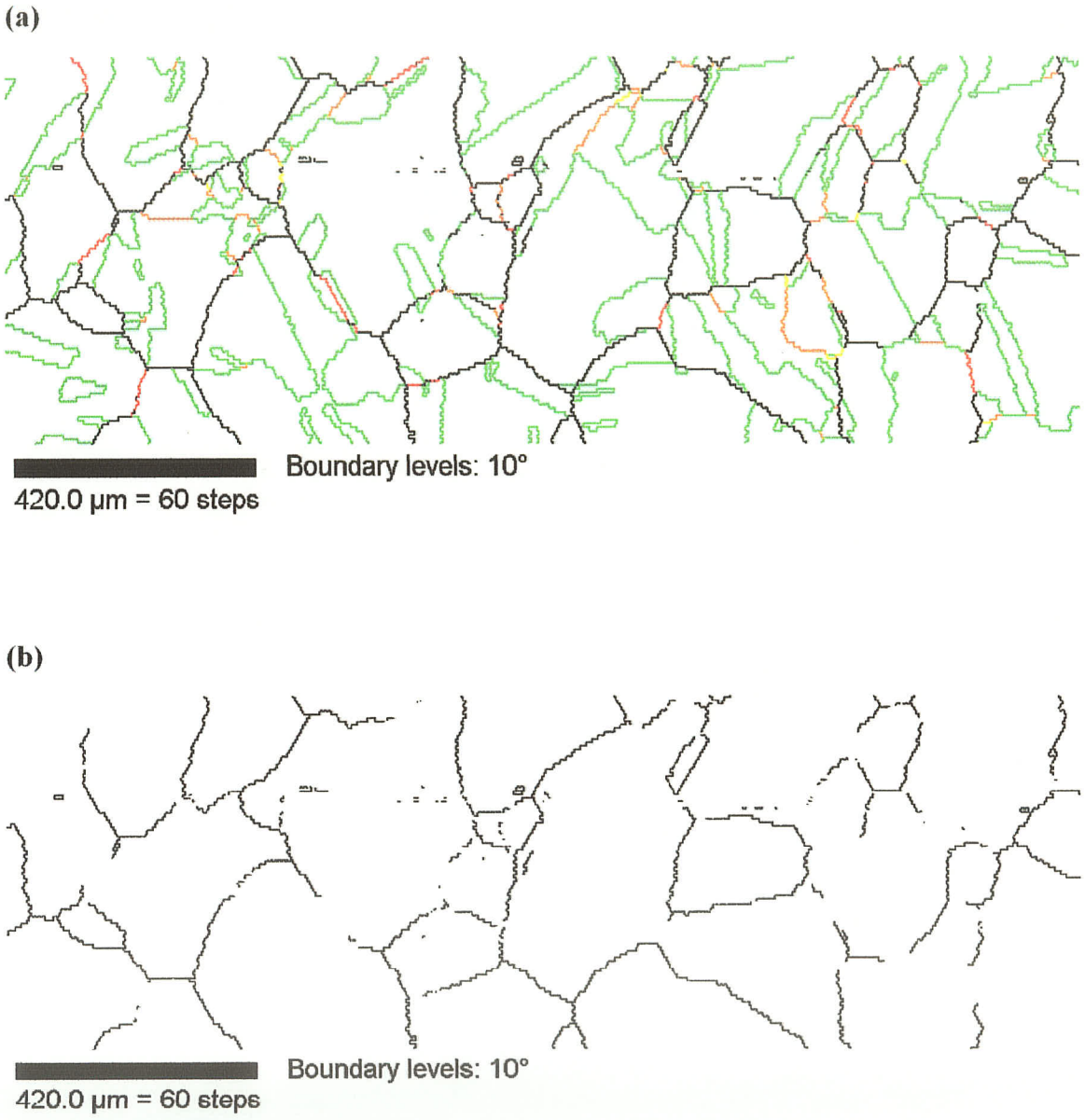

Figure 42: OIM maps of sample processed at 1 step – 3% strain at 900°C. (a) full network of grain boundaries with special boundaries colour coded, (b) only the random high angle boundary network. Grain size = 66.4µm

(a)

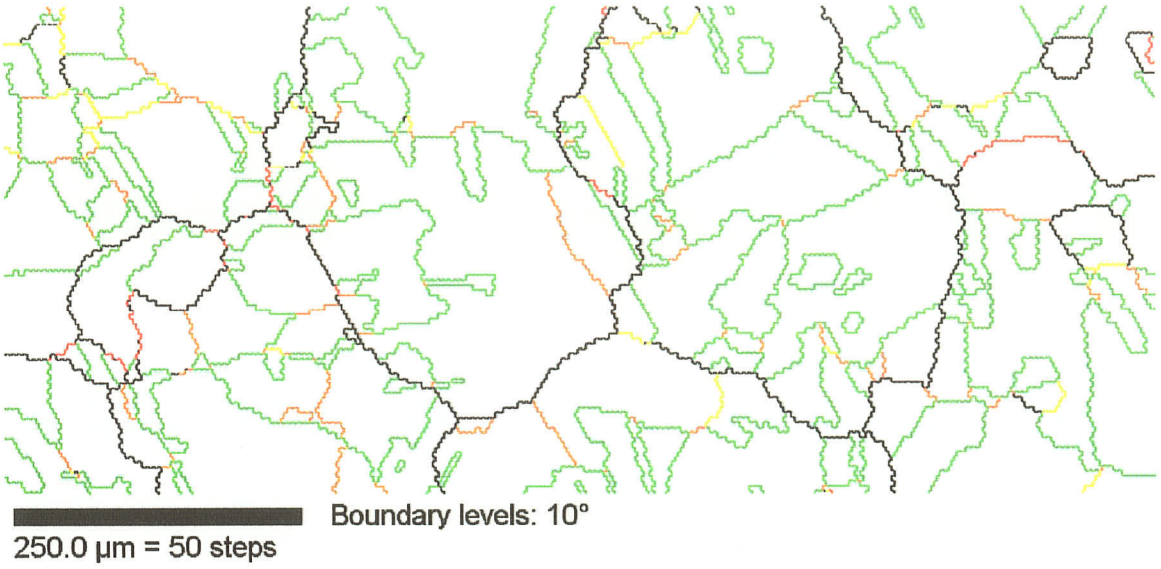

(b)

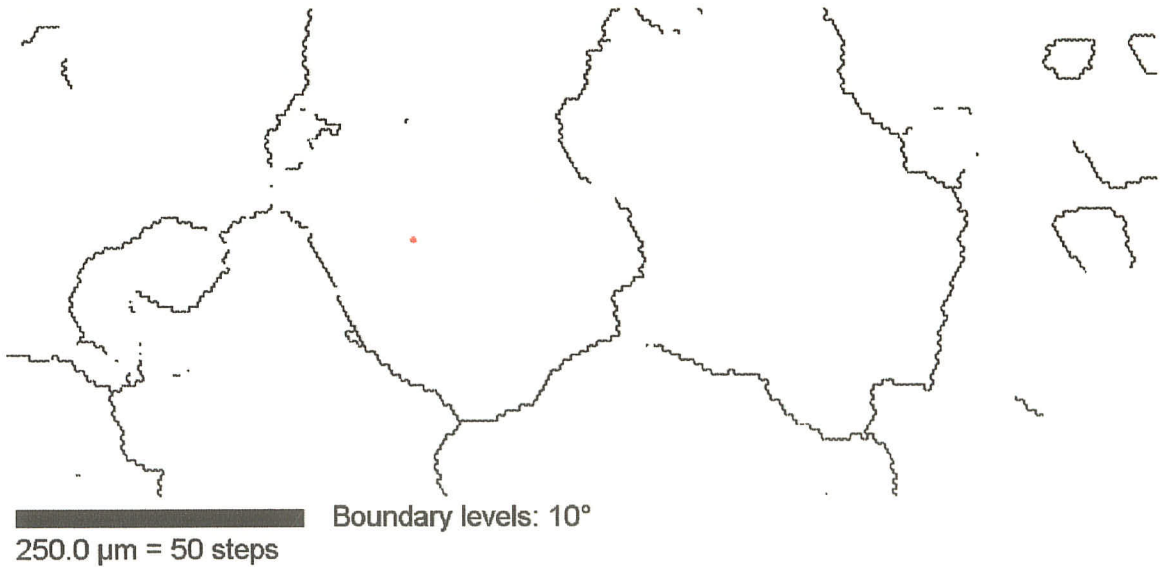

Figure 43: OIM maps of sample processed at 1 step – 6% strain at 900°C. (a) full network of grain boundaries with special boundaries colour coded, (b) only the random high angle boundary network. Grain Size = 60.2µm

(a)

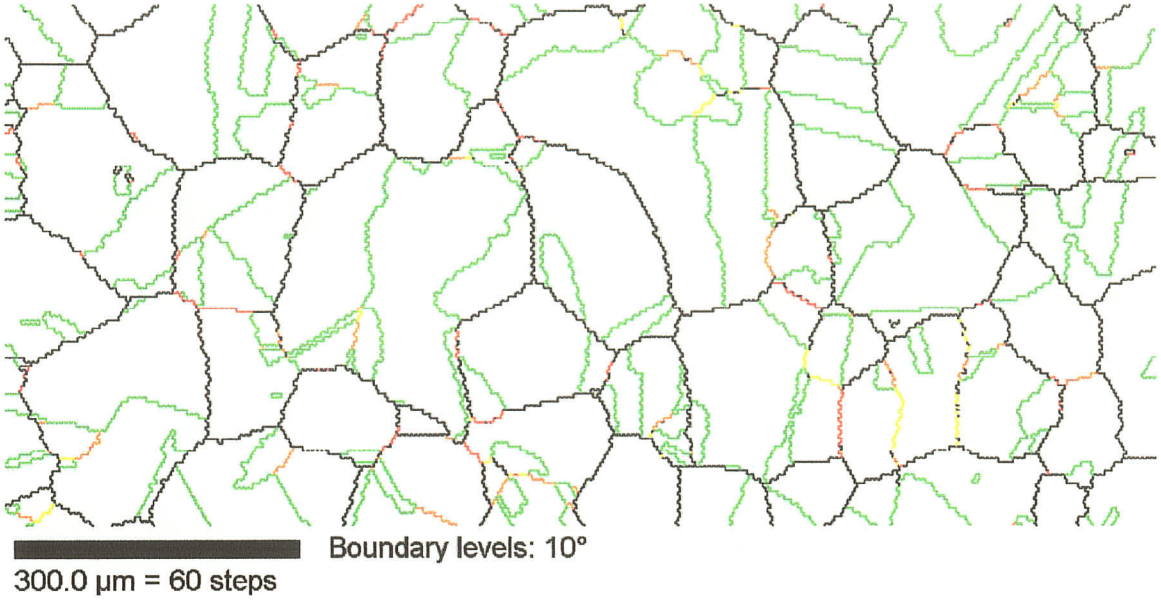

(b)

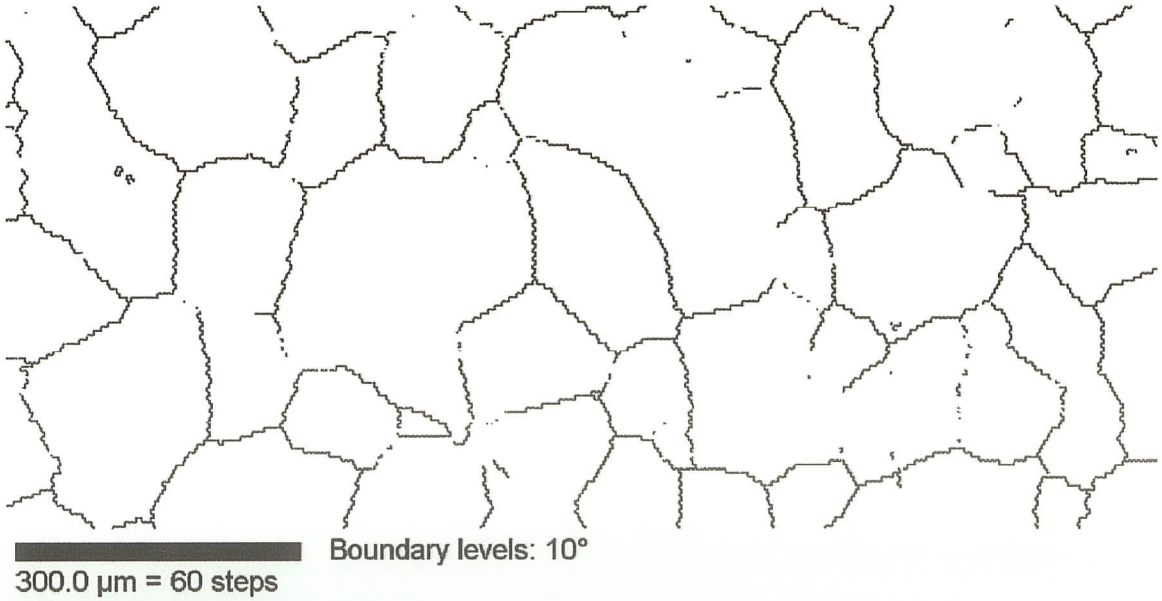

Figure 44: OIM maps of sample processed at 1 step – 9% strain at 900°C. (a) full network of grain boundaries with special boundaries colour coded, (b) only the random high angle boundary network. Grain size = 76µm

(a)

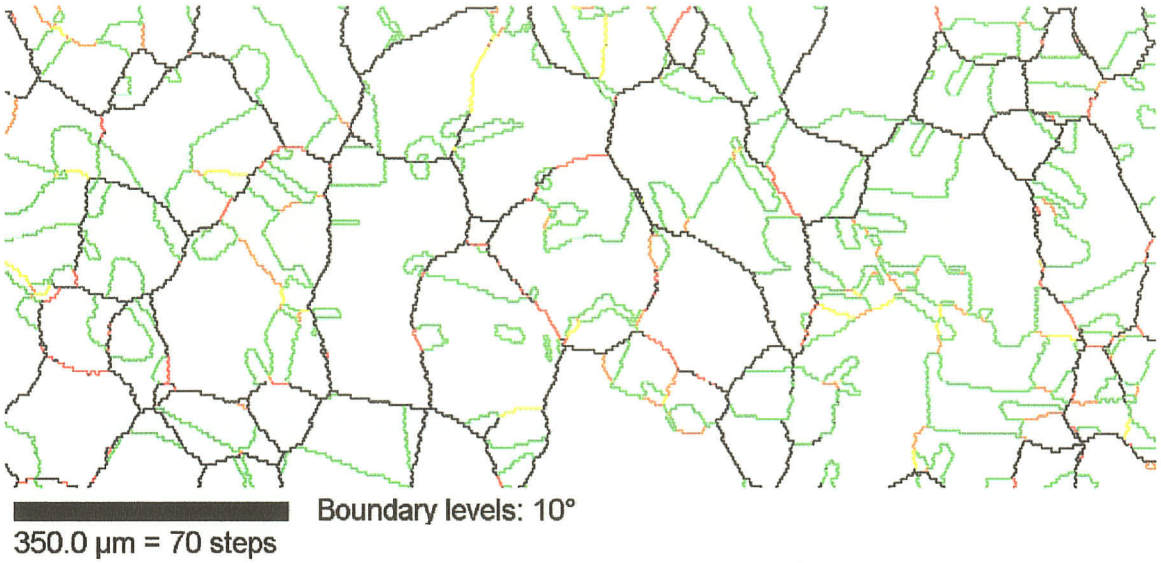

(b)

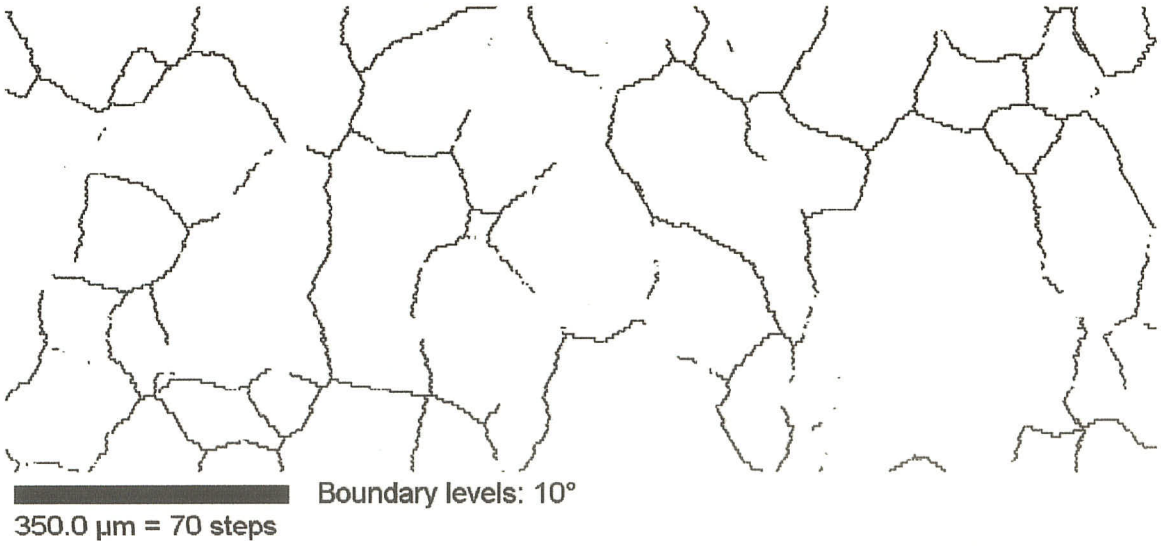

Figure 45: OIM maps of sample processed at 1 step – 12% strain at 900°C. (a) full network of grain boundaries with special boundaries colour coded, (b) only the random high angle boundary network. Grain size = 83µm

Figures 42(b), 44(b) and 45(b) show random boundary network maps of samples strain and annealed at 900°C. These OIM maps have a high connectivity of random boundaries and low fractions of special boundaries. It has been shown in [5, 6, 37, 52, 53] that high clusters of random boundaries interconnected were susceptible to intergranular failures. Although the sample of one step of 6% strain annealed at 900°C shown in Figure 43 has a high fraction of special boundaries, it was previously discussed that an undesired high proportion of random boundaries connected within a volume are potentially disastrous, since random boundaries are considered as favour sites for crack nucleation and propagation. Therefore, these one-step processed samples annealed at 900°C are undesirable processing routes to improve intergranular degradation properties.

4.5.2.5 Annealed at 1000°C for 10minutes

Experiments outlined in [25] showed a steady increase in special boundaries with increasing annealing temperature for commercially pure nickel, described by grain growth kinetic contributions as the role for the development of special boundaries. With success in improving the total fraction of special boundaries to Σ_{sp} ~75%, by increasing the annealing temperature up to 900°C, higher annealing temperatures such as 1000°C were tested to observe possible changes in grain boundary characteristic distribution.

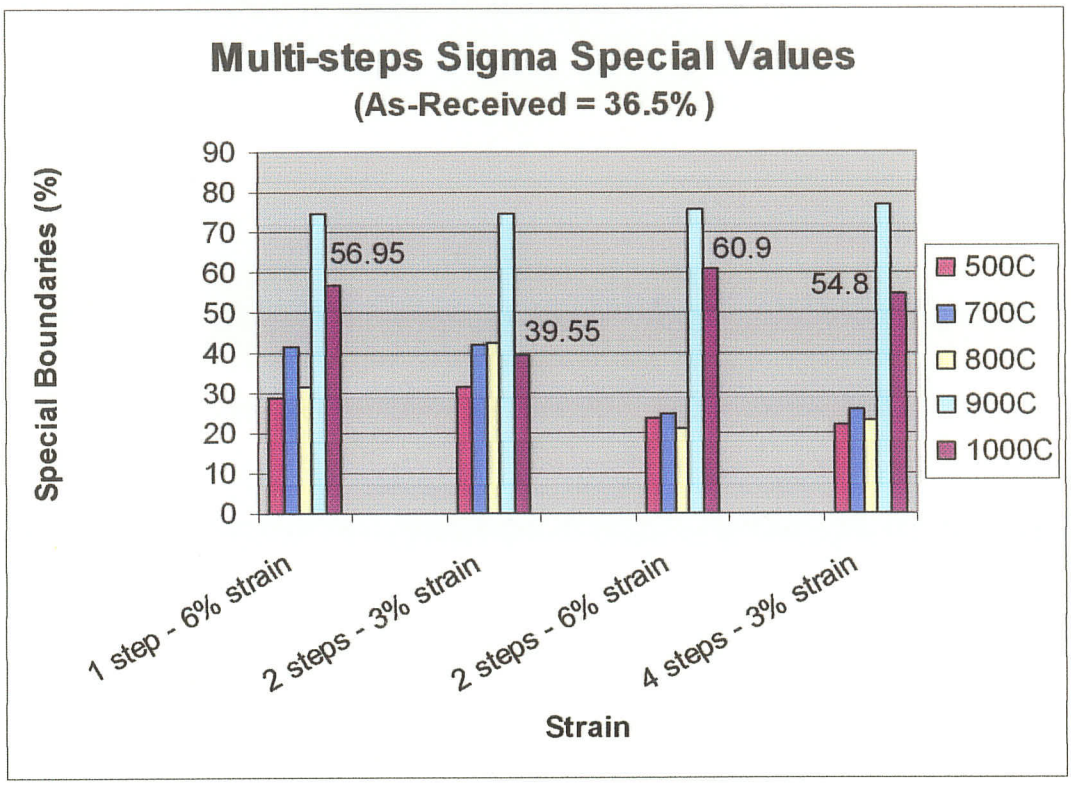

Figure 46: Multiple Steps Processing Results of Special Boundaries Percentage Annealed at 500°C, 700°C, 800°C, 900°C and 1000°C

Figure 46 is a bar graph showing all of the multiple steps strain – annealed samples processed against percentage special boundaries, including samples annealed at 1000°C. On evaluating the effect of processing at 1000°C, it can be observed that the fraction of special boundaries dropped for each strain levels compared to samples annealed at 900°C. An increased in grain size was also found for all four samples compared to samples annealed at 900°C. Figure 47 shows the grain size of the as-received sample and samples annealed at 900°C and 1000°C.

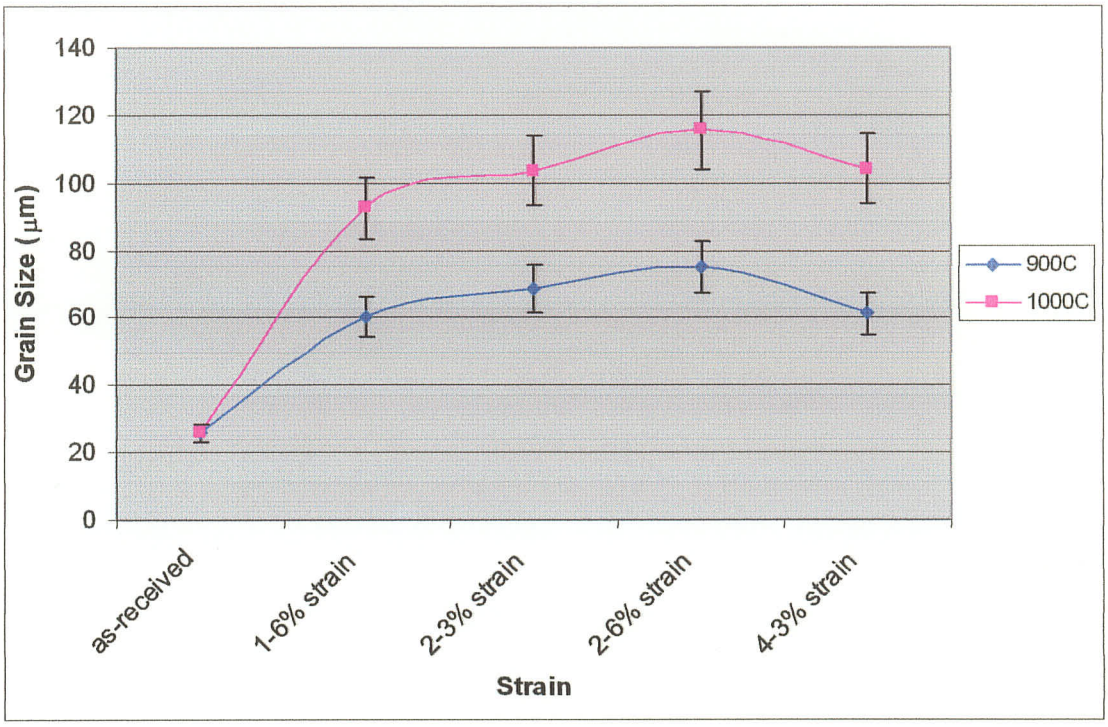

Figure 47: Grain size distributions of the as-received sample, and samples strained and annealed at 900°C and 1000°C

The difference in grain size for samples annealed at 900°C and 1000°C is some 30 - 40μm. It is believed that an undesired increased in grain size reduced the fraction of special boundaries. Grain growth caused a rapid migration of high angle boundaries to sweep across each grain, destroying newly formed low-Σ boundaries and the special fraction of grain boundaries is reduced below the optimum values achieved, Table 46.

Grain boundary network and random boundary network OIM maps of samples annealed at 1000°C are shown in the Appendix A2. Areas of large grain size bounded by random boundaries can be observed for samples with lower fractions of special boundaries. The sample of 2 steps of 6% strain showed the greatest fraction of special boundaries (Σ_{sp} = 60.9%) out of all the samples annealed at 1000°C and it can be

observed in Figure A2(g) that it has the least proportion of random boundaries showing connectivity, even less random boundary connectivity than samples with $\Sigma_{sp} > 70\%$ (i.e. multiple steps samples annealed at 900°C). The reason is that this sample has the largest grain size (115.7μm) out of all the samples annealed at 1000°C, less numbers of grains was collected in a single analysis to make a direct comparison to other images with more grains.

The sample processed with 2 steps of 3% strain annealed at 1000°C showed a significant reduction in special boundary percentage compared to the other three samples. It was accompanied by the high temperature anneal at a low sequence of pre-strain, 3% strain per step, resulted in grain growth rather than the formation of low-Σ boundaries. Samples with higher deformation (6% strain) or multiple steps of 3% strain (4 steps), resulted in a higher proportion of special boundaries, at $\Sigma_{sp} \sim 55\%$, because sufficient amounts of energy were stored for grain boundaries to migrate.

Detailed CSL distributions of the four samples processed at 1000°C can be viewed in A3. Graphical representation of the CSL distributions is shown in Figure 48.

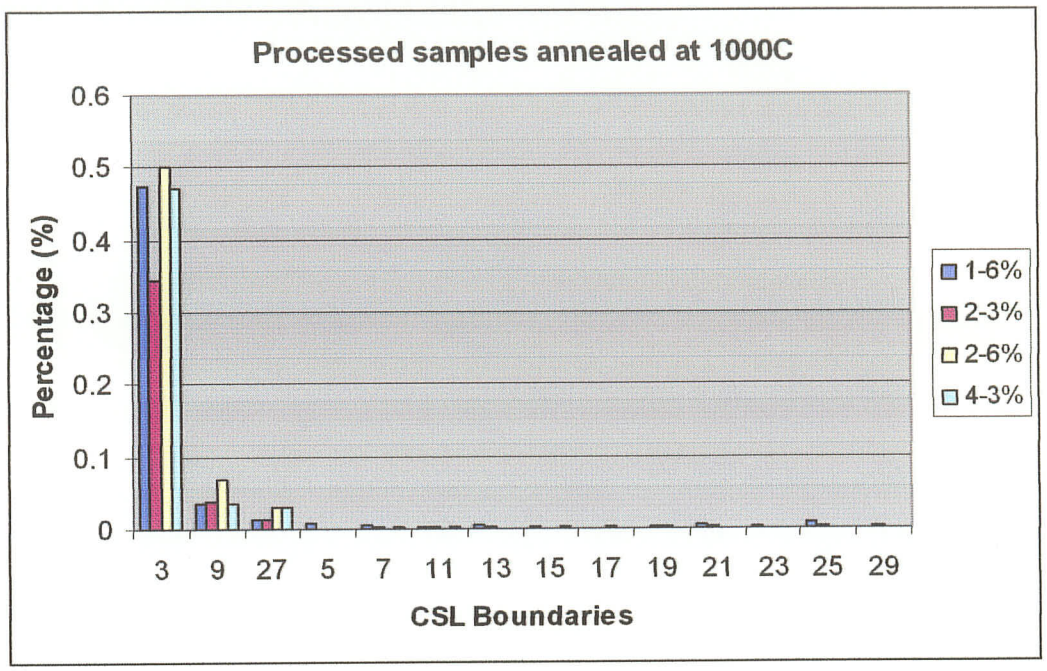

Figure 48: CSL distributions of multiple steps processing samples annealed at 1000°C

Once again, $\Sigma 3$ twin boundary and $\Sigma 3^n$ twin variant boundaries dominated the majority of special boundaries. The fraction of $\Sigma 3^n$ boundaries consistently maintained over 90% of the total special boundaries for each sample.

Experiments from previous section showed that samples with grain growth from 25.9μm (as-received) to 60-75μm (annealed at 900°C) generated a high fraction of special boundaries (mostly twin boundaries). The role of twins during grain growth has not been clearly resolved in the literature. Experiments have been observed where twins annihilate during excessive grain growth as random boundaries sweep through [23]. Other work showed an increased in twins during grain growth [22, 26, 27]. Figure 49

shows the effect of grain size on the distribution of Σ3 boundaries (reproduced from Figure 40), as the 1000°C annealed samples are included.

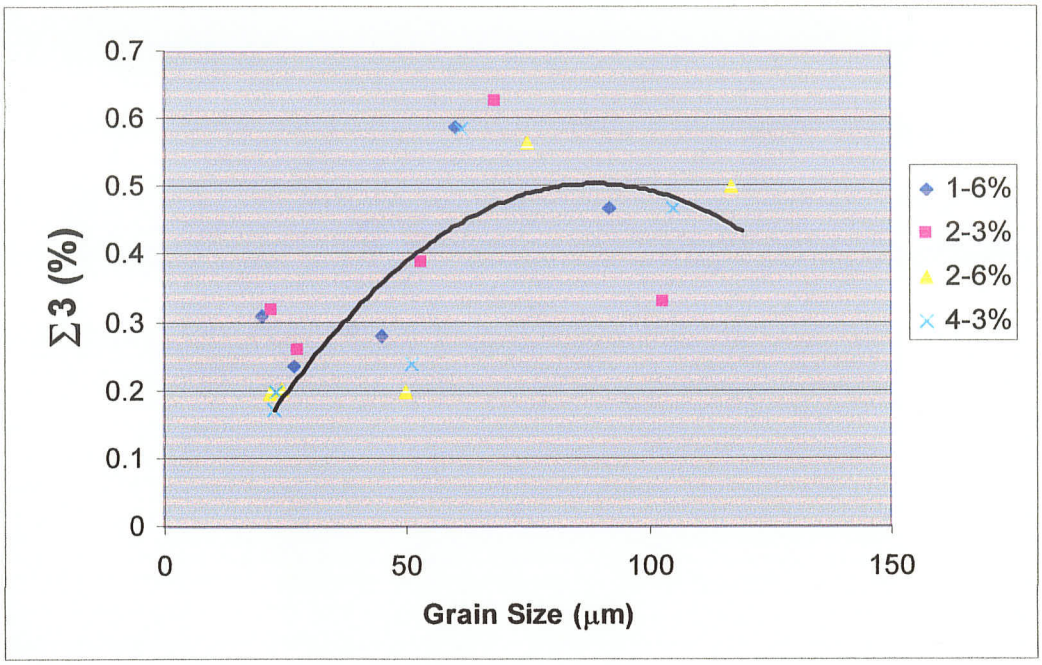

Figure 49: Graphical representation of the effects of grain size on the distribution of Σ3 boundaries at annealing temperatures 500°C, 700°C, 800°C, 900°C and 1000°C

It can be observe in Figure 49 that the fraction of Σ3 boundary reduces as the annealing temperature rose to 1000°C, and the grain size increased to 90-110μm. In this case, the equation Pande stated in [26, 27] for twin boundaries to increase with grain size is only valid up to a grain size of ~70μm, with the proportion of twin density decreasing as the grain size increased beyond this value. It is found that annealing temperature is an important factor and that excessive (1000°C), or reduced temperature (≤ 800°C), could significantly affect the total fraction of special boundaries.

From the results shown in the thesis, it is predicted that annealing samples at temperatures higher than 1000°C, with the same sequence of strains and a time of anneal at 10 minutes would not improve the final fraction of special boundaries, as much as samples annealed at 900°C. The most desire processing route discovered up to now for an annealing time of 10 minutes is 4 steps – 3% strain annealed at 900°C. This sample produced the highest fraction of special boundaries, at 76.8% shown in Figure 31 and the least proportion of random boundaries connectivity, Figure 37.

4.5.3 Strain Anneal Long Time Anneal Experiments

Experiments outlined in the following section will analyse the change in GBCD by increasing the time of anneal from 10minutes to 168 hours. Detailed thermo-mechanical treatments can be seen in the experimental section, Table 15, which includes a small strain followed by a long period of anneal.

4.5.3.1 One-step of 3% strain at 700°C

It was shown in [9] that a two – stage low strain – anneal treatment generates similar results as to one – step processing for pure nickel. No significant increase in special boundaries was observed when second stage strain annealing was imparted. Therefore, only one – step low strain (tension) – anneal treatment were processed and analysed in the thesis.

A relatively low temperature of 700°C has chosen was to induce local rearrangement of grain boundaries rather than rapid grain growth during heat-treatment. This is to avoid a fast boundary migration rate, which does not nucleate twins so readily. The sample annealed for 0.167 hour (10 minute) is considered as the initial or the starting point of the graph. Figure 50 presents the results of fraction of special boundaries as the time of annealing increases.

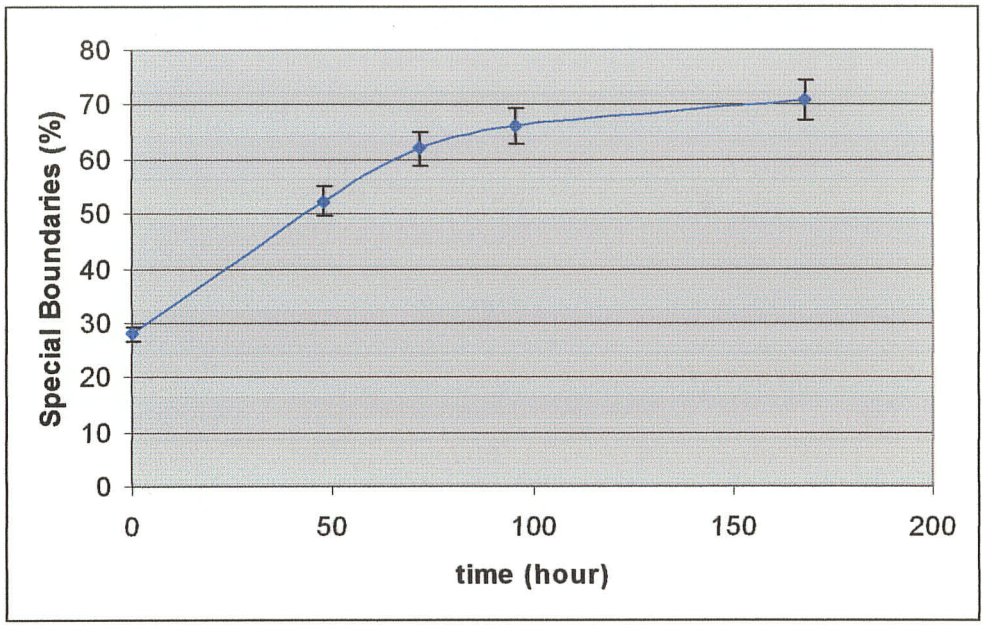

Figure 50: Graph of samples processed at 1 step 3% strain annealed at 700°C for up to 168 hours

As the annealing time increased from 10 minutes to 72 hours, in Figure 50, the relationship between special boundaries and annealing time is almost linear. The proportion of special boundaries increased to 62%, more than twice as much as the sample annealed for 10 minutes. With an additional 24 hours of annealing, the rate of increase in special boundaries slowed down, up to 66% for 96 hours. Further increase of

special boundaries up to 70.8% was observed when the annealing reached 168 hours. From the shape of the graph in Figure 49, it is likely that longer annealing treatments, beyond 168 hours would not have much effect on the total special boundaries proportion. The high fraction of special boundaries recorded showed similar results to Randle's values [19], with an extended recovery process likely being responsible for the progress of increasing special boundaries with time and minimal grain growth.

Optimization of the microstructure cannot solely base on increased fractions of special boundaries, the break-up connectivity of random boundary network should also be considered. The break-up of the random boundary network as a function of increased time of annealing in Figure 50, could be seen from the OIM maps shown in Figure 51.

(a) Grain size = 31μm

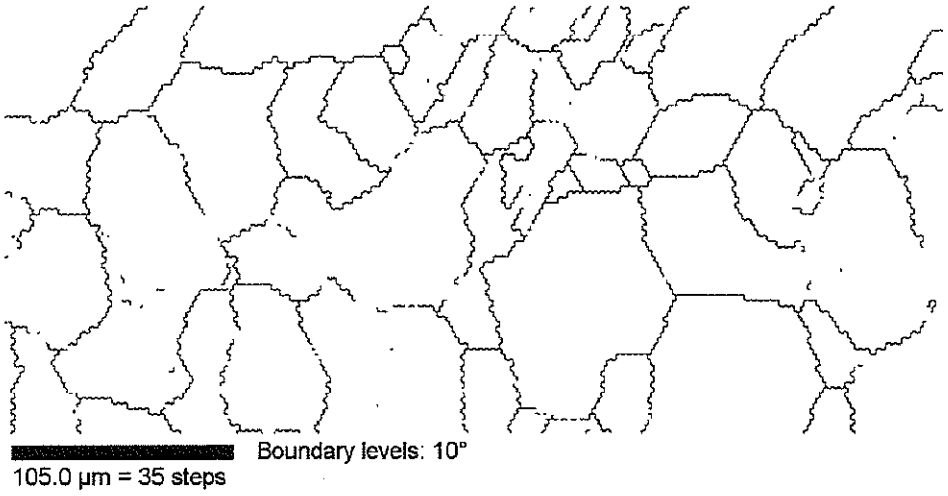

(b) Grain size = 60μm

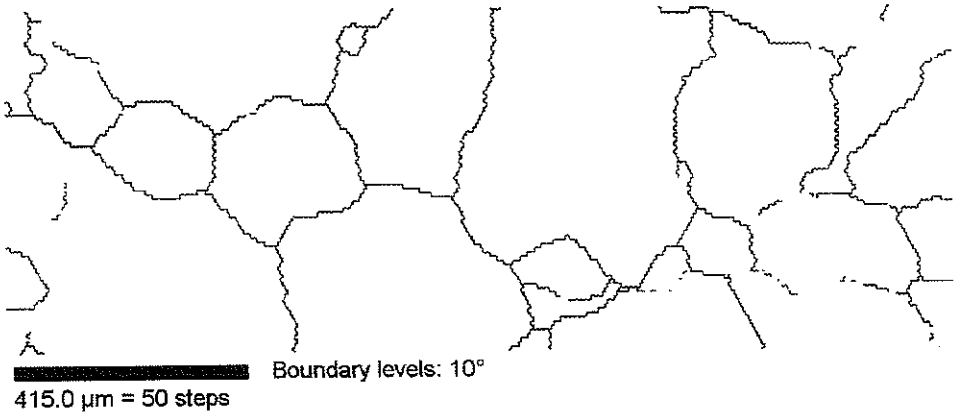

(c) Grain size = 58μm

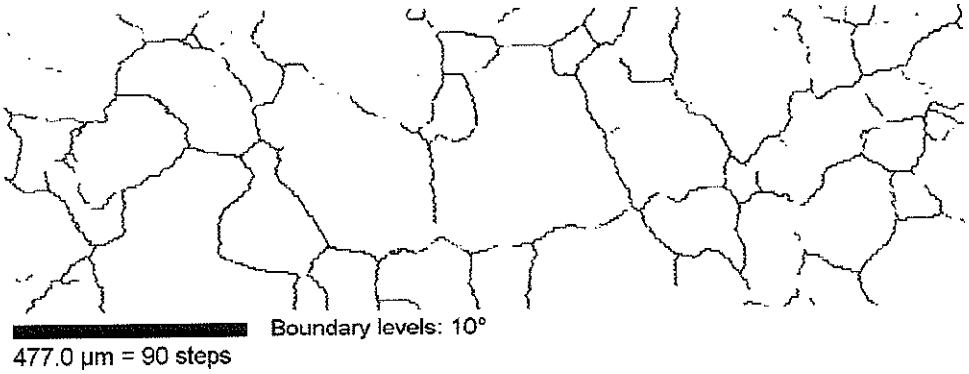

(d) Grain size = 69μm

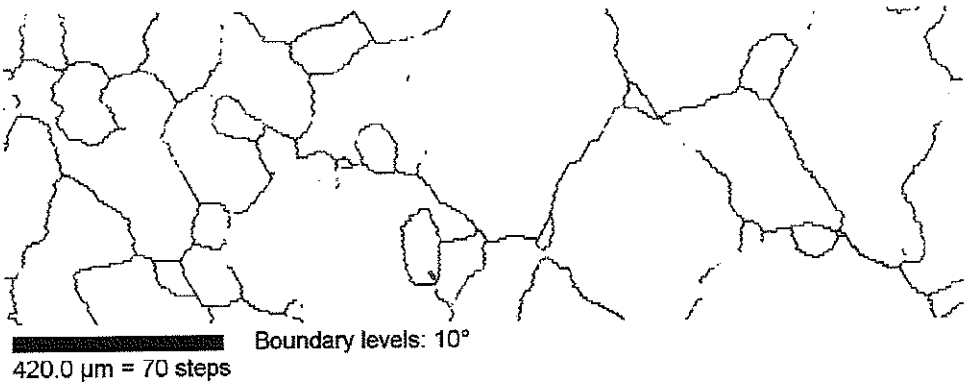

(e) Grain size = 74μm

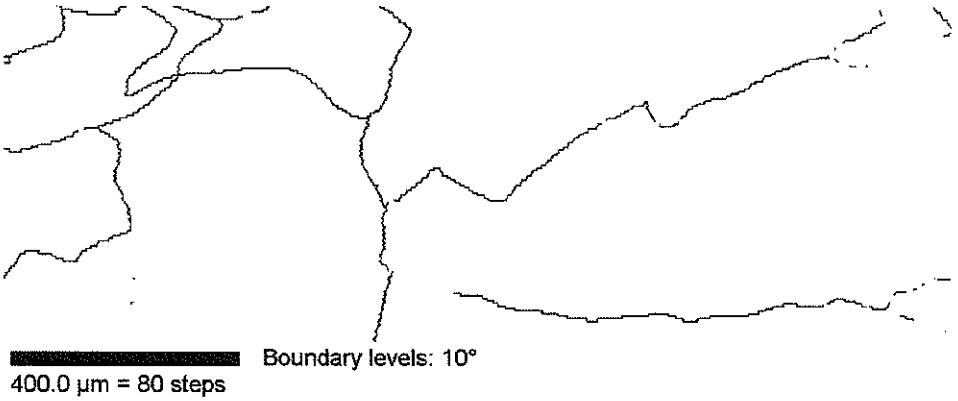

Figure 51: The network of random boundaries in the microstructure of 1 step – 3% strain annealed at 700°C for (a) 0.167hr, (b) 48hr, (c) 72hr, (d) 96hr, and (e) 168hr

Only the random boundary network is shown in Figure 51. Special grain boundaries were excluded from these OIM maps and it should not be confused with the overall grain size. The entire grain boundary network maps with special boundaries can be seen in the Appendix A4. The first map {Fig. 51(a)} shows the microstructure in the 0.167hr or 10min. annealed sample, which it is apparent that high connectivity of the random boundaries was extended throughout the imaged area. The next four maps {Fig. 51(b) – (e)} shows continuous improvement in the break-up of the random boundary network, as the annealing time increased with increasing special boundaries, reducing random high angle boundaries.

Figure 52 shows the distribution of Σ values for extended annealing time:

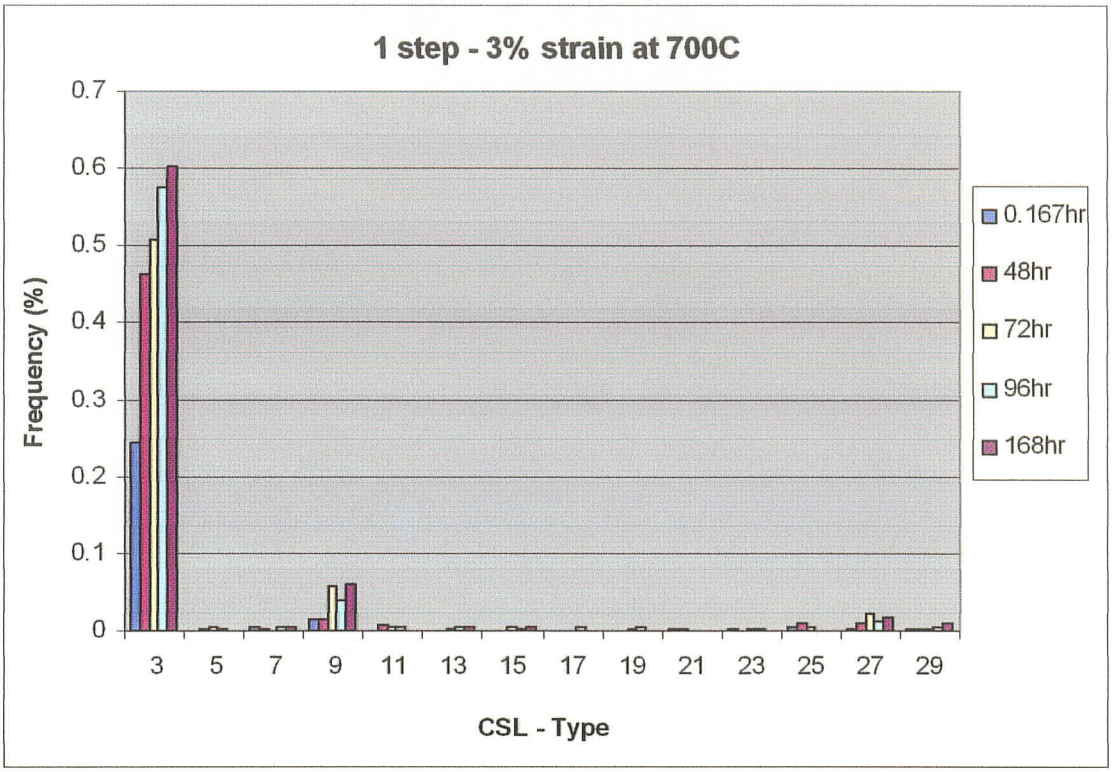

Figure 52: Distribution of CSL, $3 \leq \Sigma \leq 29$ boundaries for 1 step – 3% strain annealed at 700°C

The CSL distributions shows that as the total special boundaries increases for each sample, $\Sigma 3$ twin boundaries also increase, along with $\Sigma 3^n$ twin variants by a smaller proportion. Large percentage of $\Sigma 3$ boundaries were characterized, in the range of 45% - 60%, an increase of 23% to 64% $\Sigma 3$ boundaries compared to the 10 minute annealed sample with increasing annealing time; also an increase of ~5% in $\Sigma 9$ boundaries beyond 48 hours of annealing occurred. A lesser increase of special boundaries for $\Sigma 27$ occurred (~2%), while other low-Σ boundaries between $3 \leq \Sigma \leq 29$ had minimal contributions. Generation of new twins as annealing time increased support the generation of $\Sigma 3$ grain boundary model in [9], which by extending the annealing time to 168 hours provided

sufficient time for nucleation of twins in the wake of moving boundaries when annealed at 700°C.

4.5.3.2 One-step of 6% strain annealed at 700°C

Higher deformation (6% strain), annealed at 700°C experiments were also processed and analysed. Special boundaries proportions are plotted in Figure 53.

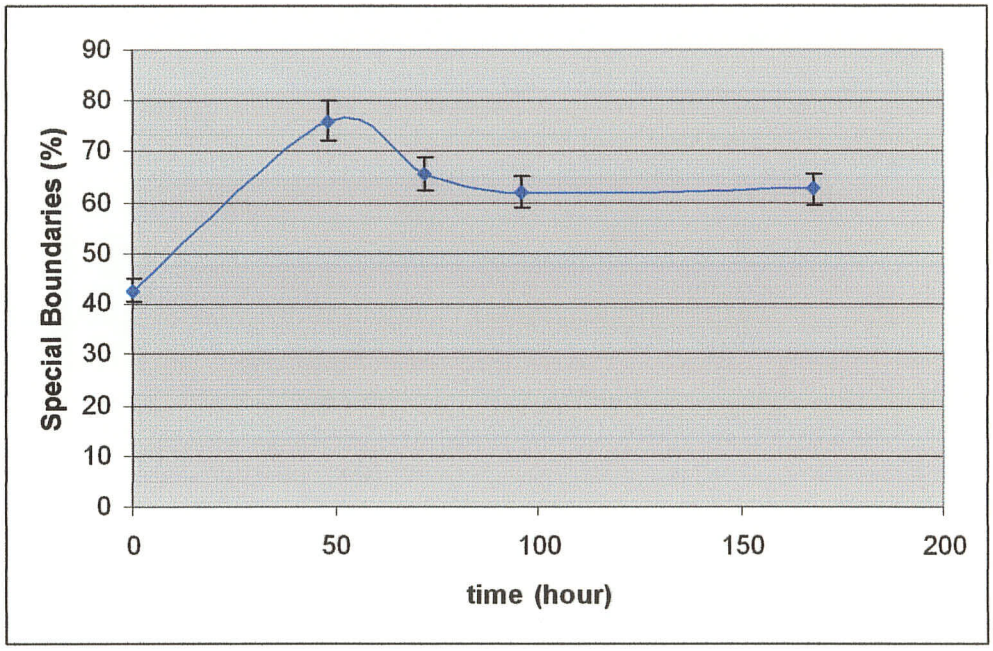

Figure 53: Graphical representation of special boundaries processed with 1 step 6% strain annealed at 700°C for 168 hours

The relationship between special boundaries and time behaved much differently in Figure 53 compared to samples processed in Figure 50. The increased in special boundary fractions for 1 step – 6% strain sample increased to 76% with 48 hours of heat-treatment at 700°C. Further annealing beyond 48 hours resulted drop in special

boundaries proportion. A negative slope can be observed from the 48 hours to 96 hours of annealing and then the curve levels off with constant Σ_{sp} values with heat-treatments beyond 96 hours.

Prolonged exposure of annealing at 700°C beyond 48 hours exerted deleterious effect in reducing the frequency of special grain boundaries, by promoting extraneous grain growth from 48 hours to 72 hours of anneal, shown in Figure 54. Then the rate of increase in grain size slows down as annealing continues after the 72 hours of anneal. Grain size measurements of samples, 1 step of 3% strain and 1 step of 6% strain annealed at 700°C for an extended period of time are plotted in Figure 54.

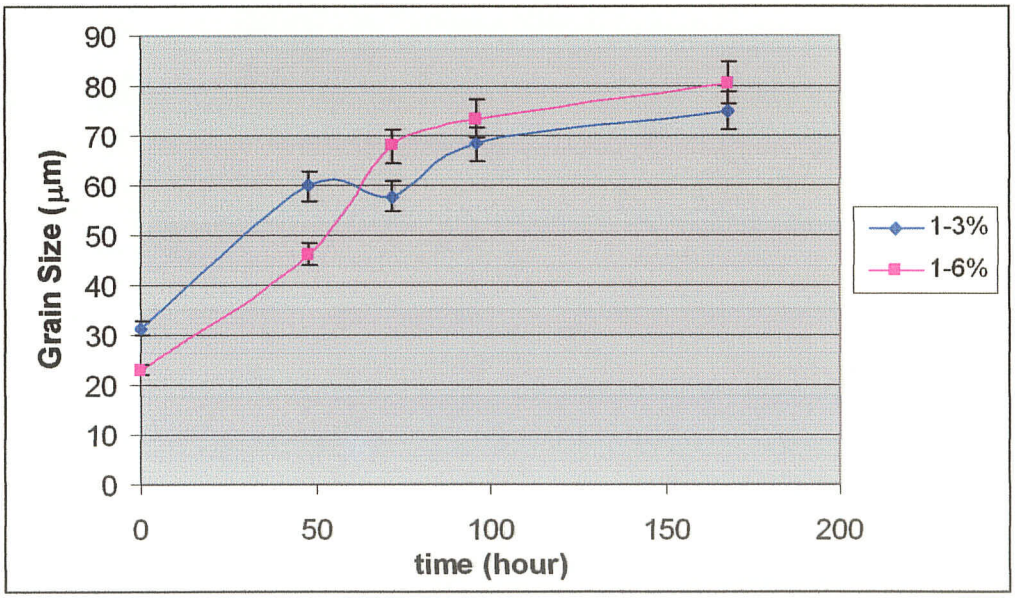

Figure 54: Grain size measurements of 1 step 3% strain and 1 step of 6% strain annealed at 700°C for an extended period of time

It was expected that grain size would increase during early stages of annealing, followed by grain boundary migration and grain rotation, forming more annealing twins

as the time of annealing increases. 1 step of 3% strain represented by 1-3% in Figure 54 shows a linear increase in grain size as the annealing time reached 48 hours. As the annealing time progresses beyond 48 hours, the rate of increase in grain size slows down, as well as the slow increase in special boundaries shown in Figure 50.

The sample 1-6% (1 step of 6% strain) annealed up to 48 hours has a high percentage of special boundaries at 76.1% and maintained a relatively small grain size of 46μm. Grain growth continued to increase up to 72 hours of annealing, then the rate of grain growth slows down. This is different than the 1-3% sample as the rate of grain growth slowed down shortly after 48 hours of annealing. It is believed that the drop in special boundaries shown in Figure 53 as time increased occurred due to the fast rate of grain growth beyond the 48 hour anneal. As the rate of grain growth slows down, the drop in the proportion of special boundaries was also reduced, indicated by the flatten portion of the curve in Figure 53, beyond the annealing time of 72 hours. This shows that the rate of grain growth also has great influence to the formation of special boundaries as well as the grain size.

OIM maps of grain boundary network and random boundary network can be seen in the Appendix A5. It can be observe from A5 (f)-(j), the random boundary network of A5(g), 1 step of 6% strain at 48 hours gave the highest proportion of low-Σ boundaries at triple junctions, contributing to the break-up of the random boundary connectivity. As expected, higher random boundary connectivity was observed as the fraction of special boundaries decreased (samples with an annealing time beyond 48hours).

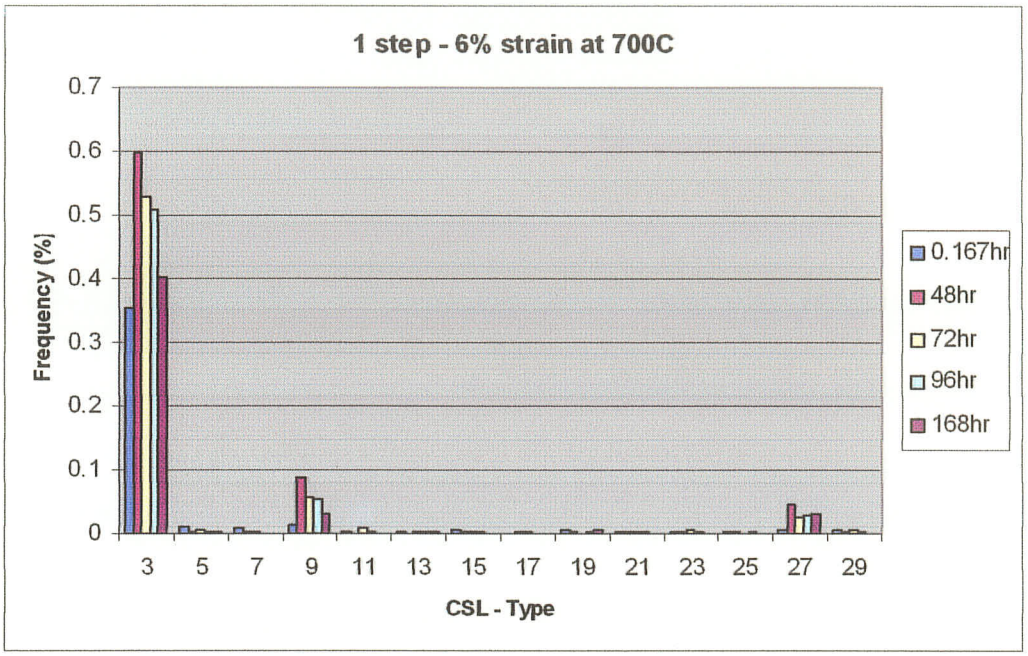

Figure 55: CSL boundaries distribution of 1 step 6% strain annealed at 700°C for 168 hours, $3 \leq \Sigma \leq 29$ boundaries

Distributions of Σ boundaries for 1 step – 6% strain annealed at 700°C are shown in Figure 55. Again, the $\Sigma 3$ twin boundaries contain the largest proportion of special boundaries, followed by $\Sigma 9$ and $\Sigma 27$, where $\Sigma 3$ twin boundary and $\Sigma 3^n$ twin related boundaries are directly proportional to the special boundaries percentage. As the total special boundaries decreased with the time of anneal (Fig. 53), the fraction of $\Sigma 3$ and $\Sigma 3^n$ boundaries also decreased.

High fractions of special boundaries have been achieved when 3% strain annealed at 700°C for 168 hours (Σ_{sp} = 70.8%) and 6% annealed at 700°C for 48hours (Σ_{sp} = 76.1%). Both of these two samples are comparable to the results of multiple steps strain annealed at 900°C, where a high fraction of special boundaries and low random boundary

connectivity were observed. Minimizing grain size has been shown in the literature to be beneficial to grain boundary engineered materials. The only sample that has a small grain size while maintaining a high proportion of special boundaries (Σ_{sp} > 70%) is the 1 step of 6% strain annealed at 700°C for 48 hours sample. This sample had a grain size of 46μm, whereas other samples with Σ_{sp} > 70% have a grain size of 60μm of higher.

4.5.3.3 One Step Anneal at 800°C

Percentage special boundaries of one step 3% and 6% strain, annealed at 800°C up to 168 hours, are shown in Figure 56.

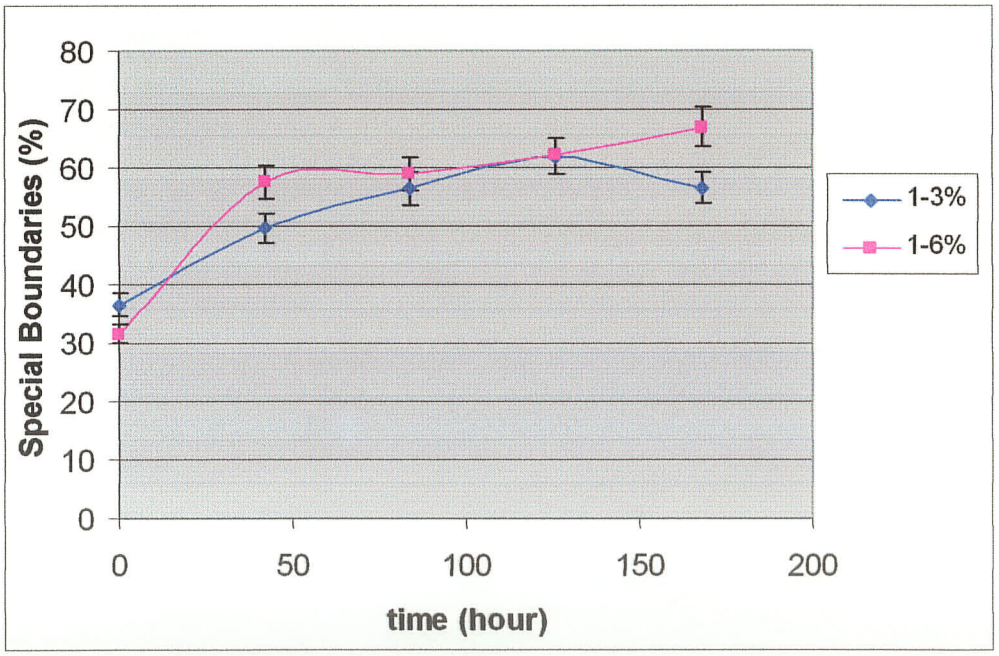

Figure 56: Results of special boundaries of increased annealing time up to 168 hours for 1 step 3% strain and 1 step 6% strain annealed at 800°C

In Figure 56, the curve 1-3% represent samples strained with one step of 3% and 1-6% signify one step 6% strain. Results obtained for both sets of samples annealed at 800°C follow a similar pattern; close to a linear increased in special boundaries with time during early stages of anneal up to 48hours, then the rate of increase in special boundaries slows down as the time of annealing increases. Special boundaries fraction of sample 1 step -6% strain, is a little higher than the 1 step - 3% strain sample during initial and latter stages of the long time anneal. It is possible that there were some scatter in $\sum_{sp}$ during data collection, which is indicated by the standard deviation of ±3%. Both samples annealed up to 168 hours and beyond are expected to maintain a $\sum_{sp} \sim 60\%$.

OIM maps of grain boundary network and random boundary network for both 1-3% and 1-6% samples annealed at 800°C can be seen in Appendix A6 and A7. Random boundary network in Figures A6(f) – (j) and Figures A7(f) – (j) shows that the random boundary connectivity decreases as the total fraction of special boundaries increases. Even though the fraction of special boundaries reached over 60%, it was not enough to influence the clusters of random boundaries that existed. Samples with $\sum_{sp} > 70\%$ observed in Figures {34-37, A5(g)} shows a much lower random boundary connectivity map with higher probabilities of finding secured triple junctions of at least two low CSL boundaries.

Grain size of both sets of samples annealed at 800°C were measured and plotted in Figure 57. The grain size of 1-6% strain sample was much larger than the 1-3% strain sample at 10 minutes of annealing due to a higher deformation strain applied initially.

Samples with small deformation normally do not initiate grain growth as quick as larger deformed samples, when insufficient deformation energy was stored and released during heat-treatment. Continuous increased in grain size was observed from 10 minutes to 48 hours of annealing for both samples, especially the 1-3% strained sample with grain size up to 64μm. Further annealing showed almost no effects on the grain size as the values were between 60-70μm for both sets of samples, with error bars indicated for upper and lower limits.

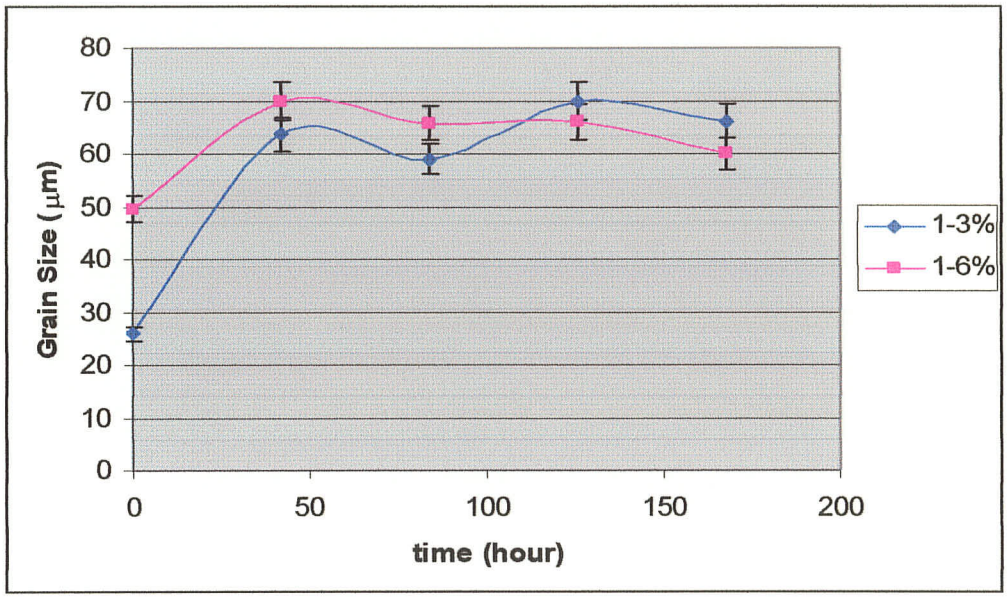

Figure 57: Grain size measurements of 1 step 3% strain and 1 step of 6% strain annealed at 800°C with increased annealing time

The distributions of CSL boundaries are shown in Figure 58(a) and (b). A consistent increase in Σ3 boundary fractions along with Σ9s and Σ27s were observed with an increase in special boundary fraction, similar to all the samples shown previously.

(a)

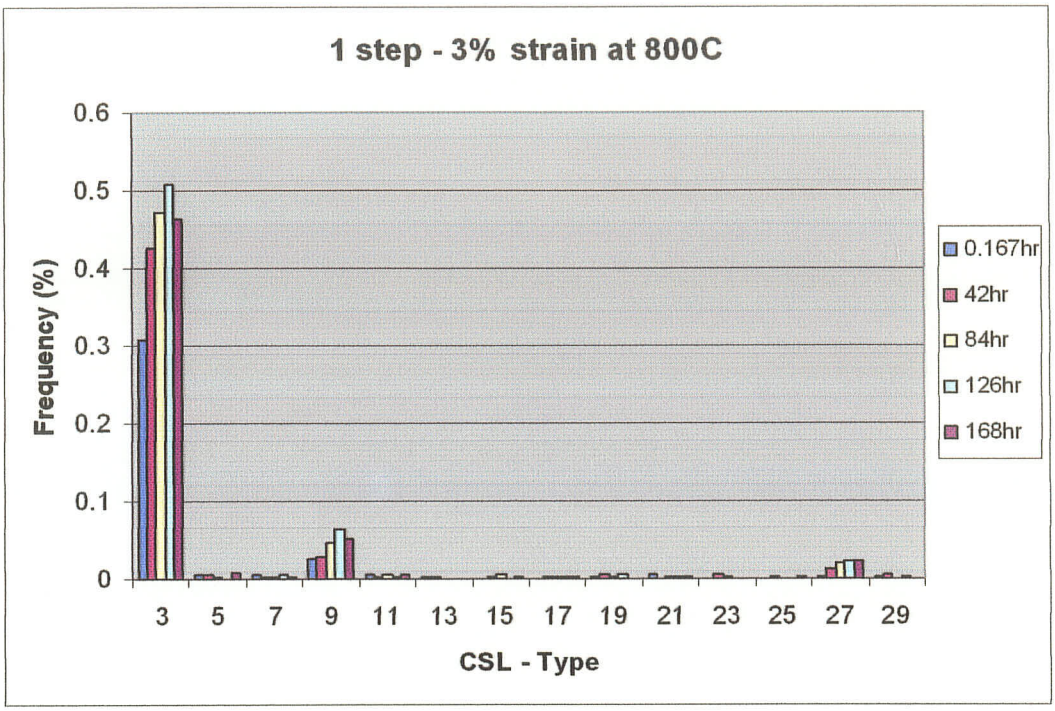

(b)

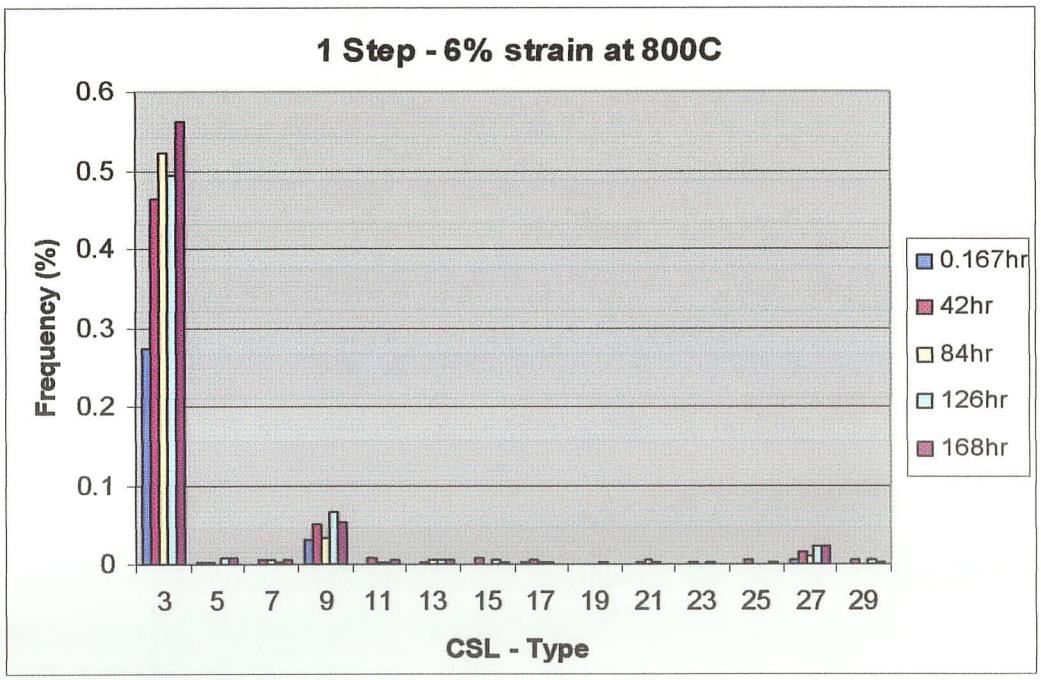

Figure 58: Distribution of CSL boundaries, $3 \leq \sum \leq 29$, for (a) 1 step – 3% strain and (b) 1 step – 6% strain annealed at 800°C

4.5.3.4 Fine Tuning at $\Sigma 3^n$ Boundaries

The main effect of small percentage of pre-strain (3%-6%) and extended time of annealing is likely fine tuning at grain boundaries [19] due to local lattice rotations near the boundary, probably accompanied by grain boundary plane reorientation.. The CSL categorization were further analysed by plotting the distribution of special boundaries at various misorientation angles as the time of annealing increased as shown in Figure 59.

(a)

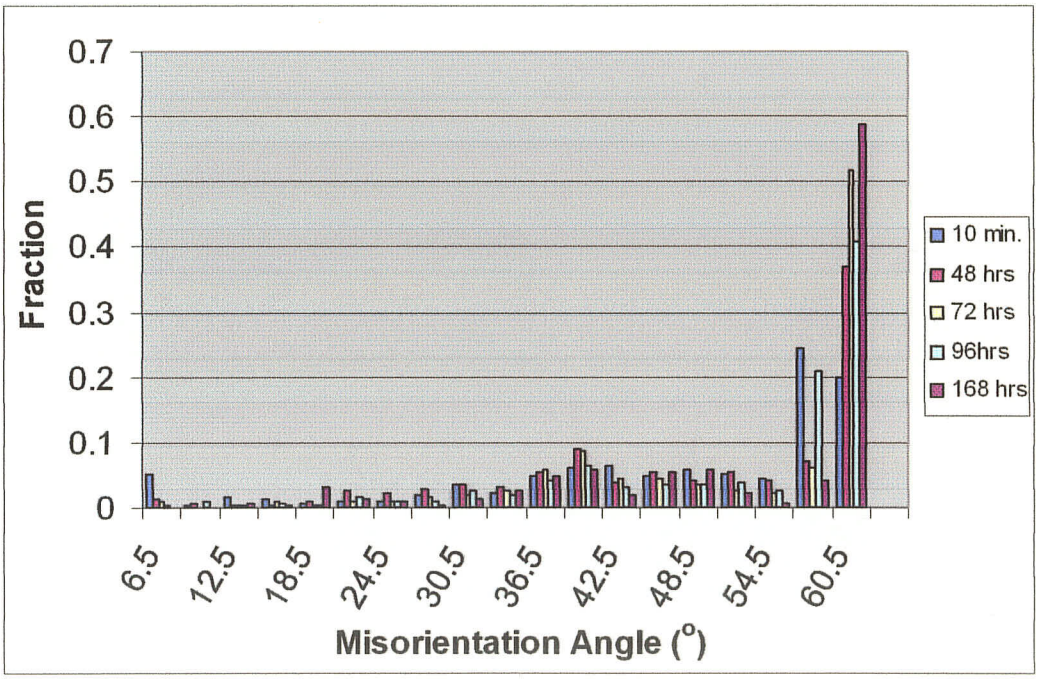

(b)

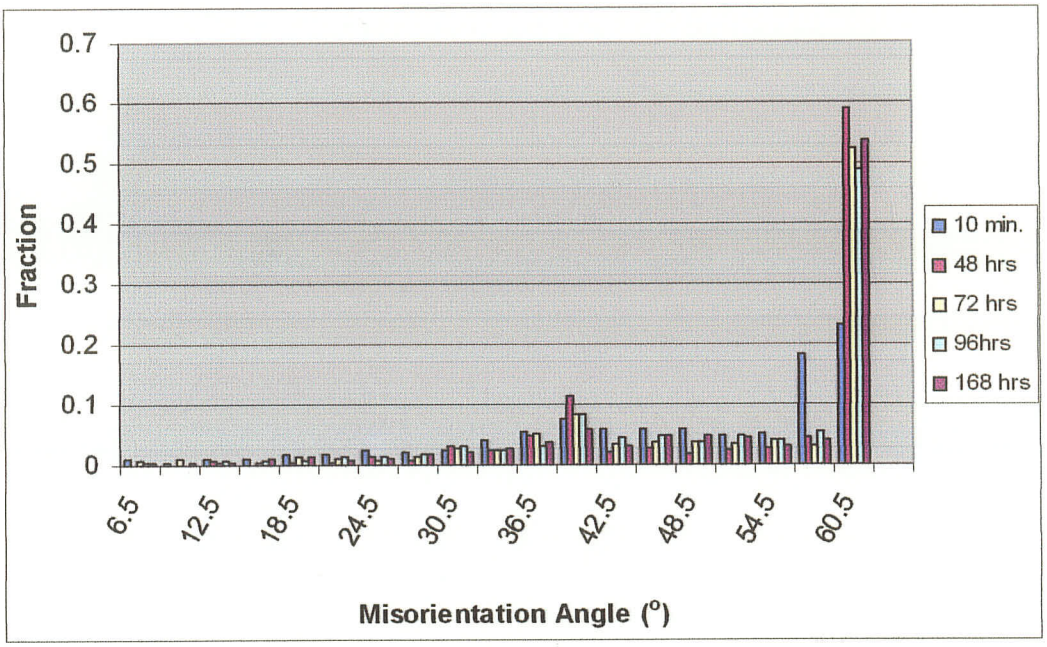
0.7
0.6
0.5
0.4
0.3
0.2
0.1
0
Fraction
6.5
12.5
18.5
24.5
30.5
36.5
42.5
48.5
54.5
60.5
Misorientation Angle (°)
10 min.
48 hrs
72 hrs
96hrs
168 hrs

(c)

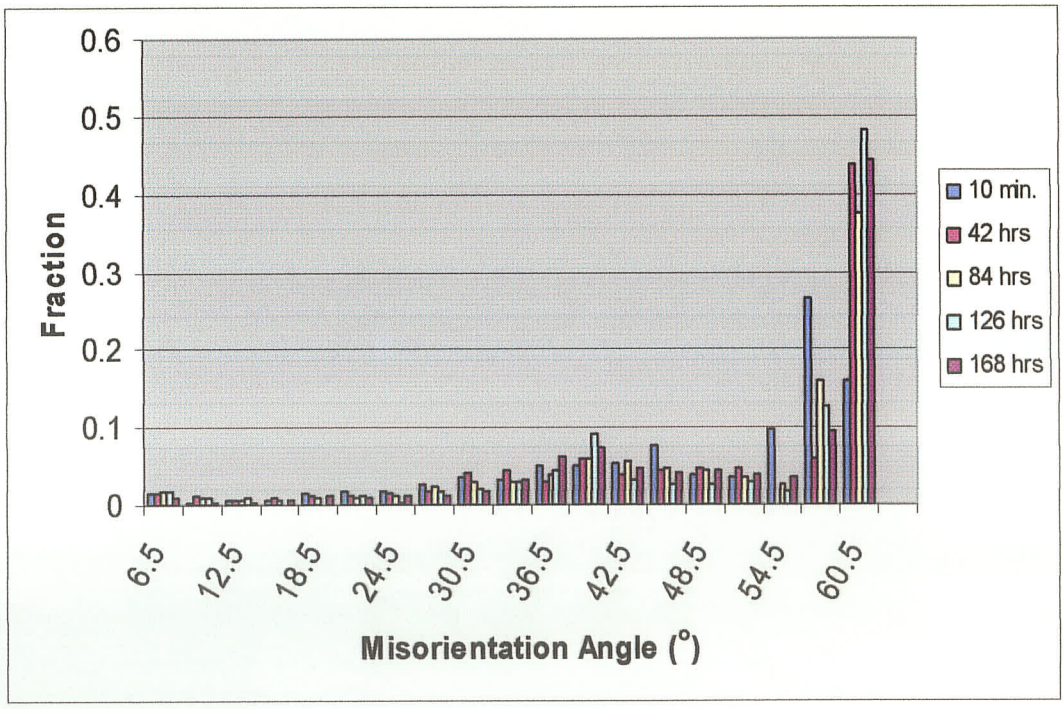
0.6
0.5
0.4
0.3
0.2
0.1
0
Fraction
6.5
12.5
18.5
24.5
30.5
36.5
42.5
48.5
54.5
60.5
Misorientation Angle (°)
10 min.
42 hrs
84 hrs
126 hrs
168 hrs

(d)

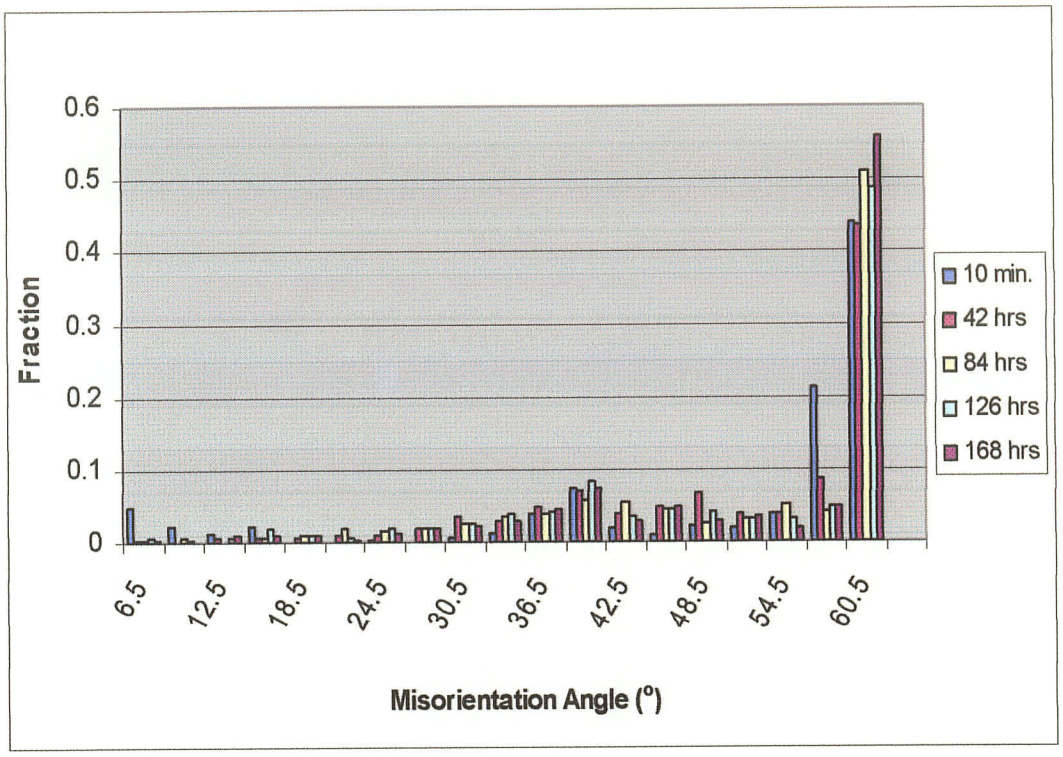

Figure 59: Graphical representation of the distribution of special boundaries at various misorientation angles processed at (a) 1 step of 3% strain annealed at 700°C, (b) 1 step of 6% strain annealed at 700°C, (c) 1 step of 3% strain annealed at 800°C, (d) 1 step of 6% strain annealed at 800°C

A large fraction of special boundaries were found at the misorientation angle of 60.5° for all four graphs in Figure 59. It was seen in previous sections that a majority of low-Σ boundaries were made up of Σ3 twin boundaries. It is reasonable to believe that the special boundaries found on the 60.5° misorientation angle are largely Σ3 boundary types. The distinction between coherent and non-coherent (Σ3) twin boundaries has been well documented in [28], that coherent Σ3 twin boundary which lies on a 60° / {1 1 1} plane have superior properties over random boundaries. In Figure 59, a large fraction of

boundaries were found at misorientation angle ~60.5° beyond 10 minutes of annealing, where coherent twin boundaries most likely exist.

The small amount of pre-strain produces non-equilibrium extrinsic grain boundary dislocations (EGBD's), which are annihilated by climb during heat treatment [72]. Pumphrey and Gleiter [73] have also shown during annihilation of extrinsic grain boundary dislocations that grain boundary movement occurs. This has been corroborated by Sangal and Tangri [72] in 316-stainless steel pre-strained 2% and annealed at 600°C, where grain boundary movement was also observed. Thus it is energetically favourable during annealing for the EGBD's to climb to towards triple points and annihilate, reducing the grain boundary energy. This is likely what happens during Randle's fine-tuning [19] accompanied by grain rotation and grain boundary plane reorientation.

4.5.4 Statistical Analysis of Selected Experiments

The results of these selected experiments were analysed by Dr. Ken Mount in the Department of Statistics. The objective of the statistical analyses were to show that there were interactions between the dependent valuable, $\Sigma_{sp,}$ and independent variables strain, temperature and the number of cycles. Experiments analysed were followed by the multiple step strain-anneal processing results found in section 4.5.2. Individual plots of independent valuables against Σ_{sp} are shown in Figure 60 and Figure 61 are plots made with pairs of variables against $\Sigma_{sp.}$

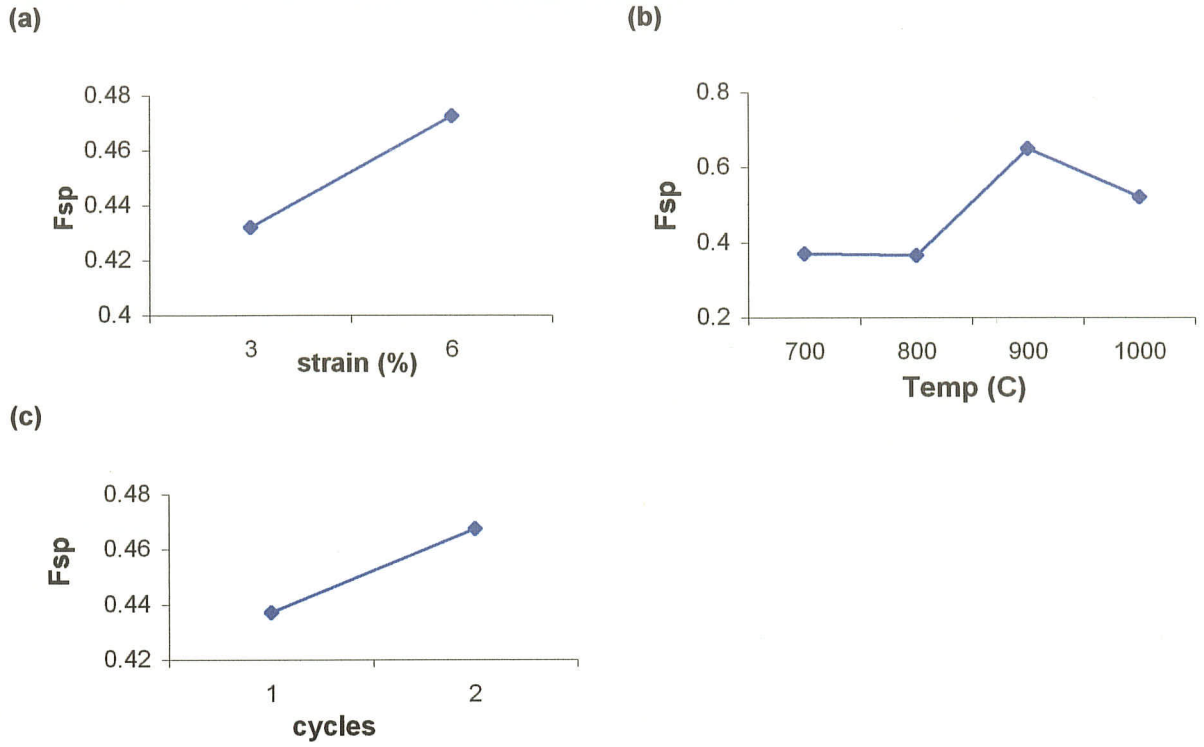

Figure 60: Main effect plots for (a) strain, (b) temperature and (c) number of cycles

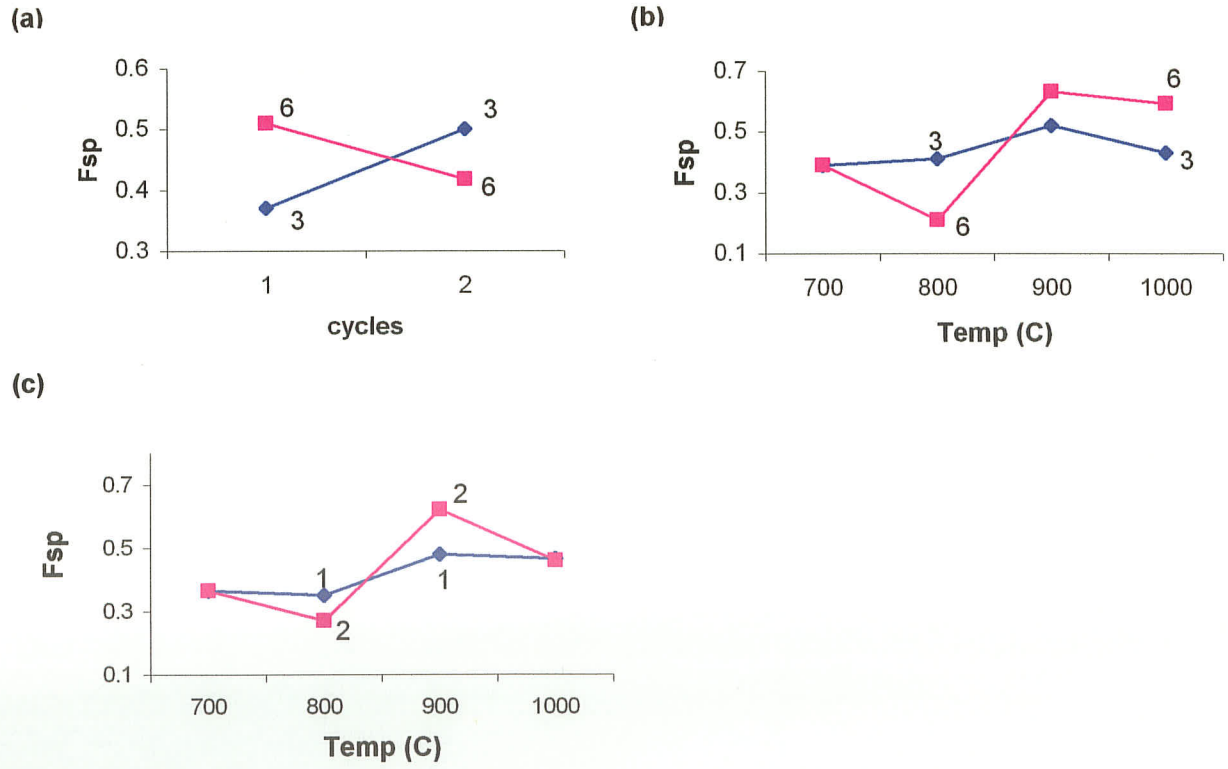

Figure 60: Variable effect combinations (a) strain per cycle and number of cycles, (b) strain per cycle and temperature, (c) number of cycles and temperature

The main effect plots displayed in Figures 60(a) and (c) showed that as pre-strain and number of cycles increases, the fraction of special boundaries increases. The temperature plot in Figure 60(b) showed that as temperature increases, the fraction of special boundaries increases up to 900°C, than decreases when it reached 1000°C.

Plots in Figure 61 showed that there are interactions among the three variables as a cross over of lines occurred; therefore logistical regression analyses were performed. Equations were developed to relate the fraction of special boundary and the three variables. The relationship for temperatures 700°C and 800°C following the strain sequence outlined in section 4.5.2 shows a model of the type:

$$\ln [F_{sp}/(1- F_{sp})] = -7.95 + 1.66\epsilon + 0.0075T + 1.878C - 0.0017\,\epsilon*T - 0.358\epsilon*C - 0.0005T*C$$

The relationship for temperatures 900°C and 1000°C following the strain sequence outlined in section 4.5.2 shows a model of the type:

$$\ln [F_{sp}/(1- F_{sp})] = -6.05 + 0.328\epsilon + 0.0033T + 7.91C + 0.0003\,\epsilon*T - 0.244\epsilon*C - 0.0068T*C$$

Where F_{sp} is the fraction of special boundaries, ϵ is the strain per cycle, T is the annealing temperature, and C is the number of cycles. The logarithm was used to ensure the value for F_{sp} is between 0 and 1. The relationships above were significant at greater than 99% level of confidence, but the goodness of fit value for these models was poor. The calculated goodness of fit value for the 700°C and 800°C model was 14.8, and the 900°C

and 1000°C model was 269.3 when an acceptable value is 2 to 2.5. This implies that this model will not provide the proper correlation between F_{sp} and the three variables.

It seems that in the 800°C / 900°C temperature range, metallurgical effects such as annihilation of EGBD's occurs, along with grain boundary movement and local fine tuning of grain boundaries. This analysis suggests that future research should concentrate in the range of 800°C - 900°C, along with duplicate tests.

4.5.5 Summary of Thermomechanical Treatment Results

The focus of this project was to manipulate the strain – anneal technique to increase the proportion of special grain boundaries, where $\Sigma \leq 29$. The as-received material recorded a special boundaries percentage of 36.5%.

4.5.5.1 Single Step Strain-anneal Treatments

The as-received Σ_{sp} value is 36.5%.

Table 23: Special boundary values due to single-step strain-anneal processing

	Temperature			
Strain	**500°C**	**700°C**	**800°C**	**900°C**
3%	32.3%	25.3%	36.6%	37%
6%	29.2%	41.5%	31.6%	74.7%
12%	29.6%	29.5%	33.1%	58.1%

4.5.5.2 Multiple Steps Strain-anneal Treatments

Table 24: Special boundary values due to multiple steps strain-anneal processing

	Temperature				
Strain	**500°C**	**700°C**	**800°C**	**900°C**	**1000°C**
2 steps of 3%	31.5%	42.3%	42.6%	75%	39.6%
2 steps of 6%	27.6%	24.5%	21.2%	75.6%	60.9%
4 steps of 3%	22.1%	25.6%	23.3%	76.8%	54.8%

4.5.5.3 Long Period of Anneal Treatments

Table 25: Special boundary values due to an extended time of annealing processed at 700°C

	700°C	700°C
Time of Anneal	**1 step of 3% strain**	**1 step of 6% strain**
10 minutes	29.5%	41.5%
48 hours	53.2%	76.1%
72 hours	62%	65.7%
96 hours	66.1%	62%
168 hours	70%	62.7%

Table 26: Special boundary values due to an extended time of annealing processed at 800°C

	800°C	800°C
Time of Anneal	**1 step of 3% strain**	**1 step of 6% strain**
10 minutes	36.6%	31.6%
42 hours	49.8%	57.6%
84 hours	56.5%	59%
126 hours	61.9%	62%
168 hours	56.6%	66.9%

Single step and multiple steps strain-anneal treatment showed almost no improvement in special grain boundary fractions at high strain (12%) and low annealing temperatures (≤ 800°C). One-step strain and anneal for an extended period of time

showed significant improvements in special boundaries, with more than 70% special boundaries formed, similar to the multiple steps strain-anneal processing at 900°C. This indicates that the annealing temperature alone may not be the most important processing parameter.

The control of the annealing time and the amount of deformation also has significant impacts on the grain boundary characteristic distributions. Appropriate combinations of the three processing parameters (strain, temperature and time) may very well generate a high proportion of special grain boundaries for $\Sigma \leq 29$, as well as the distribution of random boundary network.

Chapter 5

CONCLUSION

Thermomechanical Processing of commercially pure nickel or Ni-200 (99.5% pure) has been successfully used to increase the proportion of special low-$\sum$ boundaries over the as-received material. Processing included low tensile strains of 3% to 12%, single step or multiple steps, annealed between 500°C and 1000°C for 10 minutes. Time extended annealing treatments were also performed by deforming samples with 3% and 6% strain, followed by annealing temperatures of 700°C and 800°C for up to 168 hours.

1) The as-received material had a fine grain size of 26μm and an equiaxed microstructure. The proportion of special grain boundaries measured was 36.5%, when $3 \leq \sum \leq 29$ were considered as special boundaries. $\sum 3$ twin boundary was analysed to be the major contribution to the total fraction of special boundaries at 26.9%, approximately 75% of the total special boundary content.

2) Annealing temperature is one of the major factors in thermomechanical processing to control. For a short annealing period of 10 minutes at 900°C, over 75% fraction of special grain boundaries was achieved for multiple steps processing, with deformation of 6% strain and 12% strain applied. Recrystallization may have occurred and enhanced the formation of annealing twins, leading to $\sum_{sp}$ values up to 75% or higher. Minimal enhancement of special boundaries occurred for multiple steps processed samples annealed at

temperatures 800°C or less, when grain boundary recovery and migration likely occurred to allow local rearrangement of grain boundaries. For 1000°C annealed samples, excessive grain growth occurred and the fraction of $\sum$ boundaries was reduced below 900°C annealed samples.

3) Single step processing of 6% strain sample, annealed at 900°C also attained a high proportion of special boundaries at 74.7%. Samples strained at 3%, 9% and 12% and annealed at 900°C showed a lower special boundaries percentage of less than 60%. Single step processing of 3% to 12% strain, annealed at 800°C or below showed almost no improvement in special boundary fraction being similar to the as-received material at 36.5%.

4) As the annealing temperature increases up to 900°C, the grain size consequently increased. The increase in special boundary fraction was the result of multiple twinning during grain growth, where a high proportion of $\sum 3$ twin boundaries and $\sum 3^n$ twin related boundaries were generated. Twinning is considered an important part of grain growth as the proportion of random boundaries is reduced, the fraction of low-$\sum$ boundaries increases.

5) High clusters of random boundary network were found for samples with low percentage of special boundaries. The connectivity among random and special grain boundaries was broken-up as higher probability of special boundaries occurred. This results in fragmentation of the network of random boundaries to

provide a microstructure with secure triple junctions. The sample processed at 4 steps of 3% strain annealed at 900°C for 10minutes has the highest fraction of special boundaries at 76.8% and one of the least amounts of random boundary topology found at triple junctions.

6) Low temperature annealing treatments (i.e. 700°C and 800°C) after low pre-strains of 3% and 6% for extended periods of time also produced improvements to the grain boundary population, by increasing the total fraction of special boundaries. The sample processed with 1 step of 3% strain annealed at 700°C for 168 hours generated 70.8% special boundaries, and the process of 1 step of 6% strain annealed at 700°C for 48 hours produced 76% special boundaries.

7) Fine tuning at grain boundaries have been observed for long period annealed samples, probably due to sufficient amount of time for local lattice rotations near the boundary, accompanied by grain boundary plane reorientation. This favours $\sum 3$ twin boundaries to rearrange (fine tuning) their misorientation angle near 60°, where coherent twin boundaries exist.

8) Equations were developed for F_{sp} as a function of the three variables: strain, temperature and number of cycles. The two equations found are not a good predictor of the F_{sp} from the data collected, due to a large value of fit found. A fit value of 14.8 and 269.3 was found for temperature ranges of 700°C and 800°C, and 900°C and 1000°C respectively, when an acceptable fit value is 2 - 2.5.

Chapter 6

RECOMMENDATIONS

1) To determine the effects of changing the rate of heat energy extraction quenching medium from air to water have on the GBCD. By increasing the severity of quench, possible trapping of minor elements such as carbon, sulphur and oxygen at grain boundaries may affect the structure and mechanical properties of the sample.

2) To test for corrosion resistance of special boundaries enhanced samples with $\sum_{sp}$>70%. It was found in [8] that the increased in special boundaries frequency of Alloy-600 in excess of 70% recorded a near complete immunity against stress corrosion cracking.

3) Samples with $\sum_{sp}$>70% have been reached with grain size measurements of 46μm and 80μm. Difference in grain size may affect mechanical properties and performance during service, mechanical testing such as creep and intergranular cracking can be analysed to determine the effects of coarse and fine grain size may have on the material.

4) Implement successful processing routes to commercial nickel alloys to possibly improve its mechanical properties against intergraular degradations during service.

5) Increase the number of steps of processing long period anneals to possibly improve fine tuning of $\sum 3$ twin boundaries to become near coherent twin boundary orientation.

REFERENCES

[1] WATANABE, T., **"An Approach to Grain Boundary Design for Strong and Ductile Polycrystals"**, Research Mechanica 11, 1984, pp. 47-84.

[2] Reitz, W.E., **"Improving Materials Properties and Performance through Grain Boundary Engineering"**, JOM, February 1998, pp.39

[3] KRONBERG, M.L., WILSON, F.H., **"Secondary Recrystallization in Copper"**, Metals Transaction, 1949, Vol. 185, pp.501-514.

[4] PALUMBO, G., LEHOCKEY, E.M. and LIN, P., **"Applications for Grain Boundary Engineered Materials"**, JOM, February 1998, pp.40-43

[5] WATANABE, T., **"The Potential for Grain Boundary Design in Materials Development"**, Materials Science Forum, 1988, Vol. 11, pp. 284-303.

[6] WATANABE, T., **"Grain Boundary Design and Control for High Temperature Materials"**, Materials Science and Engineering A166, 1993, pp. 11-28.

[7] CRAWFORD, DOUGLAS C. and WAS, GARY S., **"The Role of Grain Boundary Misorientation in Intergranular Cracking of Ni-16Cr-9Fe in 360°C Argon and High-Purity Water"**, Metallurgical Transactions A, April 1992, Vol. 23A, pp.1195-1205.

[8] WATANABE, T., **"Grain Boundary Design for Desirable Mechanical Properties"**, Journal de Physique (colloque C5 - 509, supplement au n*10, Tome 49, Octobre 1988), pp.507-516

[9] RANDLE, V., **"The Effects of Thermomechanical Processing on Interfacial Crystallography in Metals"**, Materials Science Forum, 1999, Vols. 294-296, pp.51-58

[10] WAS, G.S., THAVEEPRUNGSRIPORN, V. and CRAWFORD, D.C., **"Grain Boundary Misorientation Effects on Creep and Cracking in Ni-Based Alloys"**, JOM, February 1998, pp.44-49.

[11] DIETER, G.E., "**Mechanical Metallurgy"**, McGraw-Hill Book Company, N.Y., 1986, 3rd Edition, pp.184-240.

[12] THOMSON, C.B. and RANDLE, V., **"The effects of strain annealing on grain boundaries and secure triple junctions in Nickel-200",** Chapman & Hall, pp.1909-1914, 1997

[13] MEYERS, M.A. and CHAWLA, K.K., **"Mechanical Metallurgy Principles and Applications",** Prentice-Hall Inc., U.S., 1984

[14] PALUMBO, G., AUST, K.T., **"Structure-Dependence of Intergranular Corrosion in High Purity Nickel"**, Acta Metallurgical Material, 1990, Vol. 38, No. 11, pp. 2343-2352.

[15] RANGANATHAN, S., **"On the Geometry of Coincidence-Site Lattices",** (Cambridge, England) Acta. Cryst., 1966. 21, pp.197-199

[16] RANDLE, V., **"Relationship between Coincidence Site Lattice, Boundary Plane Indices, and Boundary Energy in Nickel"**, Materials Science and Technology, 1999, Vol. 15, pp. 246-252.

[17] RANDLE, V., **"Refined Approaches to the Use of the Coincidence Site Lattice",** JOM, February 1998, pp56-59

[18] WEBSITE - http://hsc.csu.edu.au/engineering_studies

[19] THOMSON, C.B. and RANDLE, V., **"Fine Tuning at $\Sigma 3^n$ Boundaries in Nickel",** Acta Mater., 1997, Vol. 45, No.12, pp. 4909-4916.

[20] SOURMAIL, T., OPDENACKER, P., HOPKIN, G. AND BHADESHIA, H.K.D.H., **"Metals and Alloys – Annealing Twins"**, Phase Transformations and Complex Properties Research Group, 2000, www.msm.cam.ac.uk/phase-trans

[21] WEBSITE - http://www.msm.cam.ac.uk

[22] THOMSON, C.B. and RANDLE, V., **"A Study of Twinning in Nickel"**, Scripa Materialia, 1996, Vol. 35, No. 3, pp. 385-390.

[23] GINDRAUX, G., FORM, W., **"New Concepts of Annealing – Twin Formation in Face – Centered Cubic Metals",** Journal of the Institutes of Metals, 1973, Vol.101, 85-93.

[24] RANDLE, V., **"Mechanism of Twinning-Induced Grain Boundary Engineering in Low Stacking-Fault Energy Materials"**, Acta Mater., 1999, Vol. 47, Nos. 15, pp. 4187-4196.

[25] HORTON, D., THOMSON, C.B. and RANDLE, V., **"Aspects of Twinning and Grain Growth in High Purity and Commercially Pure Nickel"**, Materials Science and Engineering A203, 1995, pp. 408-414.

[26] PANDE, C.S., IMAM, M.A. and RATH, B.B., **"Study of Annealing Twins in FCC Metals and Alloys"**, Metallurgical Transactions A, Nov. 1990, Vol. 21A, pp. 2891-2896.

[27] PANDE, C.S., IMAM, M.A. and RATH, B.B., **"Nucleation and Growth of Twin Interfaces in FCC Metals and Alloys"**, Material Phys. Mech.1, 2000, pp. 61-66

[28] RANDLE, V., **"A Methodology for Grain Boundary Plane Assessment by Single-Section Trace Analysis"**, Scripta Materialia, 2001, Vol. 44, pp. 2789-2794

[29] LIM, L.C. and RAJ, R., **"On the Distribution of Σ for Grain Boundaries in Polycrystalline Nickel Prepared by Strain-Annealing Technique"**, Acta Metallurgica, 1984, Vol. 32, No. 8, pp. 1177-1181.

[30] FURLEY, J., RANDLE, V., **"Mesotextre in Annealed Nickel"**, Material Science and Technology, 1997, Vol. 7, pp.12-19

[31] WILSON, D.V. **"Controlled Directionality of Mechanical Properties in Sheet Metals"**, Review 139, Metallurgical Reviews

[32] DOHERTY, R.D., HUGHES, D.A., HUMPHREYS, F.J., JONAS, J.J., JUUL JENSEN, D., KASNER, M.E., KING, W.E., McNELLEY, T.R., McQUEEN, H.J., ROLLETT, A.D., **"Current Issues in Recrystallization: a review"**, Material Science and Engineering A, 1997, pp.219-274.

[33] WEBSITE - http://mse-p012.eng.ohio-state.edu

[34] CALLISTER, W.D., "Materials Science and Engineering an Introduction", John Wiley & Sons, Inc., 1997, 4th edition, pp. 166-171.

[35] WATANABE, T., **"The Importance of Grain Boundary Character Distribution (GBCD) to Recrystallization, Grain Growth and Texture"**, Scripta Metallurgica, 1992, Vol. 27, pp. 1497-1502.

[36] THAVEEPRUNGSRIPORN, V. and WAS, G.S. **"Grain Boundary Properties of Ni-16Cr-9Fe at 360°C"**, Scripa Materialia, 1996, Vol. 35, No. 1, pp. 1-8.

[37] WATANABE, T., **"The Impact of Grain Boundary Character Distribution on Fracture in Polycrystals"**, Materials Science and Engineering A176, 1994, pp. 39-49

[38] PALUMBO, G., **"Metal Alloys having Improved Resistance to Intergranular Stress Corrosion Cracking"**, United States Patent 5,817,193 (October 6, 1998) Filed January 17, 1997

[39] LIM, L.C., WATANABE, T., "Fracture Toughness and Brittle-Ductile Transition Controlled by Grain Boundary Charater Distribution (GBCD) in Polycrystals", Acta Metallurgical Materials, 1990, Vol.38, No. 12, pp. 2507-2516.

[40] LEHOCKEY, E.M., PALUMBO, G. and LIN, P., **"Improving the Weldability and Service Performance of Nickel- and Iron-Based Superalloys by Grain Boundary Engineering"**, Metallurgical and Materials Transactions A, December 1998, Vol. 29A, pp.3069

[41] PALUMBO, G., KING, P.J., AUST, K.T., ERB, U., LICHTENBERGER, P.C., **"Grain Boundary Design and Control for intergranular Stress – Corrosion Resistance"**, Scripta Metallurgica, 1991, Vol. 25, pp. 1775-1780.

[42] PALUMBO, G., KING, P.J., AUST, K.T., ERB, U., LICHTENBERGER, P.C., **"Grain Boundary Structure Control for intergranular Stress – Corrosion Resistance"**, Material Research Society, 1992, Vol. 238, pp. 311-316

[43] KING, W. E., and SCHWARTZ, A.J., **"Toward Optimization of the Grain Boundary Character Distribution in OFE Copper"**, Scripta Materialia, 1998, Vol. 38, No.3, pp.449-455.

[44] ROMERO, R.J., MURR, L.E., **"Torque-Related Lamellar Carbide Growth Associated with Annealing Twins in 304 Stainless Steel"**, Acta Metallurgical Material, 1995, Vol. 43, No. 2, pp. 461-469.

[45] LIN, P., PALUMBO, G., AUST, K.T., **"Experimental Assessment of the Contribution of Annealing Twins to CSL Distributions in FCC Materials"**, Scripta Materialia, 1997, Vol. 36, No.10, pp.1145-1149.

[46] THAVEEPRUNGSRIPORN, V. and WAS, G.S., **"The Role of Coincidence-Site-Lattice Boundaries in Creep of Ni-16Cr-9Fe at 360°C"**, Metallurgical and Materials Transactions A, Oct. 1997, Vol.28A, pp.2101-2112.

[47] KUMAR, M., KING, W.E., SCHWARTZ, A.J., **"Microstructural Evolution during Grain Boundary Engineering of Low to Medium Stacking Fault Energy FCC Material"**, Acta Materialia, 2002, Vol. 50, pp. 2599-2612.

[48] THOMSON, C.B. and RANDLE, V., **"The Effects of Strain Annealing on Grain Boundary Distribution and Hardening in Superpure Nickel"**, Textures and Microstructures, 1996, Vol. 28, pp.71-79.

[49] PALUMBO, G., KING, P.J., AUST, K.T., ERB, U., LICHTENBERGER, P.C., **"A Grain Boundary Engineering Approach to Materials Reliability"**, Material Research Society, 1997, Vol. 458, pp. 273-281

[50] RANDLE, V., **"Early Stages of Recrystallization in Nickel"**, Metallurgical Transaction A, 1990, Vol. 21A, pp.2215-2221.

[51] WATANABE, T., TSUREKAWA, S., **"The Control of Brittleness and Development of Desirable Mechanical Properties in Polycrystalline Systems by Grain Boundary Engineering"**, Acta Materialia, 1999, Vol. 47, No. 15, pp. 4171-4185.

[52] KUMAR, M., KING, W.E., SCHWARTZ, A.J., **"Modifications to the Microstructural Topology in F.C.C. Materials through Thermomechanical Processing"**, Acta Materialia, 2000, Vol. 48, pp.2081-2091.

[53] KUMAR, M., KING, W.E., SCHWARTZ, A.J., **"Analysis of Grain Boundary Networks and their Evolution during Grain Boundary Engineering"**, Acta Materialia, 2003, Vol. 51, pp.687-700.

[54] GUO, H., CHATURVEDI, M.C., RICHARDS, N.L., McMAHON, G.S., **"Interdependence of Character of Grain Boundaries, Intergranular Segregation of Boron and Grain Boundary Liquation in Simulated Weld Heat-Affected Zone in Inconel-718",** Scripta Materialia, 1999, Vol. 40, No. 3, pp. 383-388

[55] ALEXANDREANU, B., CAPELL, B., WAS, G.S., **"Combined Effects of Special Grain Boundaries and Grain Boundary Carbides on IGSCC of Ni-16Cr-9Fe-xC Alloys",** Materials Science and Engineering A, 2001, pp.94-104.

[56] DINGLEY, D.J., **"The Development of Automated Diffraction in Scanning and Transmission Electron Microscope"**, from Electron backscatter diffraction in material science. Kluwer Academic / Plenum Publishers 2000, pp. 1-18

[57] ALLOY DIGEST, **"Nickel 200/201 (Commercially Pure Nickel)"**, ASM International, 1998.

[58] ASTM Handbook, Specification E8, 1998

[59] BEER, F.P., JOHNSTON, E.R., **"Mechanics of Materials"**, McGraw Hill Inc., 1992, 2nd Edition, pp. 39-50.

[60] **"Standard Test Method for Vickers Hardness of Metallic Material"**, ASTM Designation: E 92, 1982.

[61] DINGLEY, D.J. and RANDLE, V., **Review: "Microtexture Determination by Electron Back-Scatter Diffraction"**, Journal of Materials Science 27, 1992, 4545-4566

[62] RANDLE, V., "**Theoretical Framework for Electron Backscatter Diffraction**", from Electron backscatter diffraction in material science. Kluwer Academic / Plenum Publishers 2000, P. 19-30.

[63] BUCHANAN, P.J., RANDLE, V., FLEWITT, P.E.J., **"A Simple Procedure for he Asessment of Plastic Strain in Electron Back-Scatter Diffraction Patterns"**, Scripta Materialia, 1997, Vol. 37, No. 10, pp. 1511-1518.

[64] WATANABE, T. and RALPH, B., **"The Characterization of Grain Boundaries"**, Scripta Metallurgica, 1992, Vol. 27, pp.1509-1514.

[65] FIELD, D.P., DINGLEY, D.J., "Microstructure Mapping of Interconnects by Orientation Imaging Microscopy", TexSEM Laboratories, Inc.

[66] WEBSITE - http://www.tsl.com/oim

[67] BLACK, M.P., HIGGINSON, R.L., **"An Investigation into the use of Electron Back-Scattered Diffraction to Measure Recrystallised Fraction"**, Scripta Materialia, 1999, Vol. 41, No. 2, pp. 125-129.

[68] KRIEGER, N.C., JENSEN, D. JUUL and CONRADSEN, K., **"Image Processing Procedures for Analysis of Electron Back Scattering Patterns"**, Scanning Microscopy, 1992, Vol. 6, No.1, pp.115-121.

[69] RANDLE, V., VALE, S., **"Mapping Microstructures"**, Materials World

[70] BASSON, F., DRIVER, J.H., **"Deformation Banding Mechanisms during Plane Strain Compression of Cube-Oriented F.C.C. Crystals"**, Acta Materialia, 2000, Vol. 48, pp. 2101-2115.

[71] MAHAJAN, S., PANDE, C.S., IMAM, M.A. and RATH, B.B., **"Formation of Annealing Twins in F.C.C. Crystals"**, Acta Mater, 1997, Vol. 45, No. 6, pp. 2633

[72] SANGAL, S., TANGRI, K., **"The Effect of Small Plastic Deformation and Annealing on the Properties of Polycrystals: Part II. Theoretical Model for the Transformation of Non-Equilibrium Grain Boundaries"**, Metallurigical Transaction, 1989, 20A, pp. 479-484.

[73] PUMPHREY. P., GLEITER, H., Phil Mag., 1974, Vol. 30, pp. 593-602

APPENDIX

Table A1 (a-d): CSL distribution of $3 \leq \sum \leq 29$ strained and annealed at 900°C

(a)

1 step – 6% strain annealed at 900°C

Sigma	Tolerance	Fraction
3	8.66	0.603
9	5	0.083
27a	2.89	0.028
27b	2.89	0.014
5	6.71	0.002
7	5.67	0
11	4.52	0.001
13a	4.16	0.002
13b	4.16	0
15	3.87	0
17a	3.64	0.001
17b	3.64	0.001
19a	3.44	0
19b	3.44	0
21a	3.27	0.003
21b	3.27	0.001
23	3.13	0.004
25a	3	0
25b	3	0.004
29a	2.79	0
29b	2.79	0
summary		0.747

(b)

2 steps – 3% strain annealed at 900°C

Sigma	Tolerance	Fraction
3	8.66	0.621
9	5	0.083
27a	2.89	0.008
27b	2.89	0.013
5	6.71	0.004
7	5.67	0.001
11	4.52	0.002
13a	4.16	0
13b	4.16	0.002
15	3.87	0.004
17a	3.64	0
17b	3.64	0
19a	3.44	0.003
19b	3.44	0
21a	3.27	0
21b	3.27	0
23	3.13	0.004
25a	3	0
25b	3	0.003
29a	2.79	0.003
29b	2.79	0.002
summary		0.75

(c)

2 steps – 3% strain annealed at 900°C

Sigma	Tolerance	Fraction
3	8.66	0.661
9	5	0.051
27a	2.89	0.009
27b	2.89	0.021
5	6.71	0.002
7	5.67	0.003
11	4.52	0
13a	4.16	0
13b	4.16	0.001
15	3.87	0.001
17a	3.64	0
17b	3.64	0
19a	3.44	0.001
19b	3.44	0
21a	3.27	0
21b	3.27	0
23	3.13	0.001
25a	3	0.004
25b	3	0.001
29a	2.79	0
29b	2.79	0
summary		0.756

(d)

4 steps – 3% strain annealed at 900 °C

Sigma	Tolerance	Fraction
3	8.66	0.636
9	5	0.077
27a	2.89	0.014
27b	2.89	0.021
5	6.71	0.006
7	5.67	0.004
11	4.52	0
13a	4.16	0
13b	4.16	0.001
15	3.87	0.001
17a	3.64	0
17b	3.64	0
19a	3.44	0
19b	3.44	0
21a	3.27	0.001
21b	3.27	0
23	3.13	0.002
25a	3	0
25b	3	0.001
29a	2.79	0.003
29b	2.79	0
summary		0.768

A2(a)

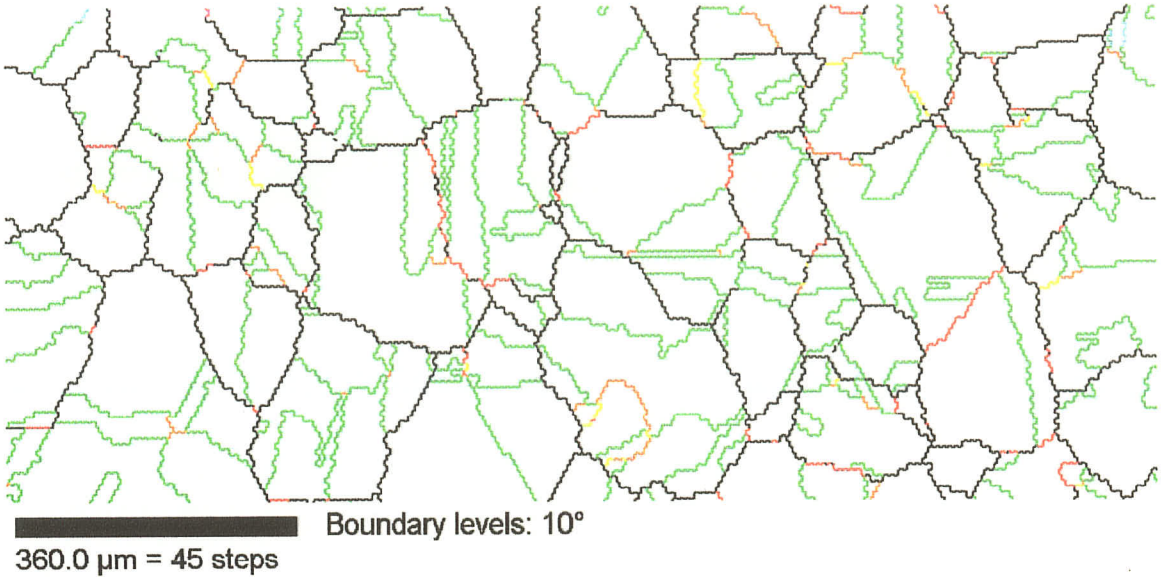
Boundary levels: 10°
360.0 µm = 45 steps

A2(b)

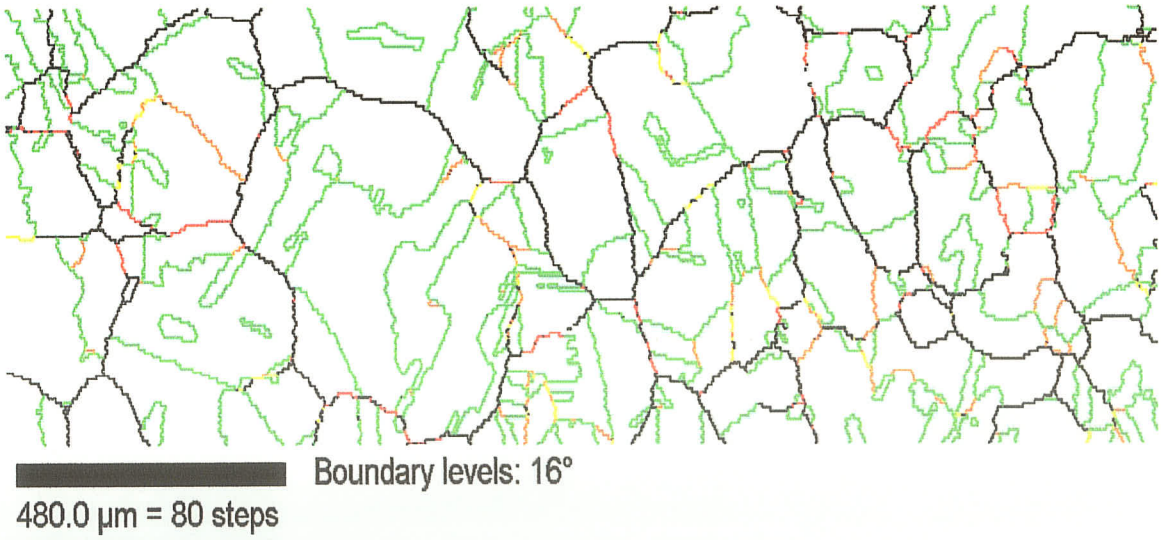
Boundary levels: 16°
480.0 µm = 80 steps

A2(c)

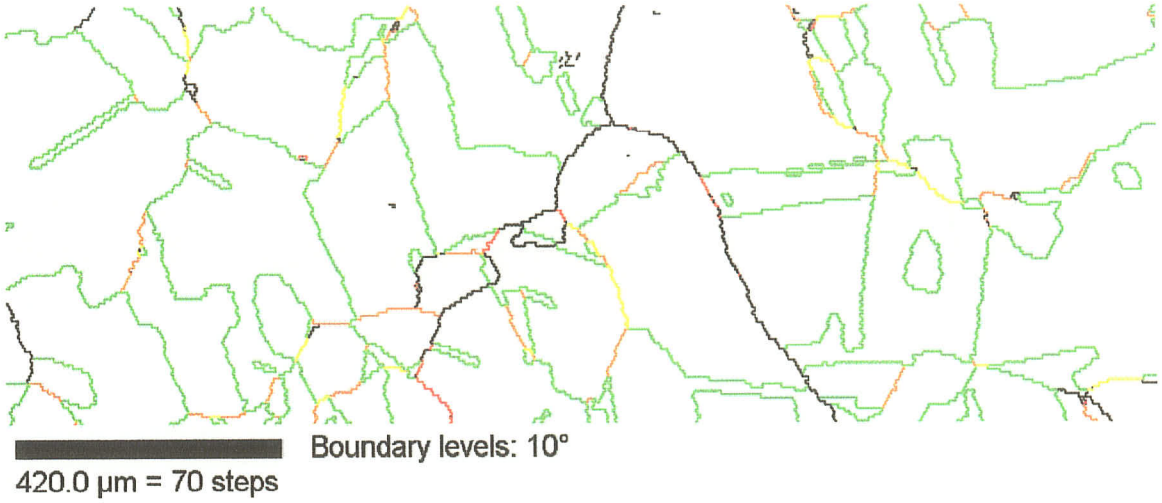

A2(d)

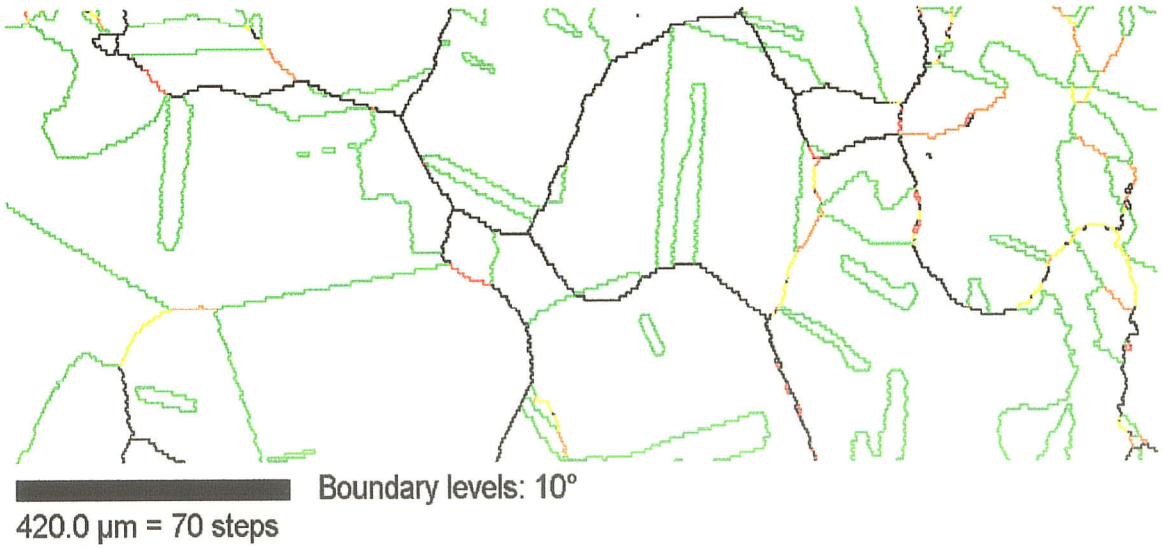

Figure A2: Grain boundary network OIM maps of samples processed with (a) 1 step – 6% strain, (b) 2 steps – 3% strain, (c) 2 steps – 6% strain, (d) 4 steps – 3% strain annealed at 1000°C for 10minutes

A2(c)

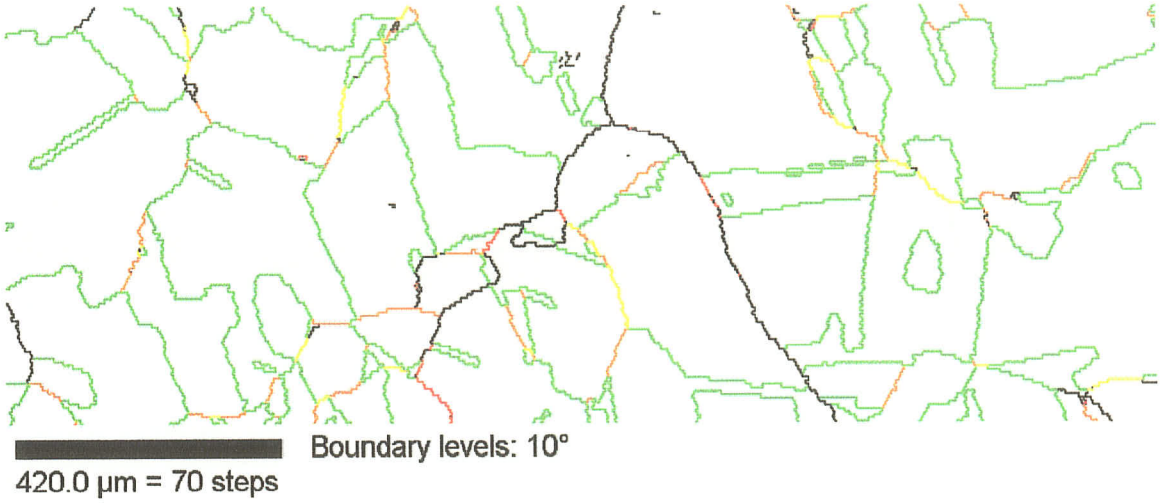

A2(d)

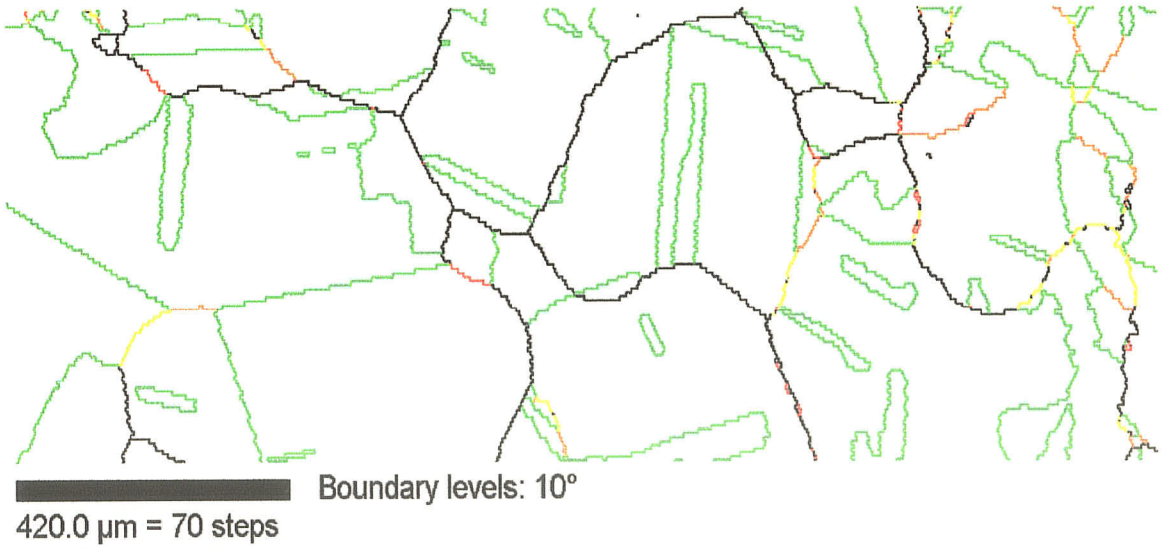

Figure A2: Grain boundary network OIM maps of samples processed with (a) 1 step – 6% strain, (b) 2 steps – 3% strain, (c) 2 steps – 6% strain, (d) 4 steps – 3% strain annealed at 1000°C for 10minutes

A2(e)

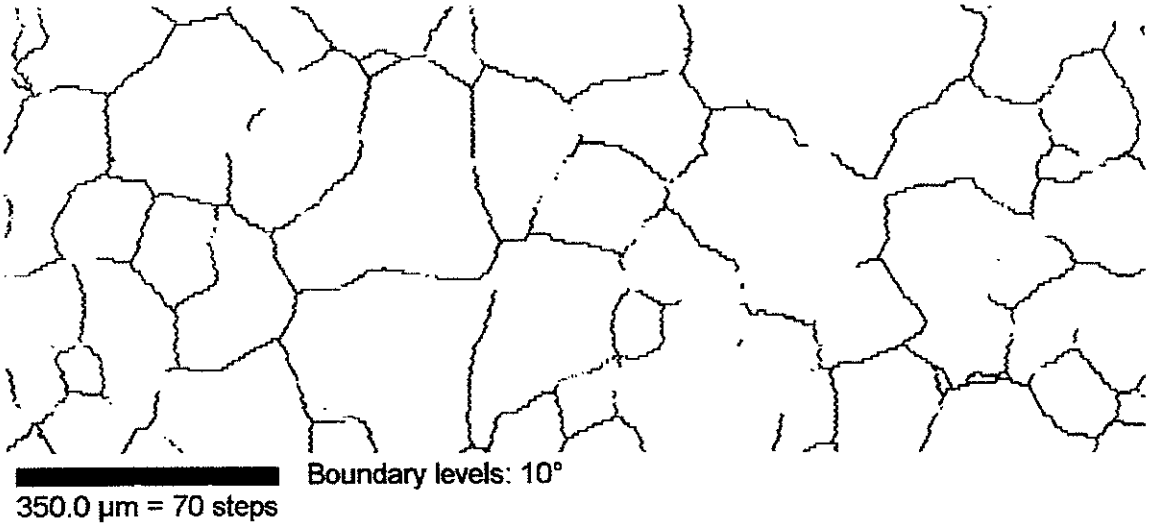
Boundary levels: 10°
350.0 µm = 70 steps

A2(f)

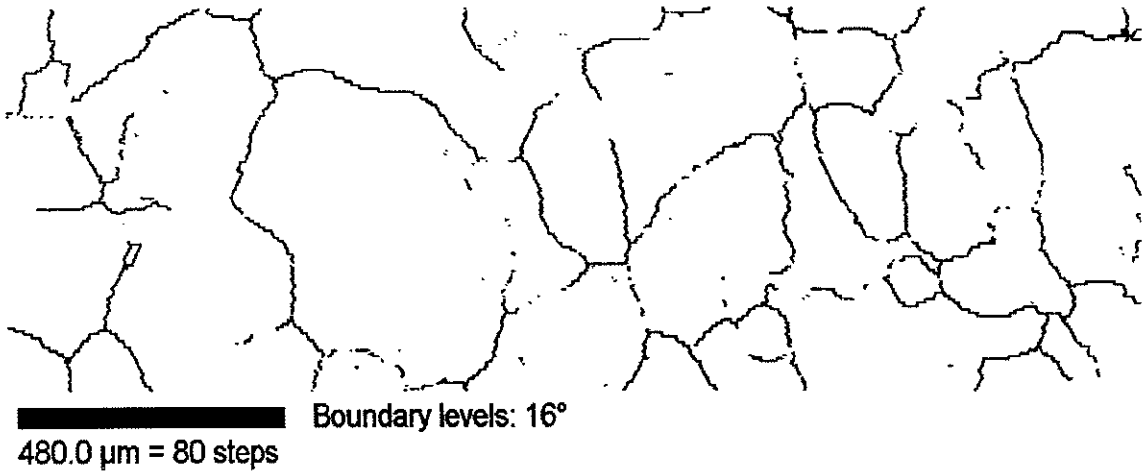
Boundary levels: 16°
480.0 µm = 80 steps

A2 (g)

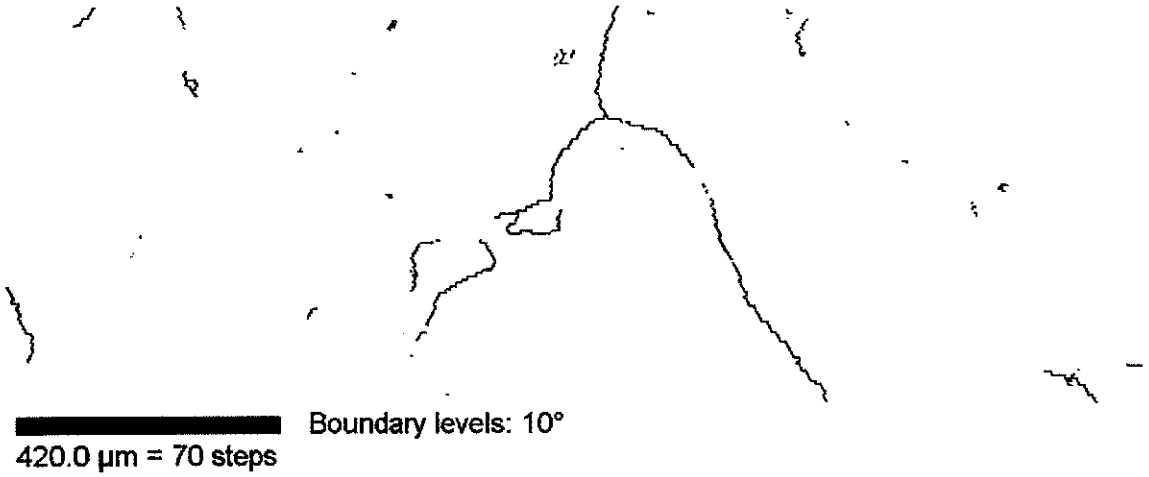

A2(h)

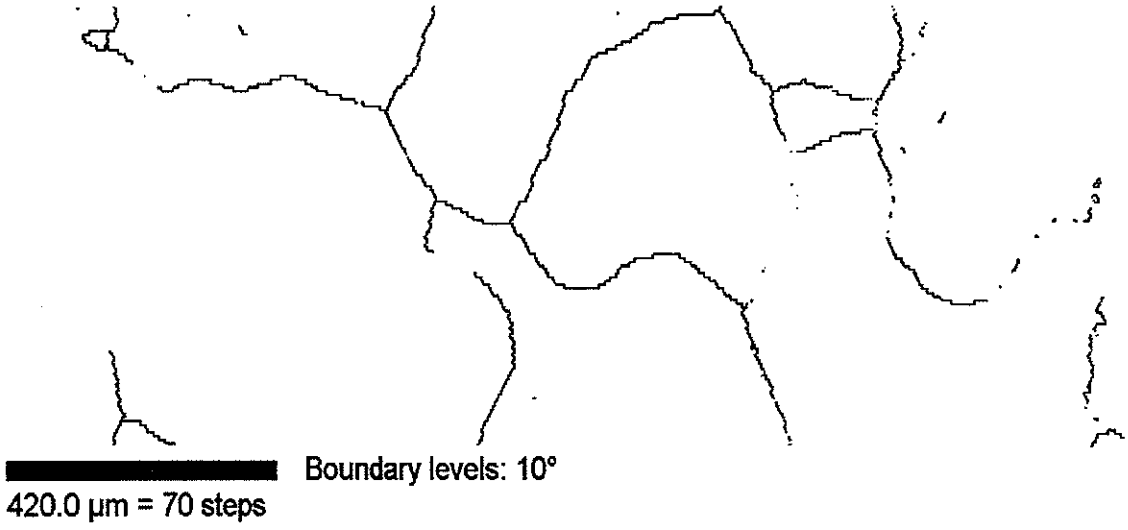

Figure A2: Random boundary network OIM maps of samples processed with (e) 1 step – 6% strain, (f) 2 steps – 3% strain, (g) 2 steps – 6% strain, (h) 4 steps – 3% strain annealed at 1000°C for 10minutes

Table A3 (a-d): CSL distribution of $3 \leq \sum \leq 29$ strained and annealed at 1000°C

(a)

1 step – 6% strain annealed at 1000°C

Sigma	Tolerance	Fraction
3	8.66	0.474
9	5	0.035
27a	2.89	0.008
27b	2.89	0.005
5	6.71	0.007
7	5.67	0.006
11	4.52	0.004
13a	4.16	0
13b	4.16	0.005
15	3.87	0.003
17a	3.64	0
17b	3.64	0
19a	3.44	0
19b	3.44	0
21a	3.27	0.003
21b	3.27	0.002
23	3.13	0.002
25a	3	0.003
25b	3	0.005
29a	2.79	0
29b	2.79	0
summary		0.564

(b)

2 steps – 3% strain annealed at 1000°C

Sigma	Tolerance	Fraction
3	8.66	0.345
9	5	0.039
27a	2.89	0.01
27b	2.89	0.004
5	6.71	0.001
7	5.67	0.004
11	4.52	0.002
13a	4.16	0
13b	4.16	0.002
15	3.87	0.001
17a	3.64	0.001
17b	3.64	0
19a	3.44	0.001
19b	3.44	0.003
21a	3.27	0
21b	3.27	0.003
23	3.13	0
25a	3	0.001
25b	3	0.002
29a	2.79	0.001
29b	2.79	0.001
summary		0.421

(c)

2 steps – 6% strain annealed at 1000°C

Sigma	Tolerance	Fraction
3	8.66	0.5
9	5	0.068
27a	2.89	0.012
27b	2.89	0.018
5	6.71	0
7	5.67	0
11	4.52	0.001
13a	4.16	0
13b	4.16	0
15	3.87	0
17a	3.64	0.002
17b	3.64	0.002
19a	3.44	0.004
19b	3.44	0
21a	3.27	0
21b	3.27	0
23	3.13	0.001
25a	3	0
25b	3	0
29a	2.79	0.001
29b	2.79	0
summary		0.609

(d)

4 steps – 3% strain annealed at 1000°C

Sigma	Tolerance	Fraction
3	8.66	0.47
9	5	0.036
27a	2.89	0.012
27b	2.89	0.018
5	6.71	0.001
7	5.67	0.004
11	4.52	0.003
13a	4.16	0
13b	4.16	0.001
15	3.87	0.002
17a	3.64	0
17b	3.64	0.001
19a	3.44	0
19b	3.44	0
21a	3.27	0
21b	3.27	0
23	3.13	0
25a	3	0
25b	3	0
29a	2.79	0.001
29b	2.79	0
summary		0.54

A4(a)

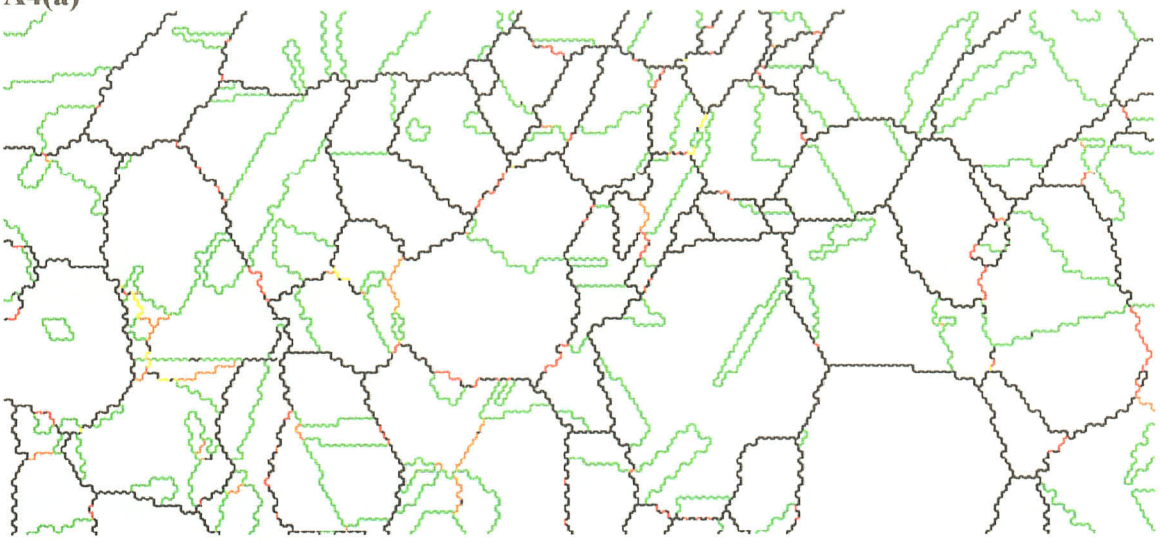

Boundary levels: 10°

105.0 µm = 35 steps

A4(b)

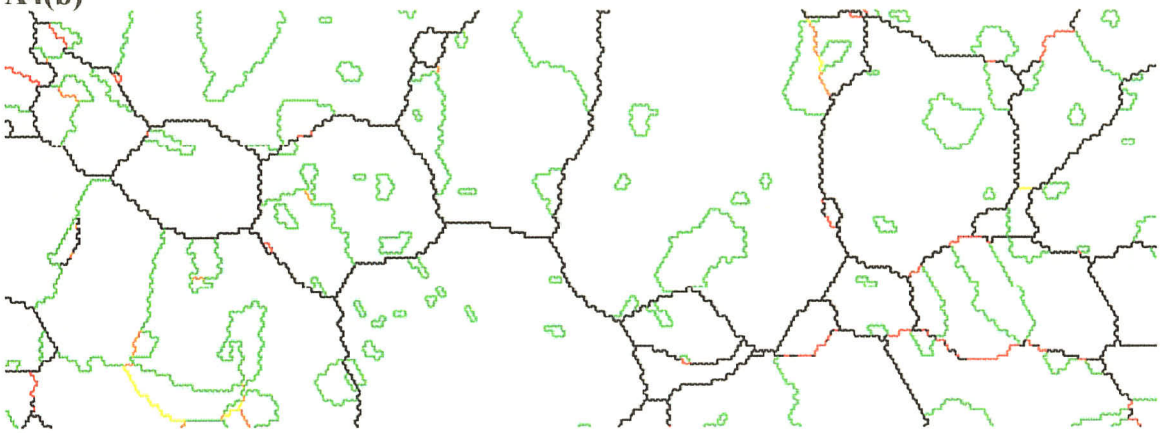

Boundary levels: 10°

415.0 µm = 50 steps

A4(c)

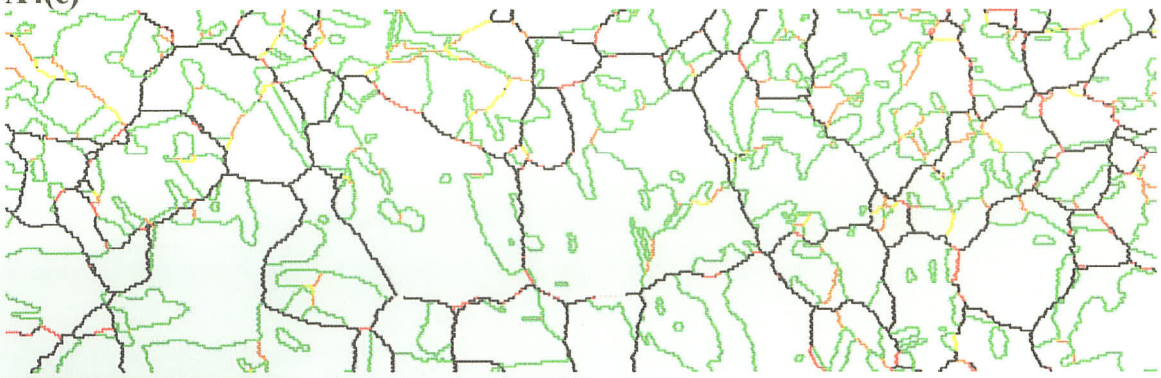

Boundary levels: 10°

477.0 µm = 90 steps

A4(d)

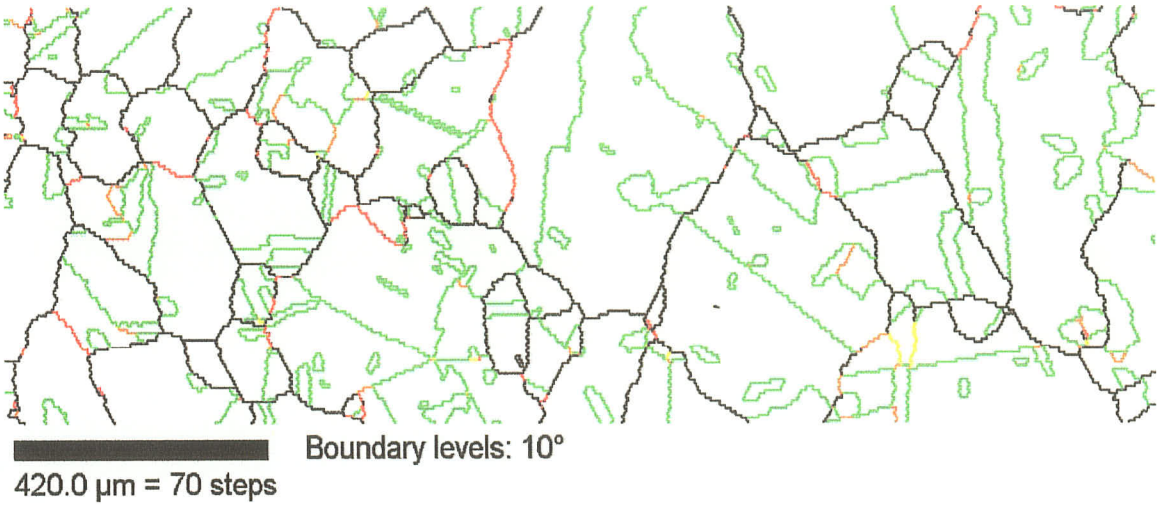

A4(e)

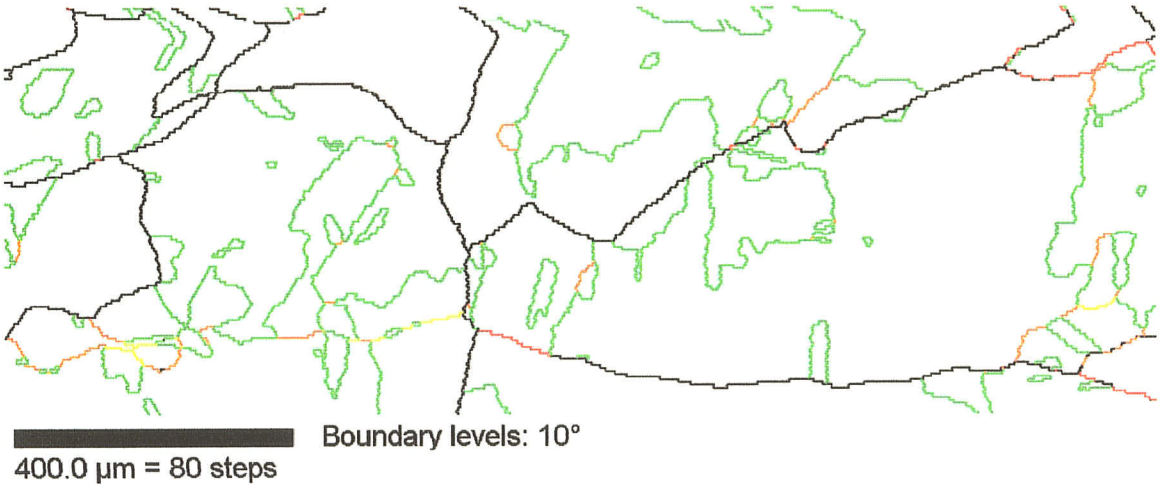

Figure A4: OIM map of grain boundary network in the microstructure of 1 step – 3% strain annealed at 700°C for (a) 0.167hr, (b) 48hr, (c) 72hr, (d) 96hr, (e) 168hr

A5 (a)

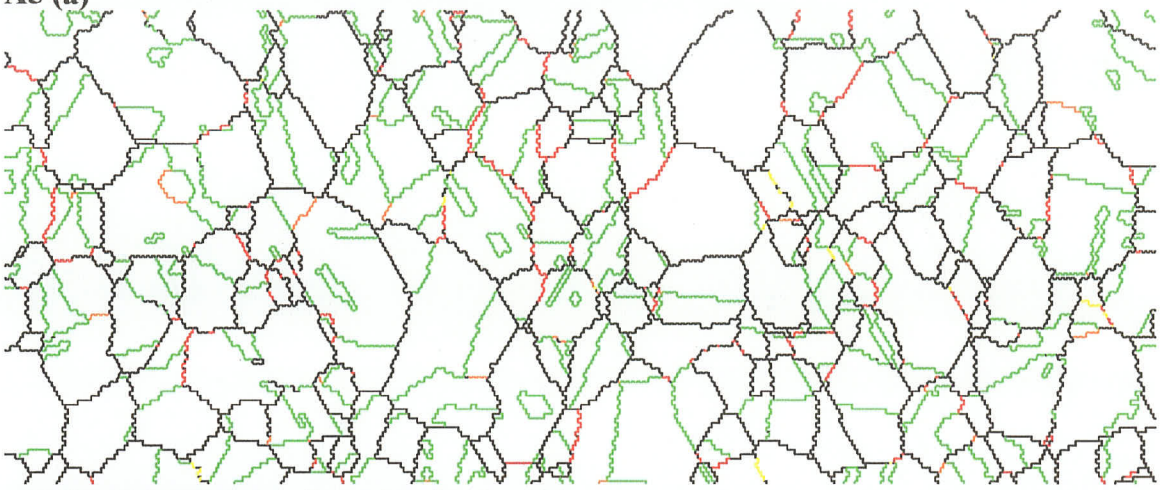

Boundary levels: 10°

100.0 µm = 50 steps

A5(b)

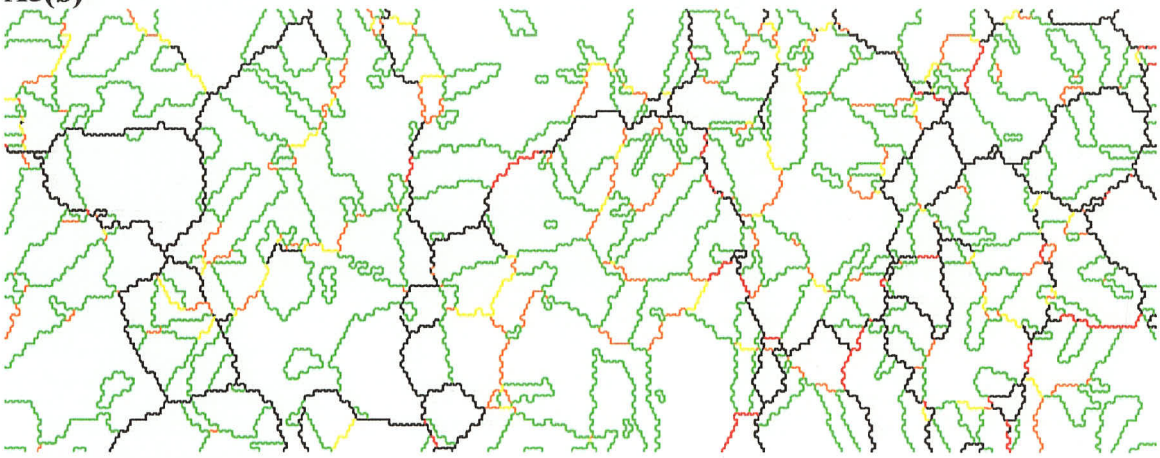

Boundary levels: 10°

360.0 µm = 45 steps

A5(c)

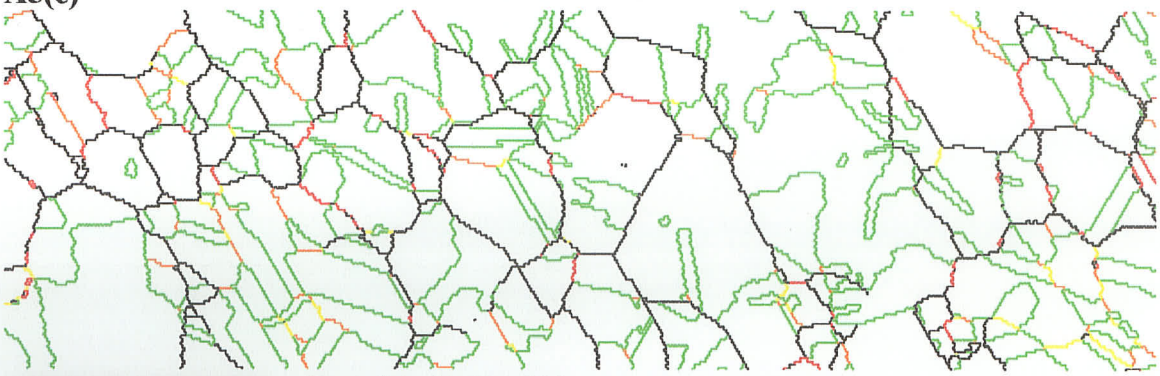

Boundary levels: 10°

420.0 µm = 70 steps

A5(d)

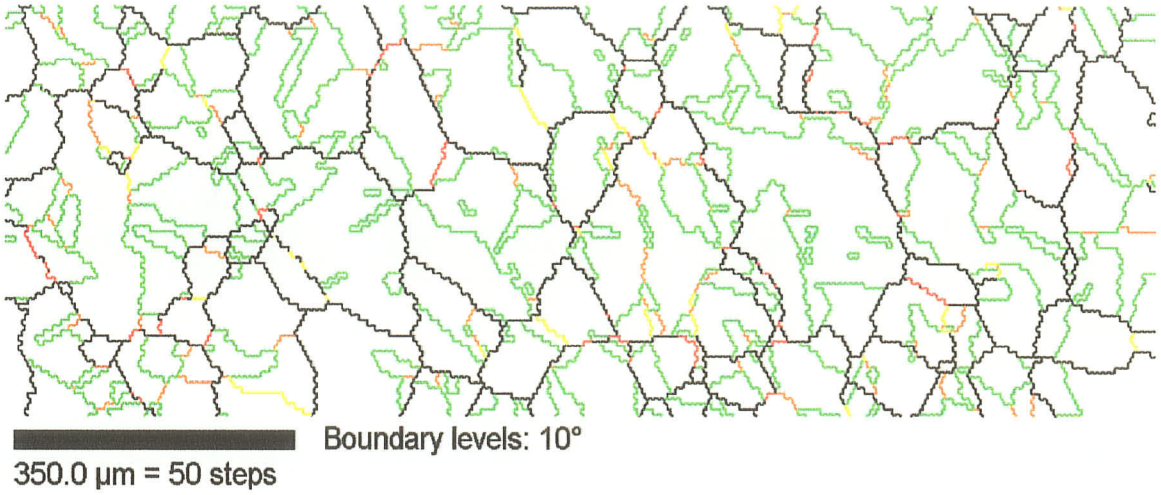

A5(e)

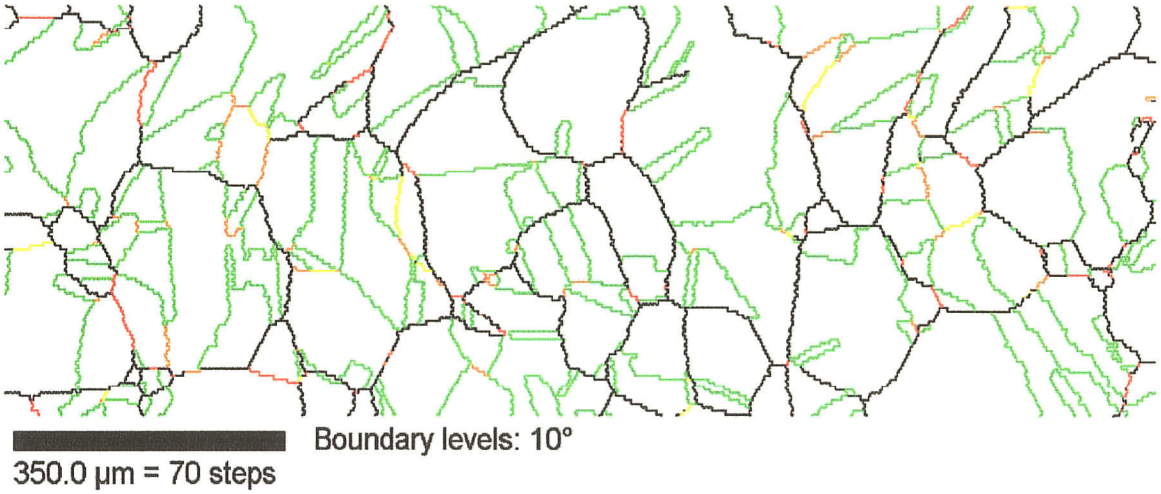

Figure A5: OIM map of grain boundary network in the microstructure of 1 step – 6% strain annealed at 700°C for (a) 0.167hr, (b) 48hr, (c) 72hr, (d) 96hr, (e) 168hr

A5(f)

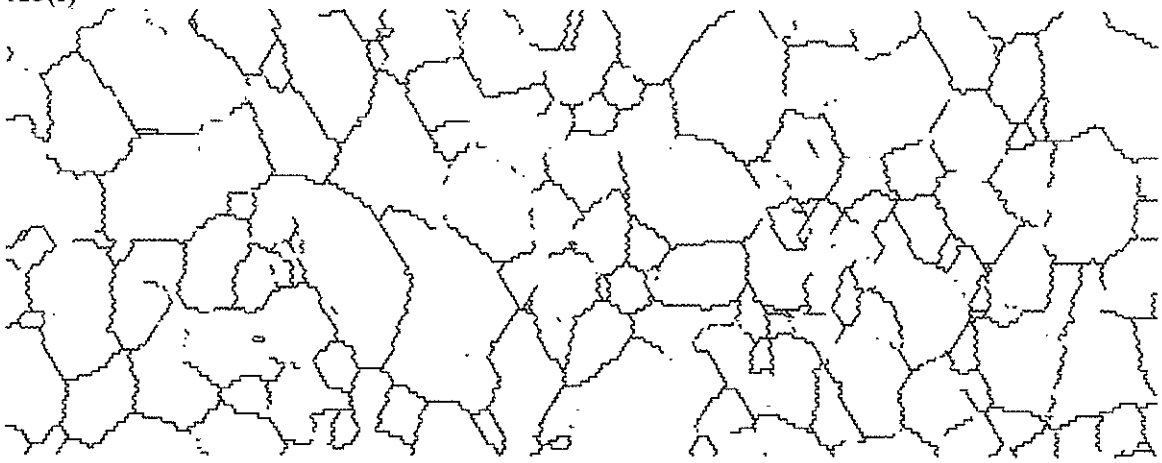

Boundary levels: 10°

100.0 µm = 50 steps

A5(g)

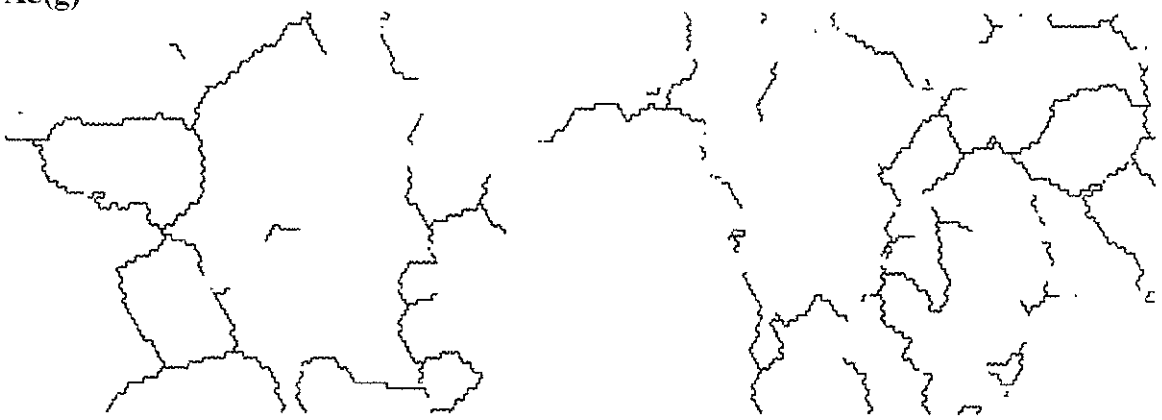

Boundary levels: 10°

360.0 µm = 45 steps

A5(h)

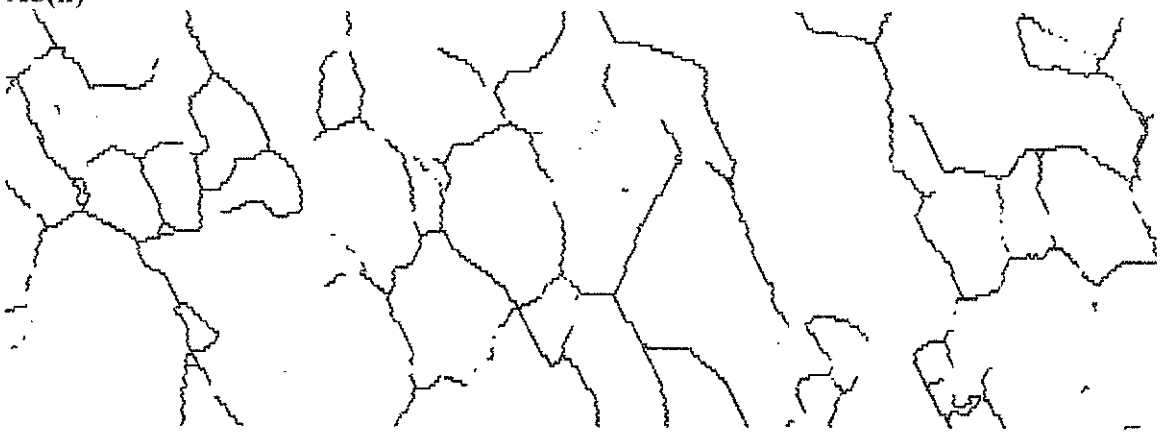

Boundary levels: 10°

420.0 µm = 70 steps

A5(i)

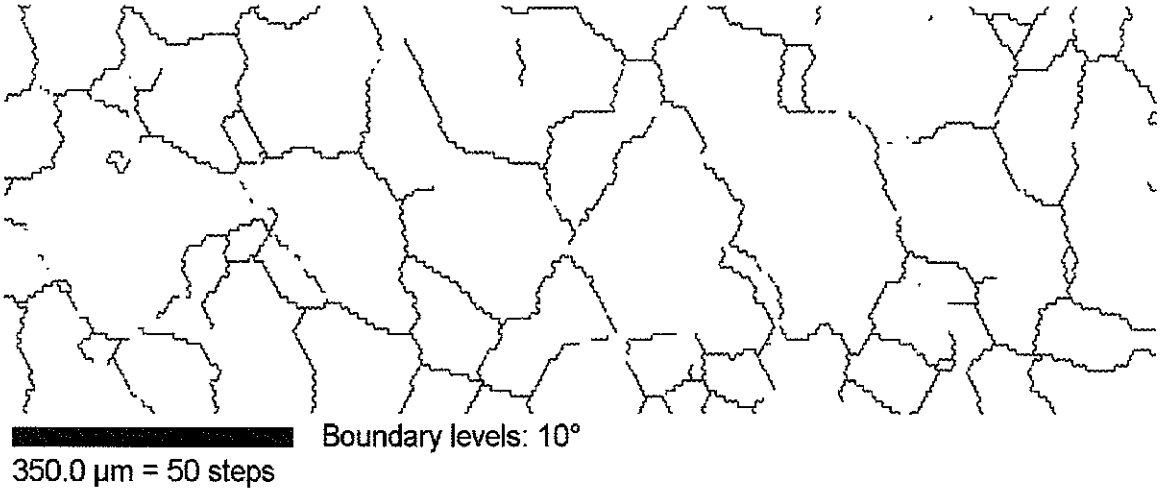

A5(j)

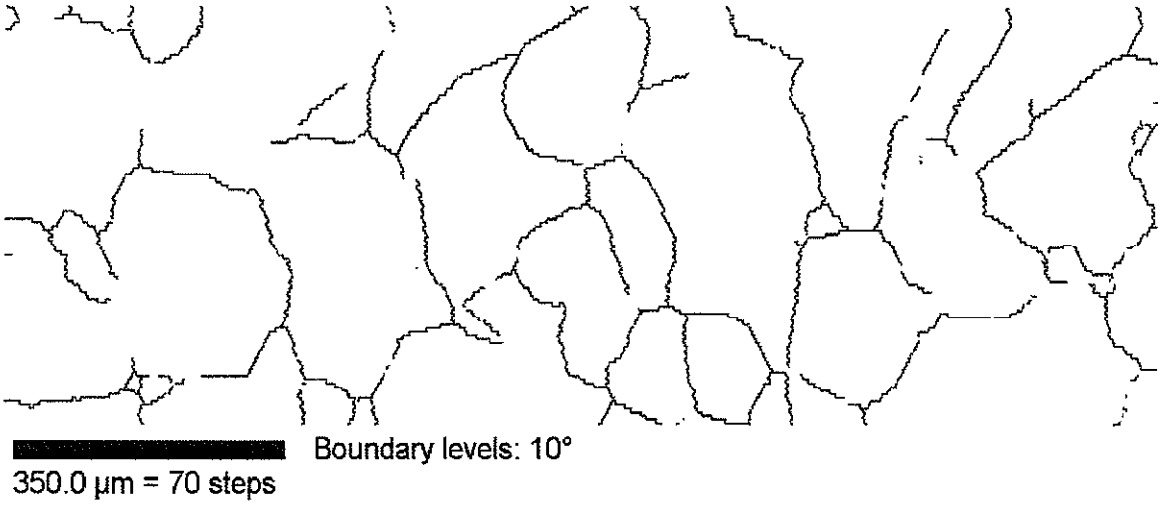

Figure A5: OIM map of random boundary network in the microstructure of 1 step – 6% strain annealed at 700°C for (f) 0.167hr, (g) 48hr, (h)72hr, (i) 96hr, (j) 168hr

A6(a)

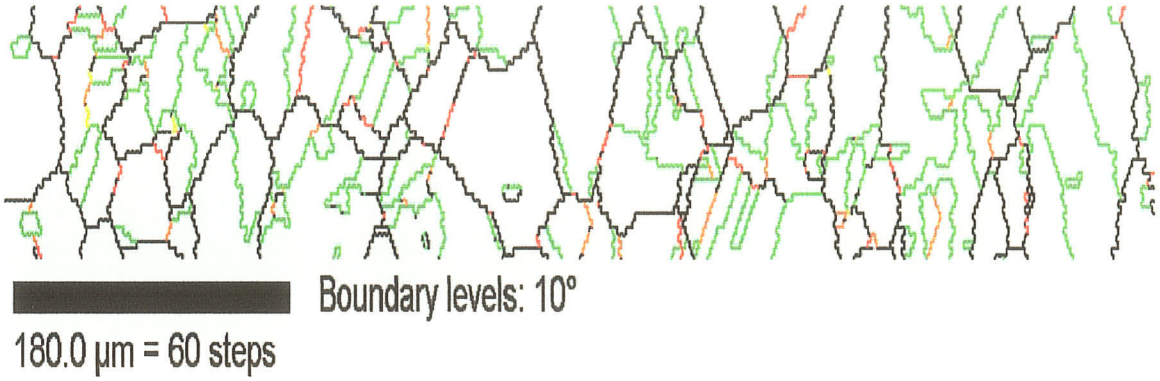
Boundary levels: 10°
180.0 µm = 60 steps

A6(b)

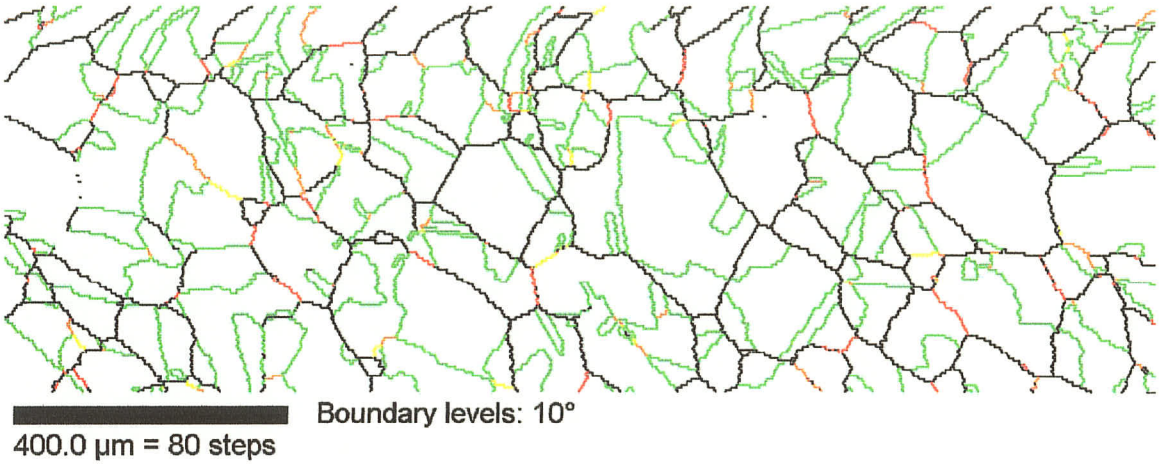
Boundary levels: 10°
400.0 µm = 80 steps

A6(c)

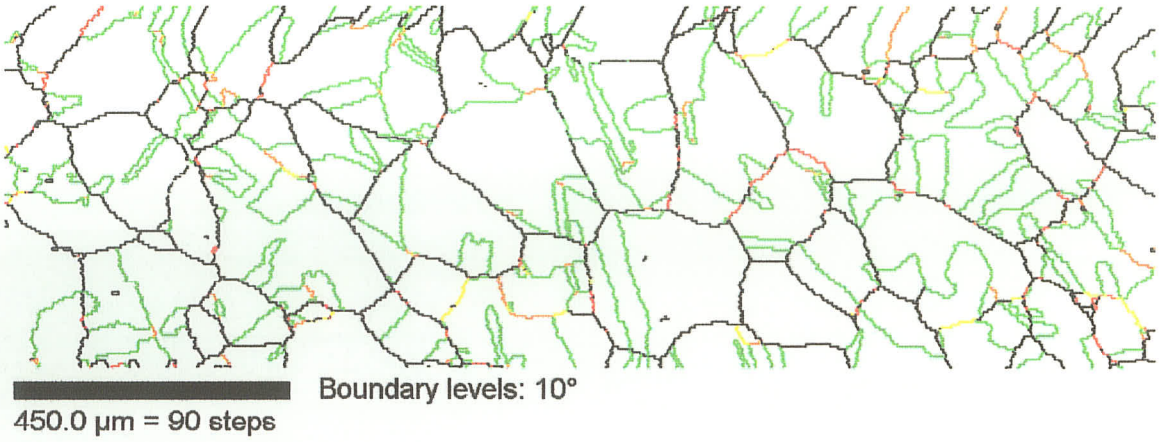
Boundary levels: 10°
450.0 µm = 90 steps

A6 (d)

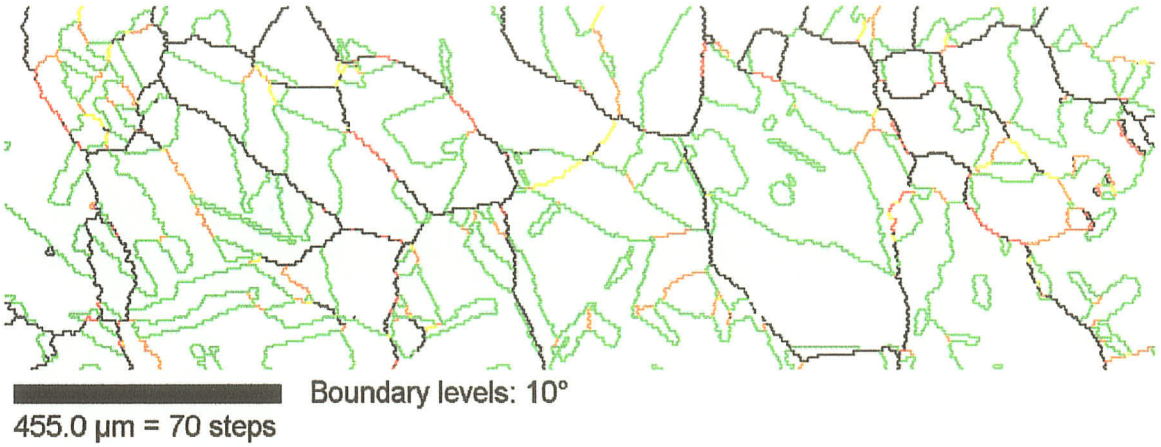

A6 (e)

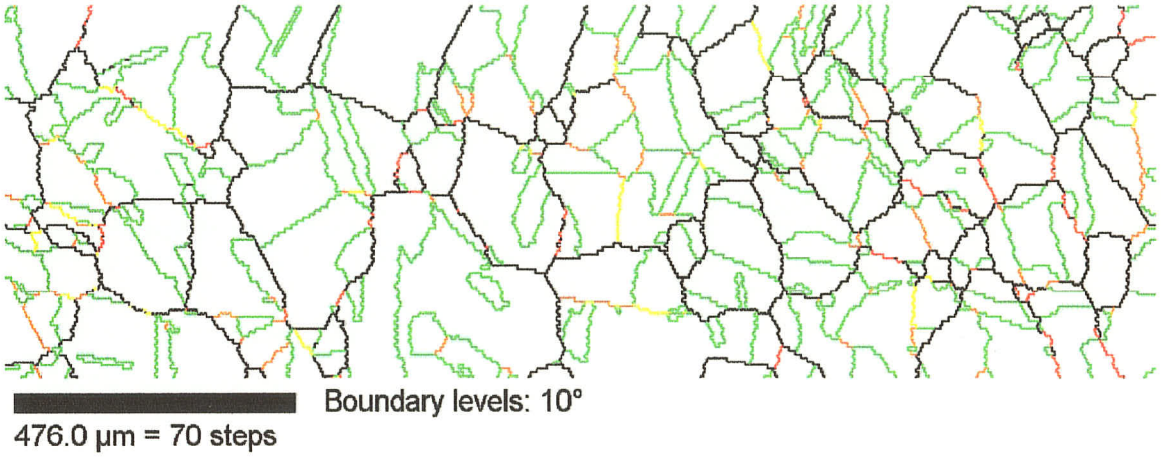

Figure A6: OIM map of grain boundary network in the microstructure of 1 step – 3% strain annealed at 800°C for (a) 0.167hr, (b) 42hr, (c) 84hr, (d) 126hr, (e) 168hr

A6 (f)

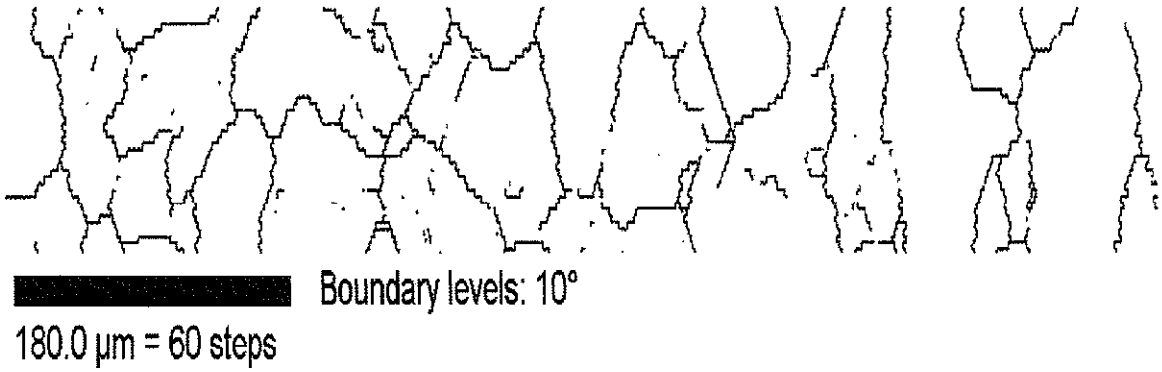
Boundary levels: 10°
180.0 µm = 60 steps

A6 (g)

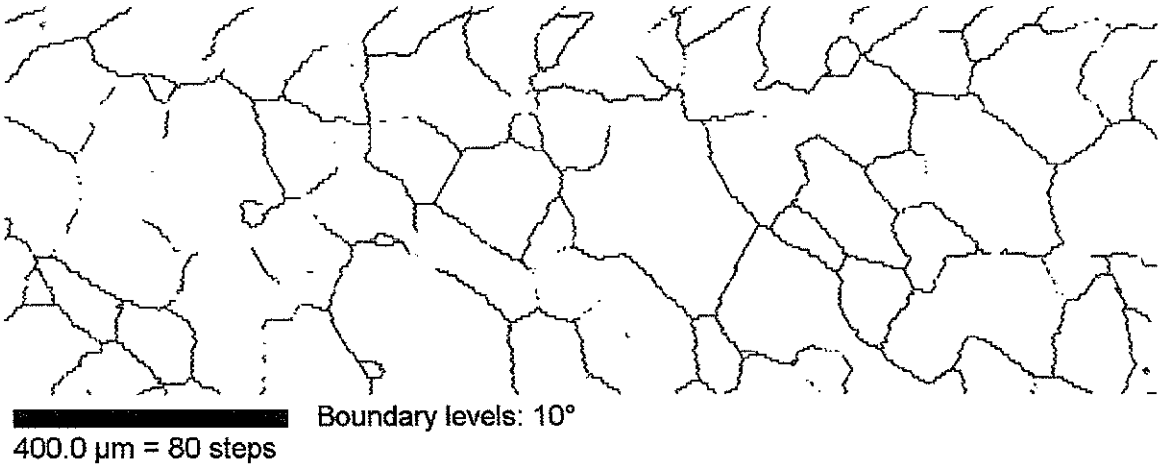
Boundary levels: 10°
400.0 µm = 80 steps

A6 (h)

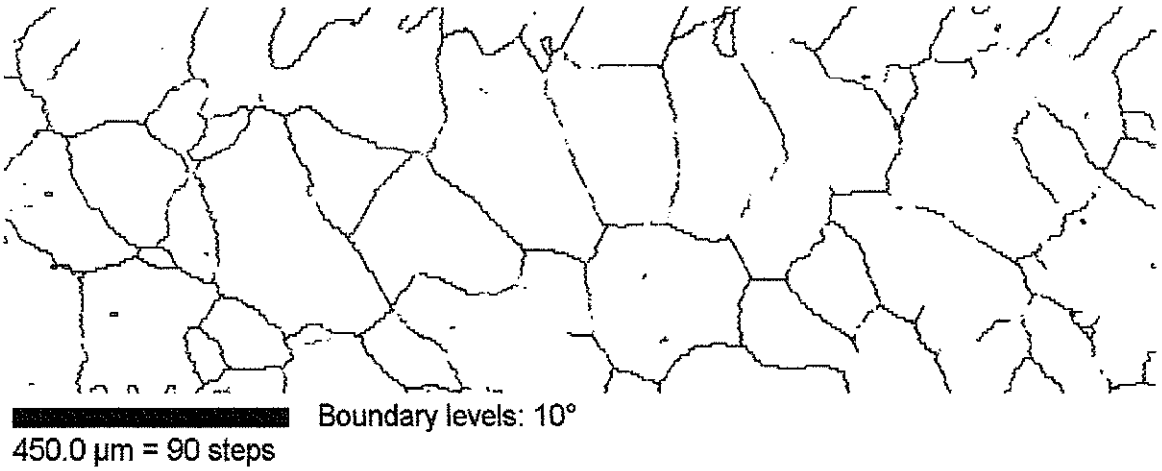
Boundary levels: 10°
450.0 µm = 90 steps

A6 (i)

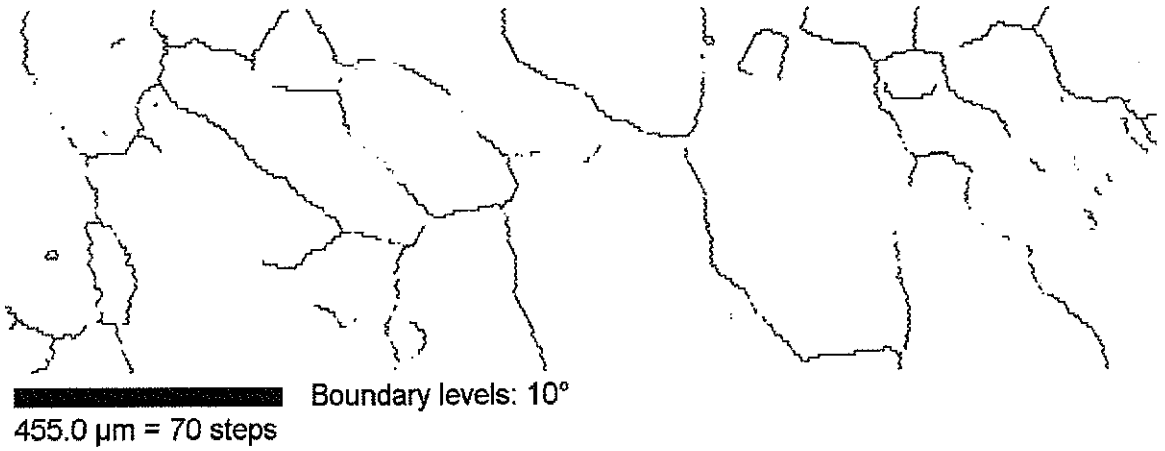

A6 (j)

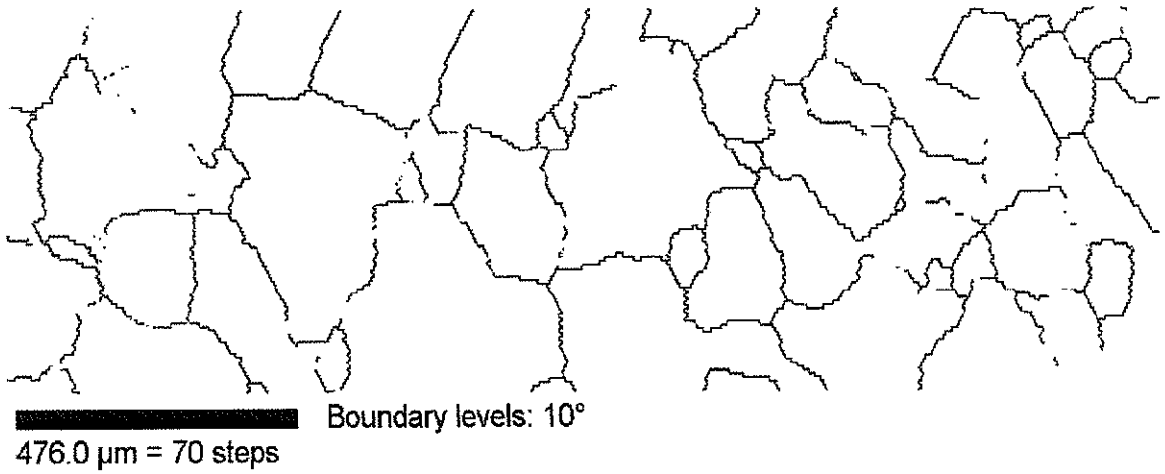

Figure A6: OIM map of random boundary network in the microstructure of 1 step – 3% strain annealed at 800°C for (f) 0.167hr, (g) 42hr, (h) 84hr, (i) 126hr, (j) 168hr

A7(a)

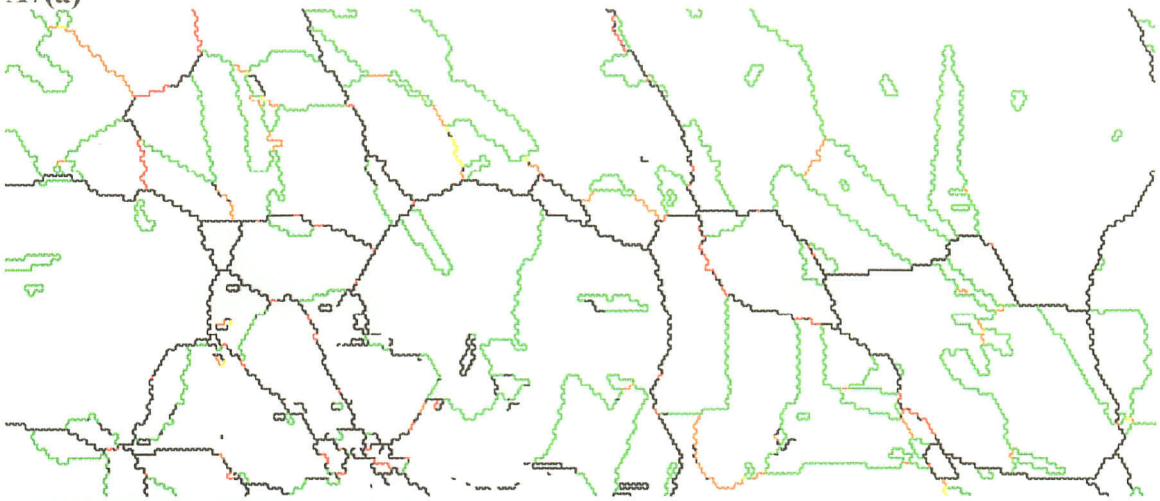

Boundary levels: 10°

135.0 µm = 45 steps

A7(b)

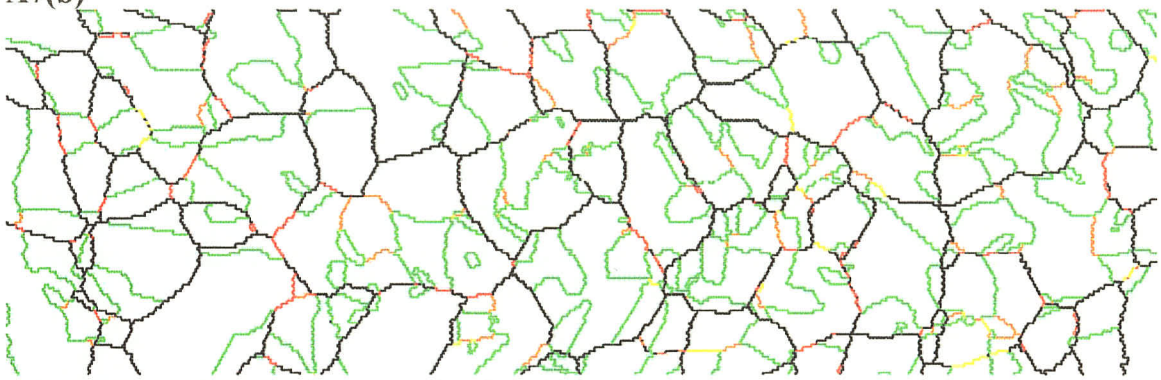

Boundary levels: 10°

420.0 µm = 70 steps

A7(c)

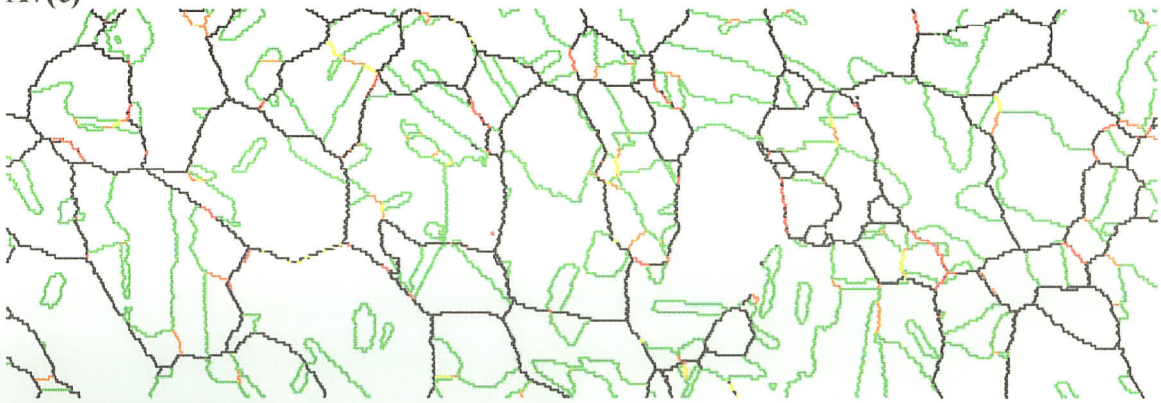

Boundary levels: 10°

440.0 µm = 80 steps

A7(d)

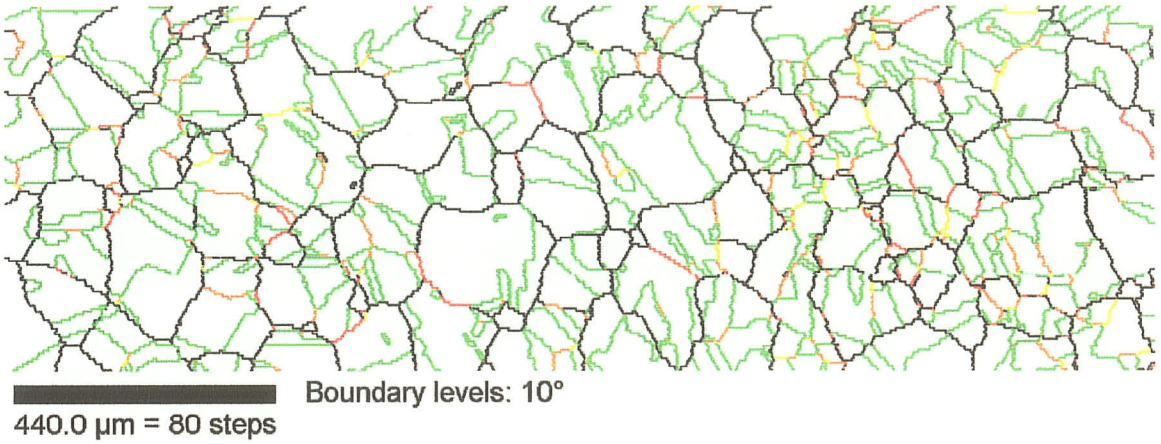

A7(e)

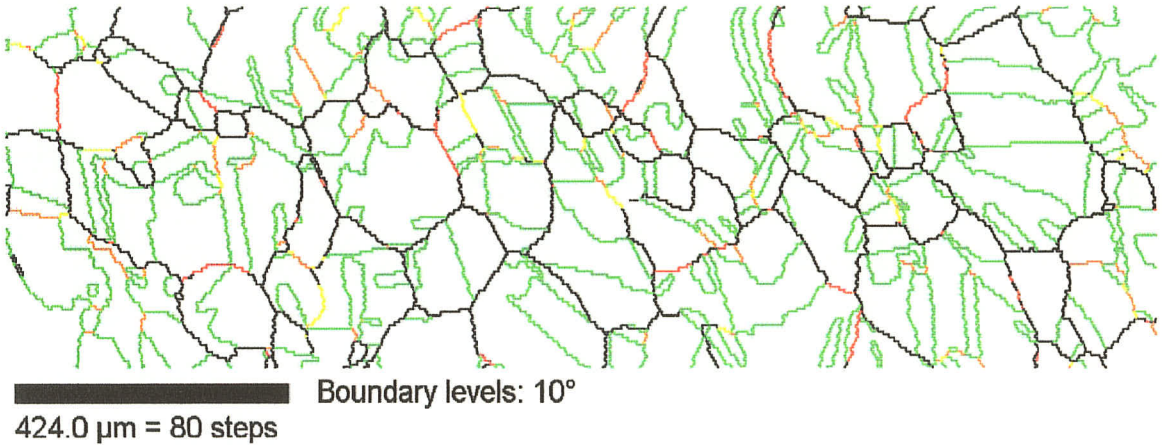

Figure A7: OIM map of grain boundary network in the microstructure of 1 step – 6% strain annealed at 800°C for (a) 0.167hr, (b) 42hr, (c) 84hr, (d) 126hr, (e) 168hr

A7(f)

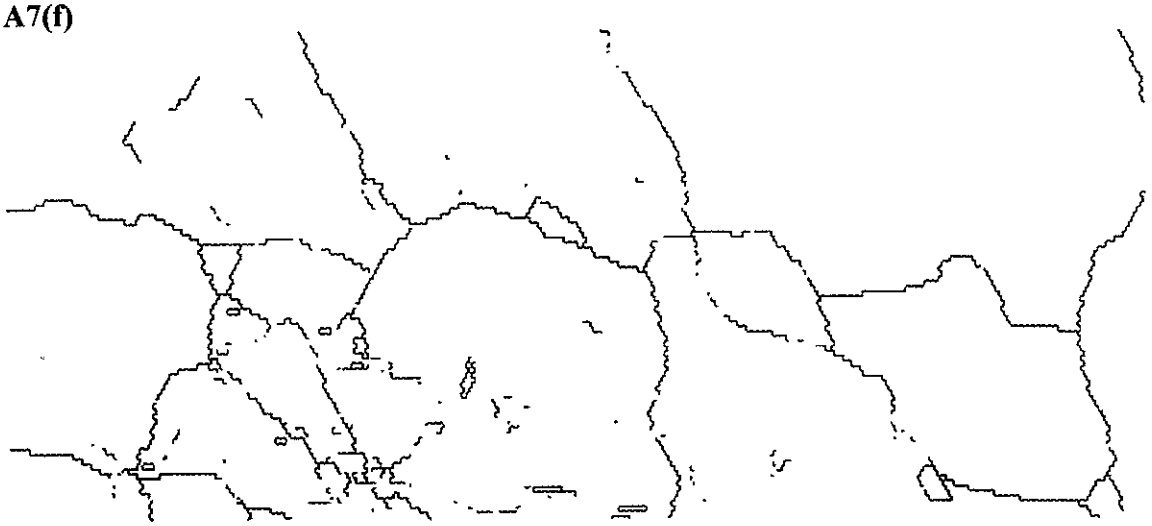

Boundary levels: 10°

135.0 µm = 45 steps

A7(g)

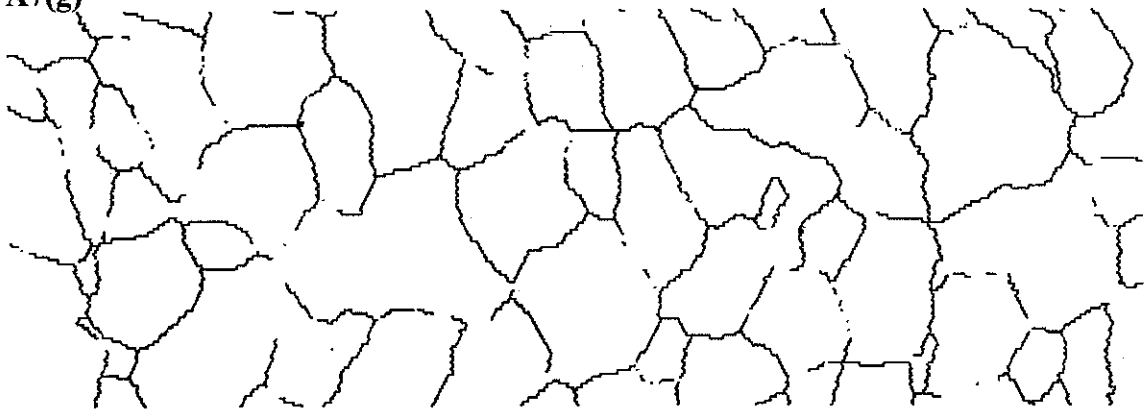

Boundary levels: 10°

420.0 µm = 70 steps

A7(h)

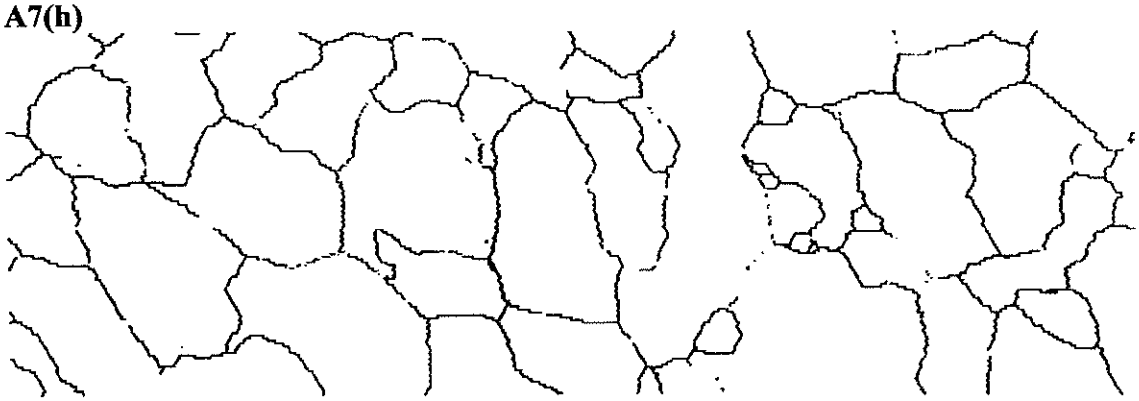

Boundary levels: 10°

440.0 µm = 80 steps

A7(i)

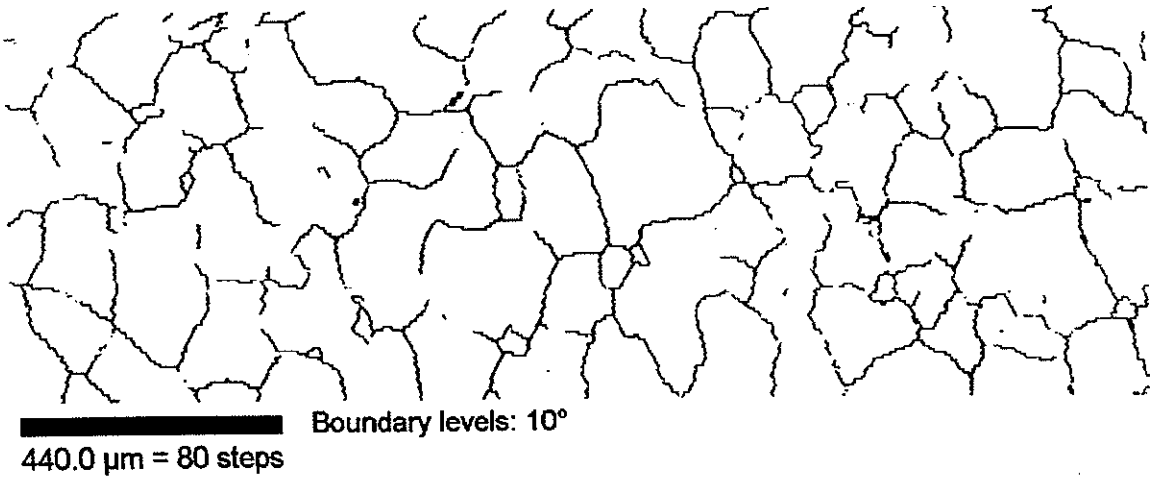

A7(j)

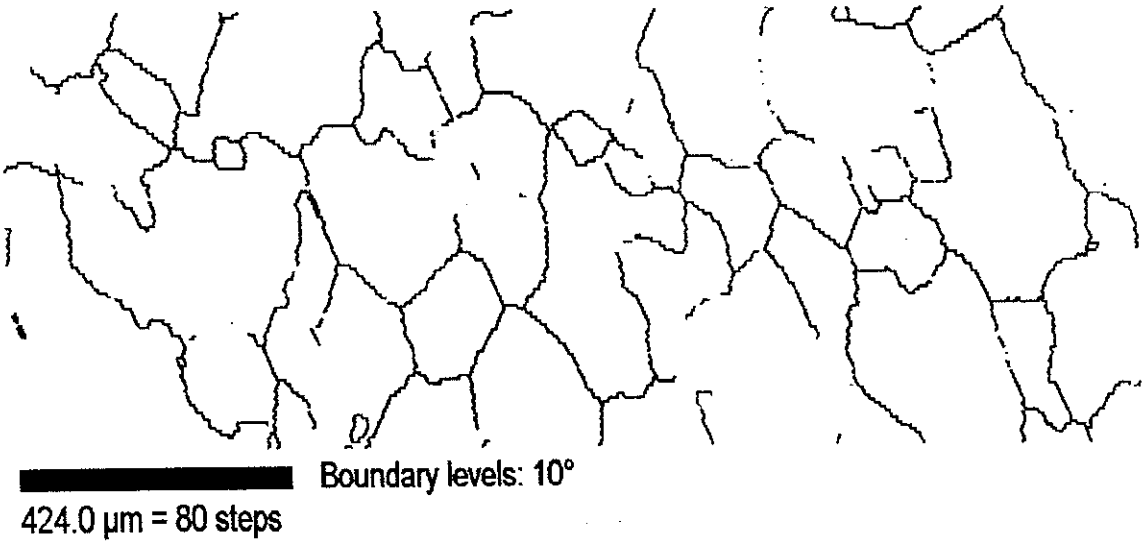

Figure A7: OIM map of random boundary network in the microstructure of 1 step – 6% strain annealed at 800°C for (f) 0.167hr, (g) 42hr, (h) 84hr, (i) 126hr, (j) 168hr